UCLouvain

epl

École polytechnique de Louvain

Seismic health monitoring of high rise buildings in the city of Darwin, Australia

Author: **Gregorio MORRA**
Supervisors: **Ryan HOULT, João Saraiva Esteves Pacheco DE ALMEIDA, Maria Pina LIMONGELLI**
Readers: **Catherine DONEUX, Scott MENEGON**
Academic year 2023–2024
Master [120] in Civil Engineering

Abstract

Seismic Structure Health Monitoring has become increasingly vital for ensuring the safety of civil engineering structures under seismic actions worldwide. This thesis focuses on optimizing the placement of accelerometers in multi-storey buildings, specifically Australian structures.

Building on existing methodologies, this research extends a 2D method for optimal sensor placement by incorporating a 3D model that accounts for torsional modes. Initially, the generalized method was tested on simple 3D frames, demonstrating that sensor layouts derived from torsional modes often resemble those obtained from flexural modes alone. The method was then applied to a typical Australian building model and a real-world case study of the Atwood Building in Anchorage. Despite variations in natural frequencies under different seismic conditions, the optimal sensor placement remained consistent across scenarios, confirming that conclusions drawn from ambient vibrations are valid even under stronger seismic events.

The thesis concludes that torsional modes do not significantly alter the optimal sensor layout, allowing the use of the simpler 2D method in most cases. However, when torsional behaviour is critical, capturing the torsional response can be essential for assessing the structure's health. To support practical applications, a MATLAB tool was developed to assist in determining the optimal sensor placement based on structural characteristics, offering a valuable resource for building owners and authorities.

Keywords: Seismic Structure Health Monitoring, Optimal location of sensors, Australian Structures, Torsional modes, Numerical modelling

Acknowledgements

This Master's thesis was made possible through the help and support of several individuals who guided me throughout the process.

First and foremost, I would like to express my sincere gratitude to my supervisors, Ryan Hoult, João Saraiva Esteves Pacheco de Almeida, and Maria Pina Limongelli. Despite their demanding schedules, they consistently ensured that I received the support I needed, whether in person or via videocall. Their expertise in the subject fueled my passion and motivation throughout the work, and their consistently positive and encouraging attitude was deeply appreciated.

I would also like to extend my thanks to Catherine Doneux and Scott Menegon, who kindly offered their time to review this work and serve on my jury, as well as providing valuable materials for the thesis.

I am incredibly fortunate to have a family that has supported me in all my choices, especially during the challenging moments of this year. I am particularly grateful to my father for transmitting in me a passion for the fascinating world of civil engineering with an architectural perspective, to my mother for always being there for me providing a safe harbor, and to my sister for sharing life experiences and true friendship.

I am also deeply grateful to Elena, who has been by my side for many years. Despite the physical distance over the past two years, her love and happiness have been a constant source of encouragement.

Last but not least, I want to thank all the friends who have accompanied me on my university journey, from Politecnico di Milano to UCLouvain. Each one, with their diverse nationalities, personalities, and backgrounds, has been an important companion during these six years of university.

List of Figures

List of Tables

Contents

Chapter 1

Introduction

1.1 Context and motivation

Since the very beginning of the 19^{th} century, monitoring of existing structures was an important tool to understand their evolving characteristics over time and to ensure their safety.

With the development of technologies until nowadays, the number of instruments that were developed to this purpose increased exponentially, with extremely positive consequences on the control of structure's performances and behaviour. From extremely local measurements mainly focused on the quality of the structural material, the focus moved to diffused sensors throughout the structure, whose data were post-processed in a different phase. This approach allowed to have a more global overview on the structure and helped to adapt the programs of maintenance to its specific needs, preventing damage or even, in worst cases, structural failure.
Among the big group of instruments used, some are particularly devoted to monitoring of structures under seismic actions. This specific type of instrumentation, which will be discussed in this thesis, is normally grouped under the name of Seismic Structure Health Monitoring (S^2HM).

Today, more and more structures worldwide are being instrumented with sensors to understand how they behave under seismic events. This growth is due mainly to increasing interest from researchers and professionals as well as higher awareness on the importance of structural health from owners, occupants and users of the structures [29].

In this context, rising concern is developing in Australia due to total absence of information on how do structures designed based on Australian Codes AS 1170.4 provisions respond to seismic actions.
Despite the typically low seismicity of the Australian Plate, the island has experienced strong earthquakes in the past, resulting in damage and fatalities. Notably, the Newcastle earthquake in 1989 caused significant destruction.
Among the different regions in Australia, the Northern Territories are one of the closest to a plate border. In particular the city of Darwin, its capital, is 450 km

away from the Timor Trench, belonging to one of the most active tectonic borders: the so-called Ring of Fire.
Because of its position, Darwin is often rocked by long period earthquakes that can reach more than 7 on the magnitude scale.
For this reason, the Australian Earthquake Engineering Society is planning to equip a set of strategic structures with sensors in order to get information on their structural response under seismic actions.

1.2 Objectives

This thesis aims to support the program of Seismic Health Monitoring under which the Australian Earthquake Engineering Society is undergoing, by investigating the optimal placement of sensors on these structures.
Despite technologies related to SHM have been improved and made more economically affordable, the price is often a limitation that imposes how many sensors can be placed on the selected structure.
It becomes then of paramount importance to understand what is the optimal placement of these sensors to have the best quality of results on the structural behaviour.
There are several existing methods available in the literature to define the optimal location of the sensors. In this thesis, a method proposed by Limongelli, also supervisor of this work, has been used and expanded to a three-dimensional structure [28].
In particular, this method is based on defining the optimal positioning of sensors for reconstruction of seismic responses through a Cubic Spline Function interpolation. In this thesis, the method was expanded in order to consider also the torsional modes in the dynamical response, which previously were not taken into account, to have a better understanding of their influence on the ideal positioning of sensors.
The results provided not only suggestions for optimal placement of sensors in Australian Structures, but conclusions that are valid also for different structures worldwide.

1.3 Structure

This section is devoted to a brief overview of the most important steps followed in the current thesis.

1. The first Chapter is dedicated to a presentation of the seismicity of Darwin's region and the reasons leading to the necessity of a program of seismic monitoring. It is then presented a state of the art on Seismic Structure Health Monitoring, with a special attention on the different provisions and guidelines worldwide on the topic. Some of the most important parameters being used in the thesis are also presented, with an adequate theoretical background

2. In the second Chapter, an existing method of sensors' placement optimization was considered and expanded in order to take into account also of the torsional

modes. This generalized method can then be applied not only to extremely symmetric structures where just the flexural modes are relevant, but also to those with a highly torsional response

3. The following Chapter aimed to model, starting from a plan, what could be a classic Australian multi-storey building, with the purpose of studying it and validating the statements of the previous chapter.

4. In Chapter 5 the method was applied to an existing structure, the Atwood building, to have also a validation from a real structure and not just a numerical model.

5. In the final chapter, the conclusions of the previous chapters are collected and put together, with an eye on the future possible developments.

Important note: In this Master's Thesis, the AI tools ChatGPT from Open AI and LanguageTool were utilized to improve the text's quality, enhancing its clarity and readability.

Chapter 2

Literature review

2.1 Overview of the city of Darwin's seismicity

The Australian continent is generally classified as a Stable Continental Region (SCR) in terms of its plate tectonic setting and seismicity [11]. SCRs are defined as regions of continental crust that have not experienced any major tectonism, magmatism, basement metamorphism or anorogenic intrusion since the early Cretaceous and no rifting, major extension or transtension since the Palaeogene. The definition therefore is based on geology rather than seismic activity. Although earthquakes are rare in stable continental regions, they have the potential of causing enormous damage [35]. Indeed, also Australia historically was hit by strong earthquakes, which caused damage and deaths, e.g. the famous Newcastle's earthquake in 1989.

Looking at Figure 2.1 it can be easily detected that in Australia one of the closest region to a plate margin are the Northern Territories. In particular its capital, the city of Darwin, is located 450 km away from the Timor Trench, belonging to one of the most active tectonic borders: the so-called Ring of Fire. Hence, it is frequently affected by earthquakes originating from the offshore plate margin region of the Banda Sea.

In 1938, an estimated magnitude 8.6 earthquake occurred in the Banda Sea region [32], significantly larger than recent events. Although this quake was felt in Darwin, no major damage was reported. However, Darwin's building landscape has changed considerably since 1938, with significant urban and industrial growth. Larger structures, sensitive to longer-period ground motions, may now be at greater risk if a similar magnitude earthquake occurs again.

Since 2019, this region has experienced three significant earthquakes over magnitude 7.0, the largest being a magnitude 7.6 earthquake on January 10, 2023. Geoscience Australia received over 3,000 reports for this event, with some reports indicating minor structural and cosmetic damage [2]. Despite these earthquakes have not been causing major damage and deaths, higher magnitude earthquakes could occur in the region with greater effects.

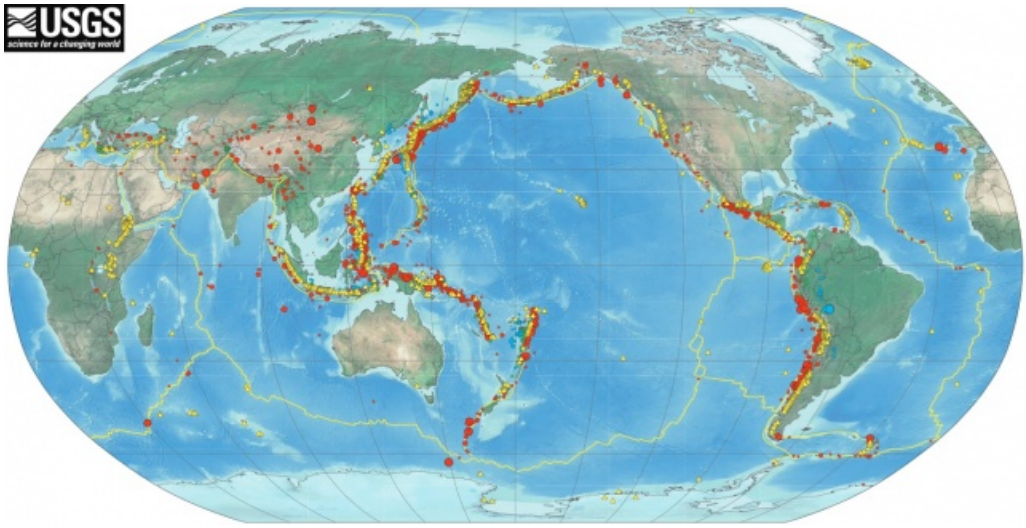

a) Events along the Ring of Fire: in yellow are the volcanoes and in red the earthquakes

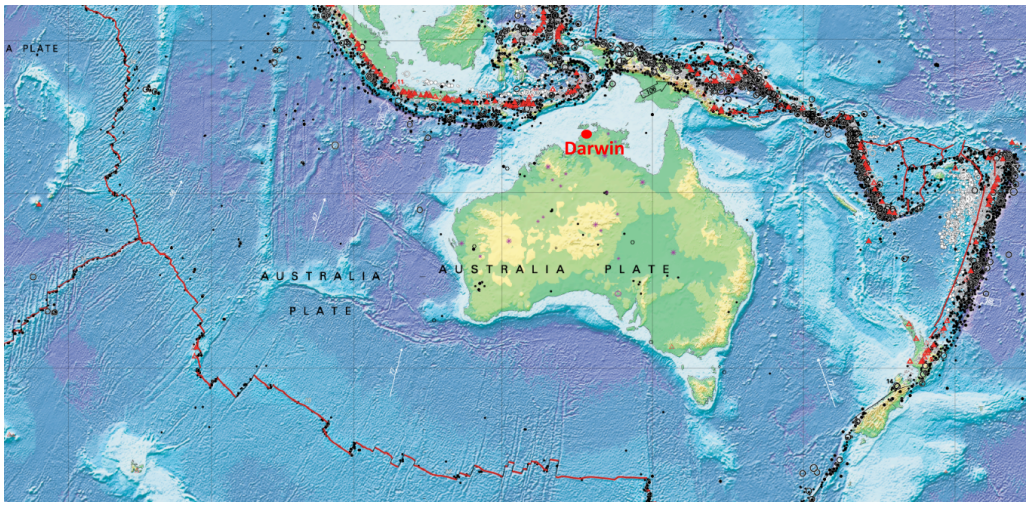

b) Australian Plate

Figure 2.1: Overview of the Ring of Fire (a) and detail of the Australian Plate with the city of Darwin (b) [44].

Given the potential for future great-magnitude earthquakes (magnitude 8+) in the Banda Sea region, it is crucial for engineers and seismologists to reassess current design actions and detailing requirements for structures in Darwin using data from real events [2].

Because of this, the Australian Earthquake Engineering Society (AESS) is implementing a program to instrument selected structures in the city of Darwin, to have a better control on their dynamic response under seismic actions. This work will have national significance and could benefit not only structures in the city of Darwin, but also new buildings throughout Australia designed to the AS 1170.4 standard, with all the advantages of Structure Health Monitoring presented in Section 2.2.

2.2 Seismic Structure Health Monitoring (S^2HM)

Structure Health Monitoring (SHM) encompasses all those methods that are devoted on monitoring a certain structure, on a global or local scale, in order to have an almost real-time idea on its health.
Depending on the purpose of the monitoring, SHM can be done with different types of sensors in different layouts. All the measurements of these sensors are then collected in a central unit that elaborates the data and can come out with an assessment of the structure [22].
The first applications of Structure Health Monitoring was on aircraft for damage identification in aerospace engineering and industry. In the late 1970s, however, it was implemented to investigate offshore platforms. At the beginning of the 1990s, SHM was extended to civil engineering and infrastructure systems [22].
With the high developments of technologies in the last two decades, there was a remarkable jump in the field with a more spread use of sensors for damage detection of bridges, buildings and other civil structures.

SHM is being used nowadays for monitoring structures under different types of loading:

- **wind loads**: specially for very slender structures such as skyscrapers and suspension bridges, wind can have important effects on the response of the structure, in particular in zones where typhoons are common. Nevertheless, SHM for wind actions is still associated to research programs and no generalized provisions have been developed yet, specially as each instrumented structure has its particularities and needs a specific study to optimize the position of sensors

- **seismic loads**: this field of SHM is often referred to as Seismic SHM, or S^2HM. The research in S^2HM is way more developed, leading to wide applications and guidelines throughout the world (see Section 2.2.2).

There are mainly two advantages that S^2HM have on traditional inspection techniques:

- on a short term, it provides a real-time assessment of the structure after an earthquake, detecting damage also when it is not possible to see it with a visual inspection because of fire proofing and finishes [29]

- on a long term, it offers important feedbacks on the behaviour of the structure under seismic actions, allowing to understand if the Code Provisions with which they were designed are correct and thus suggest a possible enhancing of future Design Standards

2.2.1 Sensoring

The present study focuses on optimizing the placement of accelerometers, which are the type of sensors most commonly used in S^2HM. Accelerometers measure the acceleration in one (uni-axial) or three (tri-axial) orthogonal dimensions and through

a system of cables, send the measured accelerations to a central system.
Accelerometers are the most widely used in current practice due to their cost-effectiveness, ease of installation, unobtrusive operation, and the ability to infer structural displacements by the double-integration of recorded acceleration data [37].
Nevertheless, many other sensors can be used and provide useful data. Below are listed the most common ones in SHM [19]:

- Linear Variable Differential Transformers (LVDTs) and inclinometer, used to directly measure mono-dimensional displacements and angular displacements
- strain gauges that are employed for strain and consequently stress measurements. Strains can also be measured continuously with Distributed Fiber Optic Sensing (DFOS)
- Liquid Levelling Sensors (LLS) for vertical displacement measurements, mainly used for bridges
- weather monitoring stations measuring temperature, humidity, wind and pressure

2.2.2 S^2HM around the world

Due to the high potential of S^2HM, many countries around the world decided to create special programs of instrumentations of strategic structures to have good knowledge on how do their structures behave under earthquakes actions.
In the following pages, a list of the most important programs of instrumentation and of guidelines around the world is presented.

2.2.2.1 USA

Probably one of the countries that invested more in the field, USA have been pioneers in S^2HM, and nowadays have in their regulation specific provisions on sensors positioning for strategic structures.

In the following, a list of the main steps done in the USA on S^2HM is shown:

- in 1997, for the first time some provisions on sensors' placement were published in the Uniform Building Code (UBC)[26]. In this document, it is recommended that any structure of more than 6 storeys with a total floor area of more than 5574 m^2 or more than 10 storeys located in seismic zones 3 and 4 must be equipped with at least three accelerographs. The instruments must be placed at least at the lowest level, at mid-height and near the top of the structure [26]. As shown in Figure 2.2.a, zones 3 and 4, depicted in the two darkest shades of orange, represent the areas of highest hazard. These zones are primarily concentrated along the Western Coast and the Centre of the country, with California exhibiting the highest hazard levels.

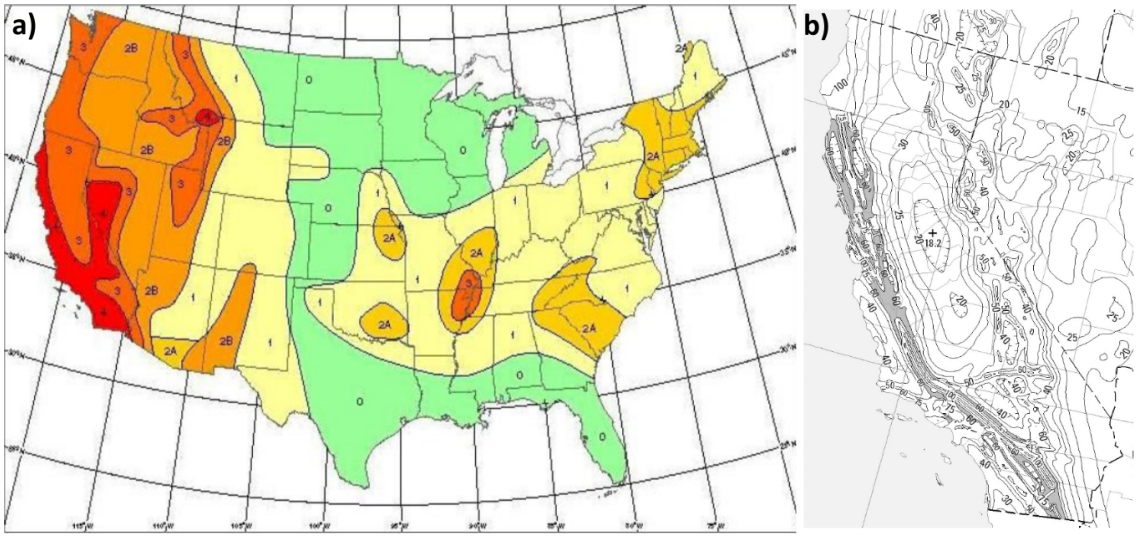

Figure 2.2: US seismic hazard map according to the UBC (a) [26] and value of S_1 according to the IBC for the state of California (b) [25].

- From the year 2000, the UBC was replaced by the International Building Code (IBC), a unified version of the three previous existing Codes in the USA. The IBC was developed by the International Code Council (ICC) with the purpose of having a unified code updated every three years [41]. Unless specifically referenced in the adopting ordinance and state, these guidelines are not mandatory.
  In this version of the Code, which is currently used, the hazard zoning is replaced with the so-called 1-second spectral response acceleration, or S_1. If this parameter is greater than 0.4 g (40% g), the same provisions previously applied to zone 3 and 4 in UBC have to be applied.
  In the IBC it is possible to find maps assessing the value of S_1 throughout the USA, which results to be a more precise zoning than the one previously defined in the UBC [25]. As an example, in Figure 2.2.b the zoning is shown, where lines with equivalent value of S_1 (expressed in percentage) can be detected.

- Other guidelines on sensors' placement were suggested by the United States Geological Survey (USGS), which has its own instrumentation program, called Advanced National Seismic System (ANSS). In these guidelines, more precise indications are provided on sensors placing [1]:

  1. A free-field sensor shall be provided near the structure to measure ground motion. This shall measure triaxial acceleration.
  2. One triaxial acceleration sensor should also be installed at the base of the structure at or below grade to measure "base motion."
  3. Sufficient acceleration sensors shall be distributed in the structure to resolve linear modal response (frequencies and gross mode shapes) based on the global response predicted for the structure. Both translation and torsion shall be considered. For the first, a distinction is done on the height of the structure. Regarding low-rise buildings up to three stories

in height, single-component sensors at the roof and at each intermediate level should be installed; on the other hand, for mid-rise buildings four to seven stories in height they should be at the roof and two intermediate levels while for high-rise buildings more than eight stories in height they should be at the roof, two intermediate levels and locations of stiffness discontinuities.
For torsional measurements, it is suggested installing pairs of single-component sensors at opposite ends of a floor plate at each instrumented level of a building. Differences between these measurements will estimate the torsional response.

4. Other sensors shall be distributed as required to measure important local responses, such as relative displacements. Sensors for local response need not be limited to accelerometers. Use of extensometers, strainmeters, and electronic distance measuring technology should be considered.

- Some guidelines have been given in the USA also from the non-profit Consortium of Organizations for Strong Motion Observation Systems (COSMOS) to optimally instrument tall buildings extensively. In the following are the main steps that should be followed to correctly place the sensors [12]:

  1. every instrumented floor should be equipped with three separated uniaxial accelerometers in order to account of torsional and translational effects
  2. to measure rocking in both directions three sensors should be placed at the base of the structure, in particular two on opposite walls of the structure and the third on one of the remaining walls
  3. accelerometers at different floors should be stacked vertically. In other words, they should be placed at the same relative position on each floor
  4. if there are unusual configurations of the roofing system or heavy machinery equipment, it would be convenient to place additional sensors
  5. different number of accelerometers should be placed based on the number of stories of the structure, as seen in Table 2.1:

Stories	**Minimum. #**	**Recommended #**
6-10	12	15
11-20	15	19
21-30	21	26
31-50	24	30
>50	30	38

Table 2.1: Minimum and recommended amount of accelerometers [12].

  6. apart from accelerometers, also other types of sensors can be useful to make relevant measures, specially in accounting interstorey drift

Following all these recommendations would be challenging and very costly in practice, but they are set as goals to aim for.
The just presented guidelines were also suggested by The Los Angeles Tall Buildings Structural Design Council (LATBSDC), a non-profit organization founded in 1988 whose main aim is to provide a forum for the discussion of issues relating to the design of tall buildings. This council published in 2023 an interesting document specifically referred to the optimal design of tall building, based on their interaction with other professional organizations, building departments, and university researchers [30]. Considering tall buildings those with a height higher than about 50 m, the document aims to give some specific information associated to tall buildings in those cases where the traditional regulation (IBC) could lead to a non-optimal design.

2.2.2.2 Japan

In Japan, although the Design Codes do not provide information on Structural Health Monitoring (SHM), the Building Research Institute (BRI) has undertaken an extensive instrumentation campaign. This initiative involves the installation of accelerometers on over 80 buildings throughout the country. [5].
One third of them are located in the zone of Tokyo. The program aims to investigate the dynamic behaviour of instrumented buildings under earthquakes and to use the obtained data for further research projects. BRI principally placed accelerometers at the top floor and at the basement of the buildings, and optionally on the nearby ground, for having a free field measurement [5].

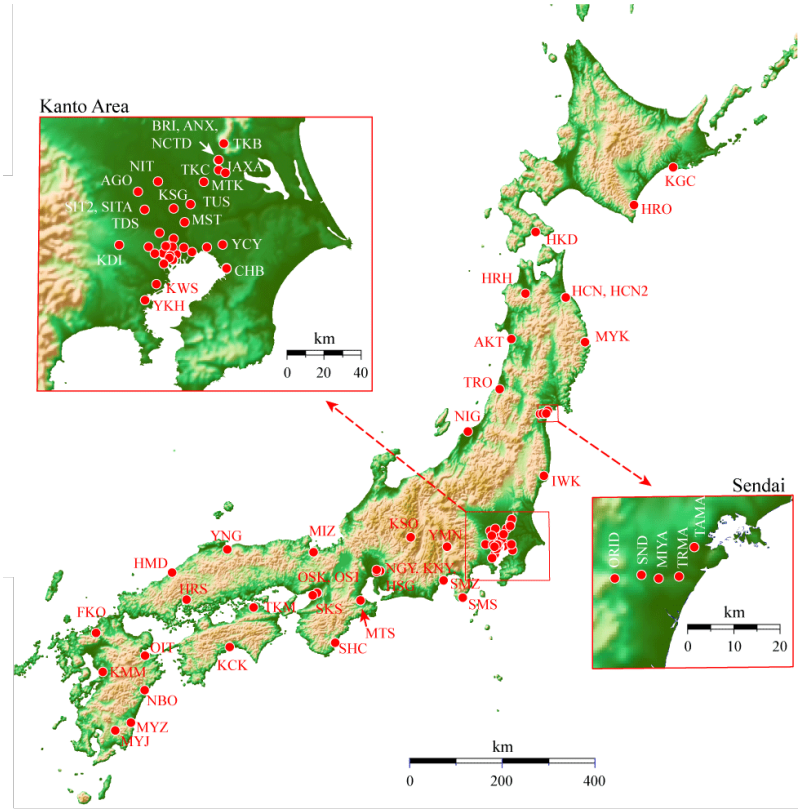

Figure 2.3: Japan's buildings equipped with sensors [5].

2.2.2.3 New Zealand

New Zealand, is a country often rocked by high magnitude earthquakes due to its position on the border of the Pacific and the Australian Plates. Despite this, there are no indications on the New Zealand's Standards (NZS 1170-5 Earthquake actions) on sensors positioning for S^2HM [39].
Still, New Zealand's GeoNet Service equipped in the so-called Structural Array program a total of 19 among buildings and structures with sensors. These sensors were often high fidelity solid state accelerometers, generally more precise than standard accelerometers, which have been supplemented with displacement sensors and multi-parameter weather stations [20].

For each specific case study, the GeoNet service was assisted by selected engineers who gave suggestions on the ideal positioning of sensors. Because of this, there are no general guidelines suggesting a specific sensors' layout. Nevertheless, by analysing research papers regarding instrumented structures in the country, some general points can be outlined [9] [43]:

- there is a general tendency to instrument relatively few structures but with a high amount of sensors
- these sensors are often placed at each floor of the structure

- more than one sensor is placed at the two extremes of the floor, to capture also the torsional response
- it is almost always present a free field accelerometer

Over the coming years, the GeoNet Building Instrumentation Programme aims to instrument a wider portfolio of buildings in New Zealand, with the objective of bringing its capabilities on par with similar initiatives in countries like the USA and Japan [9].

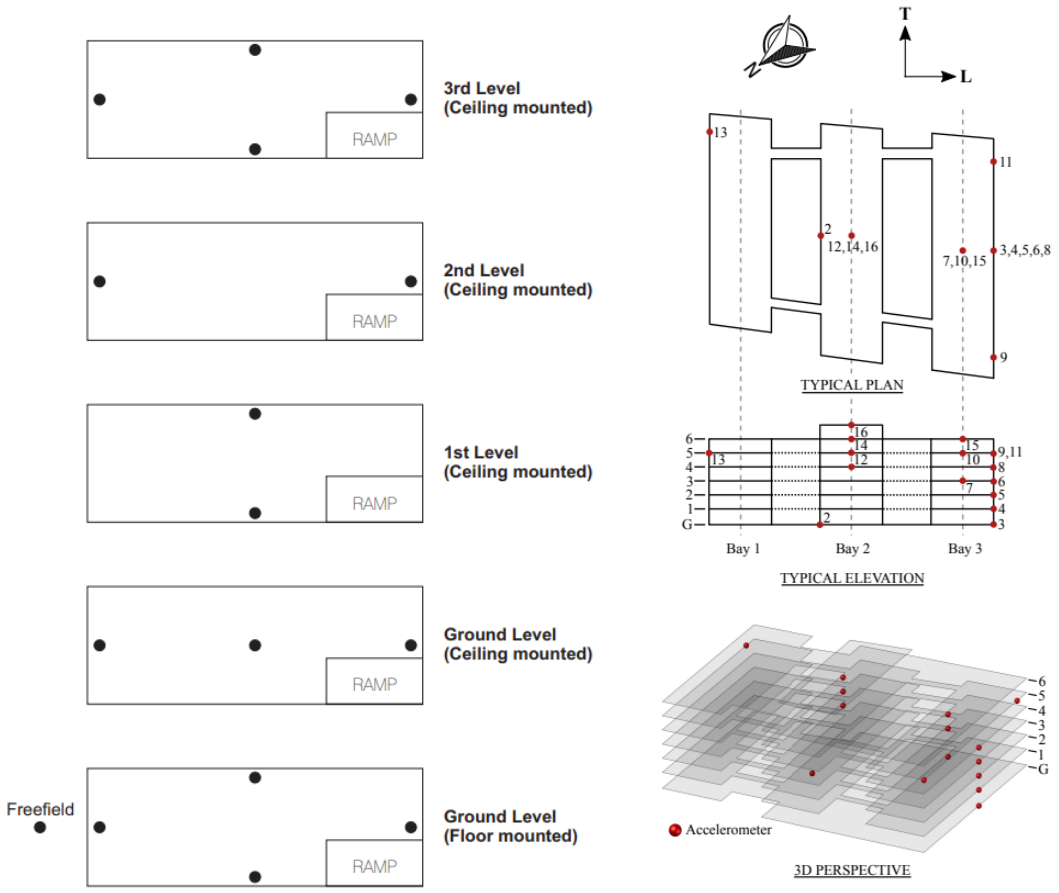

(a) Schematized layout [20] (b) Bank of New Zealand building [9]

Figure 2.4: New Zealand schematized guidelines (a) and an example of sensors layout on a existing structure (b).

2.2.2.4 Chile

In South America, Chile has by far on the most active seismic territory. In addition, the well-developed mining industry often induces important vibration due to the blasts it causes. To have an idea on how do structures respond to these actions, from 2009 Chile equipped more than 20 buildings with a low cost monitoring system, which consists in wireless MEMs accelerometers controlled via the internet network [29]. No specific information were found on the positioning of these sensors.

2.2.2.5 Philippines

In the Philippines, the Department of Public Works and Highways (DPWH) published in 2015 some guidelines to be followed in order to equip strategic buildings and to have a better idea of their response under seismic action. These guidelines took inspiration from the UBC provisions. Based on the type of building to be instrumented, two typologies of layout are proposed [14]:

- the placement of three sensors on the ground, on a middle floor and on the floor below the roof for hospitals, schools and other buildings higher than 50 m
- the placement of one accelerogram on the ground or on the lowest floor for all the other buildings

It is remarked that the guidelines specify that all the sensors should be placed on the same direction, which has to be of the principal one of the structure. Therefore, with this type of provisions torsional and rocking effects are not recorded.

2.2.2.6 Italy

For what concerns the Eurocodes, the collection of European Codes governing the construction sector, neither the current nor the new generation contain any provisions or recommendations regarding Structural Health Monitoring (SHM) practices. Nevertheless, many European countries such as Italy have equipped strategic buildings on their national territories to have relevant data about their response under seismic actions. For more information on S^2HM in Europe refer to Chapter 13 of Limongelli and Celebi's *Seismic Structure Health Monitoring* [29]. The following paragraphs report the main aspects presented in that publication.

In the framework of the national seismic risk prevention and mitigation policy, the Italian Department of Civil Protection (DPC) is engaged in numerous initiatives and projects related to the topic of S^2HM. The most important project in this field is the development and the management of the Osservatorio Sismico delle Strutture (OSS), a network of permanent seismic monitoring systems installed in 152 public buildings, 7 bridges and 3 dams, whose primary civil protection scope is to provide quasi-real-time remote information on the damage state of the monitored structures in case of an earthquake. The equipped buildings are schools, hospitals, town halls as well as churches, libraries and sports buildings. The distribution of equipped structures on the Italian territory is shown in Figure 2.5.

Regarding the methodology in which sensors are placed on the structures, a distinction has to be made.
First, all the bridges and dams had an ad hoc design of the accelerometers' layout, due to the particularity of their geometry and the uniqueness of each of these structures. On the other hand, two different types of monitoring systems related to buildings are found:

- a “complete” system: it is deployed in 129 buildings and it consists of a triaxial accelerometer placed on the ground level to which is added a set of at least three uniaxial accelerometers per floor, to capture torsion
- a “simplified” system: it is deployed in 22 buildings. In this case just the top floor is instrumented apart from the triaxial accelerometer on the ground

It is also remarked that an hybrid between these two systems can be found in the town hall of Recanati.

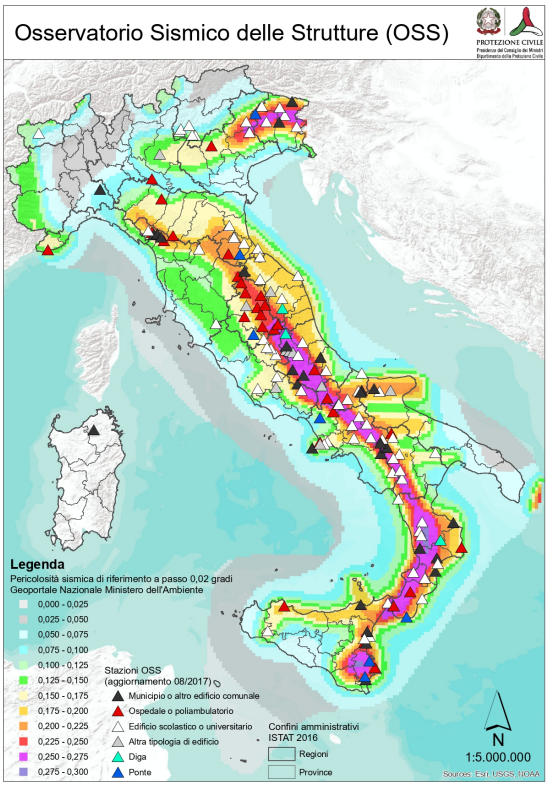

Figure 2.5: OSS distribution of equipped structures [29]

2.2.2.7 France

Since 2009 in France the Permanent Accelerometer Network (PAN) launched a program named National Building Array Program (NBAP) consisting in placing a set of accelerometers on five buildings in French territories. Data from these sensors once recorded are then freely accessible to the public. The distribution of sensors over the buildings does not follow a standard criterion but has been designed ad hoc for each structure. Nevertheless, in all the cases a triaxial accelerometer is found on the ground floor, together with several uniaxial accelerometers at different floors to take into account of torsion and inter-storey drift [29].

2.2.2.8 Greece

In Greece the Institute of Engineering Seismology and Earthquake Engineering (ITSAK) has been active in seismic monitoring since its foundation in 1979. In this

country, the attention was mainly dedicated to installing ground sensors to monitor the seismic action. Just a few buildings were equipped with a system of sensors in order to measure their response under this seismic action. According to some examples found in the literature [29], the instrumented structures were usually low rise buildings which were equipped at almost each floor with three uniaxial sensors to capture flexure and torsion.

2.2.2.9 Portugal

SHM in Portugal was mainly used to account of historical constructions and monuments response as they give the possibility to continuously track the structural health of the system under observation without resorting to any invasive technique, despite the numerous challenges associated with such complex structures. Even if these structures would need a wide amount of sensors to be well studied due to their elaborate geometry, normally they are equipped with two triaxial accelerometers, one on the ground and one on the top of the structure [29].

2.2.2.10 Comparison

In the previous pages, the main programs of Seismic Structural Health Monitoring throughout the world were presented, showing how in different ways several countries are gradually instrumenting their structures.
Table 2.2 provides a summary of the parameters that each SHM program or guideline can capture, based on information found in the literature. Since no precise guidelines or specific examples of instrumented structures were found in Chile, it was not included in the table.

From Table 2.2, it is observed that all national programs dedicate a big importance to recording the base motion of the structure. Having a free field station allows also to have a better idea on the influence of soil without being affected by soil-structure interaction. The most complete set of guidelines is the one presented by COSMOS and LATBSDC, which is presented in Figure 2.6. This layout suggests an extensive sensor deployment, which, while providing comprehensive monitoring of the instrumented structure's behaviour, also comes with significant financial costs. Because of this, large programs of instrumentation such as the ones seen in the USA and Japan often involve simplified layouts to reduce costs.
Nonetheless, this layout is particularly well-suited for SHM campaigns focused on research objectives. In chapter 5, for instance, the considered Atwood building was instrumented accordingly to these provisions.
In that case, in order to capture also the inter-storey drift, couples of adjacent floors were equipped.

Program/Guidelines	Number of sensors	Base motion	Free field	Interstory drift	Torsion	Rocking
USA-UBC & IBC	3					
USA-ANSS	Depending on the stories					
USA-COSMOS & LATBSDC	Depending on the stories					
Japan	3 or 2					
New Zealand	Not specified					
Philippines	3 or 2					
Italy-complete	3 uniaxial per floor					
Italy-simplified	2					
France	Not specified					
Greece	Not specified					
Portugal	2 triaxial					

Table 2.2: Summary of parameters captured by the various guidelines and programs found in the literature. When the cells are filled in green, it means that the respective guidelines suggest a sensor layout that captures the parameter. Conversely, if the cell is red the parameter is not captured following these guidelines.

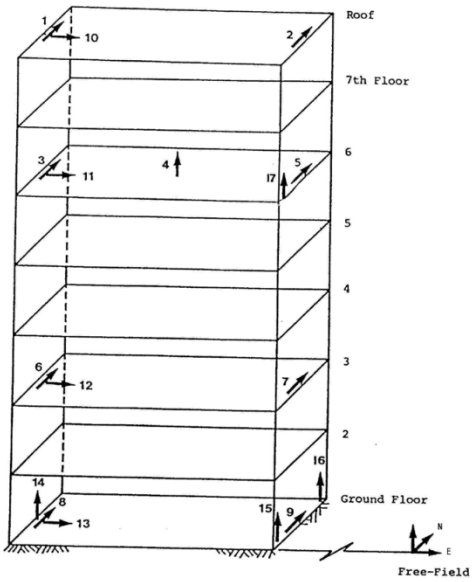

Figure 2.6: Ideal sensors' layout: there is a free field station, some accelerometers at the base to record base motion (8, 9 and 13), three vertical accelerometers at the base to measure rocking in the two directions (14, 15 and 16), couples of accelerometers at the same floors to capture torsion (6-7, 3-5, 1-2) [12].

2.2.3 Existing methods for Optimal Sensors Positioning

The methods presented in the literature for the definition of Optimal Sensors Positioning (OSP) represent a wide part of the literature regarding SHM. Due to the

reduced available space, in this thesis just the main criteria and optimization techniques will be presented, with a special attention to the one used in this work. According to Tan and Zhang [40], the possible evaluation criteria that can be used for sensors optimization are the following:

- modal assurance criterion (MAC)
- Fisher information matrix (FIM)
- information entropy (IE)
- effective independence (EI)
- effective independence driving-point residue (EFI-DPR)
- energy-based criteria

These criteria, further discussed in [40], provide a parameter that has to be maximized or minimized in the optimization process in order to arrive to the optimal sensors' layout.

The optimization process is also not unique, as different algorithms can be implemented to reach the optimal layout satisfying at best the just presented criteria. The most important groups of optimization process algorithms are [40]:

- evolutionary optimization methodologies: are based on a principle of evolution (i.e. the survival of the fittest), constitute a critical category of heuristic search
- sequential sensor placement (SSP): usually divided into two types, namely forward sequential sensor placement (FSSP) and backward sequential sensor placement (BSSP)
- deterministic optimization methodologies: ideal for SHM with simple and regular shapes such as beam and plates
- probability-based methodologies: based on the use of Bayesian theory to determine sensors configuration
- other optimization methodologies: such as the use of Snobfit, the Kalman filter algorithm, Machine Learning (ML) and other procedures (see [40] for a more comprehensive overview)

The methods presented can be used in different situations based on the optimization that has to be done and on the analysed structure.
In this paper, a method based on cubic spline interpolation to get unknown response is used, where the criterium is the minimization of a γ function obtained starting from the modal shapes and the mass distribution of the structure [28]. In the following section, the modal parameters used in the development of the method are introduced, and then further discussed in Chapter 3.

2.3 Theoretical background

A structure experiencing seismic excitation undergoes complex dynamic responses. Therefore, this section aims to provide a comprehensive overview of the fundamental principles and key aspects governing the dynamic behaviour of structures, starting from the governing equation until the definition of the parameters being used in this paper.
The topic is extremely wide and could be largely discussed. Nevertheless, just the parts relevant to the work of this thesis will be presented. For a deeper insight on the topic of Dynamics of Structure refer to Chopra's *Dynamics of Structures* [10], main source for this paragraph.

2.3.1 Single Degree of Freedom systems (SDoF)

Consider an extremely simple structure as the one in Figure 2.7. This structure can be used to represent, schematically, a one-story frame. The whole mass of the structure is lumped in one point, the stiffness is provided by the frame and a viscous damper acts to dissipate the energy of the system.

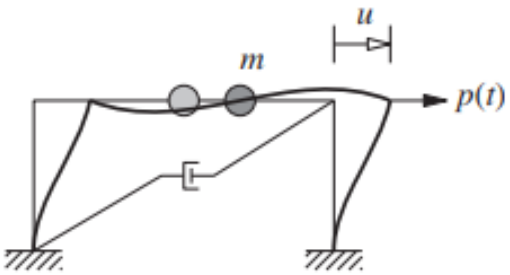

Figure 2.7: Single Degree of Freedom structure [10].

As the columns are considered to be axially inextensible, the position of the mass if the structure is being pushed by a force *p(t)* can be described by a single displacement in horizontal. Thus, the frame is considered to be a One Degree of Freedom system.
Starting from the Newton's Second Law of Motion, the forces acting on the mass can be expressed as follows:

$$p(t) - f_D - f_S = m\ddot{u}(t) \qquad \text{or} \qquad f_t + f_D + f_S = p(t) \tag{2.1}$$

where $p(t)$ is the applied external force, $f_S = ku(t)$ is the stiffness component depending on the displacement, $f_D = c\dot{u}(t)$ is the damping component depending on the velocity and $f_t = m\ddot{u}(t)$ is the mass component depending on the acceleration.
In the case in which the force $p(t)$ is due to a seismic action, Equation 2.1 becomes:

$$m\ddot{u}(t) + c\dot{u}(t) + ku(t) = -m\ddot{u}_g(t) \tag{2.2}$$

where $\ddot{u}_g(t)$ is the ground acceleration.
To define the problem completely, some initial conditions have also to be defined,

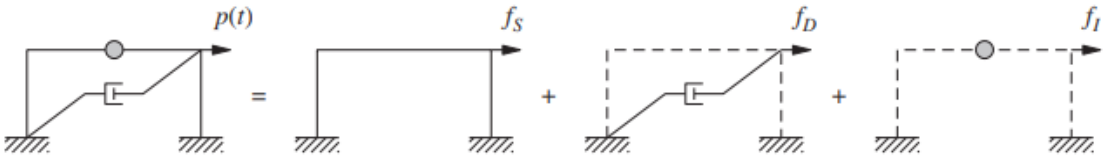

Figure 2.8: All the forces in the equation of motion of a SDoF system [10].

which are usually a condition on the initial displacement $u(0)$ and initial velocity $\dot{u}(0)$.

2.3.2 Multi Degree of Freedom systems (MDoF)

The concepts above can be generalized for a Multi Degree of Freedom system, which has multiple directions of possible movement and therefore need multiple variables to describe its displacement in space.
First, the simpler case of an undamped system under free vibration can be considered. Free vibration is a particular state in which there is no applied force $\mathbf{p(t)}$ on the system, and the dynamic motion is induced by disturbing the initial state of equilibrium by imposing initial conditions on displacement and velocities. The resulting dynamic equation of motion would be the following:

$$\mathbf{m}\ddot{\boldsymbol{u}}(\boldsymbol{t}) + \mathbf{k}\boldsymbol{u}(\boldsymbol{t}) = \mathbf{0} \tag{2.3}$$

where the mass matrix $\mathbf{m}$ and the stiffness matrix $\mathbf{k}$ are NxN matrices, with N corresponding to the number of degrees of freedom. The equation can be solved with adequate initial conditions:

$$\begin{cases} \boldsymbol{u}(\mathbf{0}) = \boldsymbol{u_0} \\ \dot{\boldsymbol{u}}(\mathbf{0}) = \dot{\boldsymbol{u}}_\mathbf{0} \end{cases} \tag{2.4}$$

The displacement of the structure can be described in modal coordinates as:

$$\boldsymbol{u}(\boldsymbol{t}) = \sum_{r=1}^{N} \boldsymbol{u}^{(\boldsymbol{r})}(t) = \sum_{r=1}^{N} q^{(r)}(t)\boldsymbol{\phi}^{(\boldsymbol{r})} \tag{2.5}$$

corresponding to the sum of all the contributions given from the N natural modes of vibration associated to the N deflected shapes $\boldsymbol{\phi}^{(\boldsymbol{r})}$. It is remarked that $\boldsymbol{\phi}^{(\boldsymbol{r})}$ does not vary with time. The time variation of the displacements is described by the simple harmonic function:

$$q^{(r)}(t) = A^{(r)}\cos(\omega^{(r)}t) + B^{(r)}\sin(\omega^{(r)}t) \tag{2.6}$$

where $A^{(r)}$ and $B^{(r)}$ are constants that can be determined from the initial conditions in Equation 2.4. Combining Equations 2.5, considering a single mode r, and 2.6:

$$\boldsymbol{u}^{(r)}(t) = \left(A^{(r)}\cos(\omega^{(r)}t) + B^{(r)}\sin(\omega^{(r)}t)\right)\boldsymbol{\phi}^{(\boldsymbol{r})} \tag{2.7}$$

where the modal shape $\phi^{(r)}$ and the natural frequency $\omega^{(r)}$ tied to a specific mode r are unknown. Substituting this form of $\boldsymbol{u^{(r)}}(t)$ and its derivatives in Equation 2.3 gives:

$$\left[-\omega^{(r)^2}\mathbf{m}\boldsymbol{\phi}^{(r)} + \mathbf{k}\boldsymbol{\phi}^{(r)}\right] q^{(r)}(t) = 0 \tag{2.8}$$

To be satisfied, the solutions are two. The first, called trivial solution, is $q^{(r)}(t) = 0$, which implies that $u^{(r)}(t) = 0$ and there is no motion of the system. The second, such that the following algebraic equation is satisfied:

$$\mathbf{k}\boldsymbol{\phi}^{(r)} = \omega^{(r)^2}\mathbf{m}\boldsymbol{\phi}^{(r)} \tag{2.9}$$

also expressed as:

$$\left[\mathbf{k} - \omega^{(r)^2}\mathbf{m}\right] \boldsymbol{\phi}^{(r)} = 0 \tag{2.10}$$

This algebraic equation is called the matrix Eigenvalue Problem. The stiffness and mass matrices k and m are known; the problem is to determine the scalar $\omega^{(r)^2}$ and the vector $\boldsymbol{\phi^{(r)}}$. The non-trivial solution can be found imposing:

$$\det\left[\mathbf{k} - \omega^{(r)^2}\mathbf{m}\right] = 0 \tag{2.11}$$

When the determinant is expanded, a polynomial of order N in $\omega^{(r)^2}$ is obtained. This equation, defined as the characteristic equation, has N real and positive roots for $\omega^{(r)^2}$ because $\mathbf{m}$ and $\mathbf{k}$, the structural mass and stiffness matrices, are symmetric and positive definite.
Physically, $\omega^{(r)}$ corresponds to the natural frequency or the r-th mode of vibration. When a natural frequency $\omega^{(r)}$ is known, Equation 2.9 can be solved for the corresponding vector $\boldsymbol{\phi^{(r)}}$ to within a multiplicative factor. The eigenvalue problem does not fix the absolute amplitude of the vectors $\boldsymbol{\phi^{(r)}}$, but only its shape.

Modal and spectral matrices

The N eigenvectors can be assembled compactly in a single square matrix $\mathbf{\Phi}$, called modal matrix, wherein each column is a natural mode. Similarly, the N eigenvalues $\omega^{(r)^2}$ can be assembled into a diagonal matrix $\mathbf{\Omega^2}$, called spectral matrix. Therefore, it is possible to assemble all the N relations corresponding to each mode r from Equation 2.9 into a single equation:

$$\mathbf{k\Phi} = \mathbf{m\Phi\Omega^2} \tag{2.12}$$

Orthogonality of modes

It can be proven that the following mode orthogonality conditions hold when $\omega^{(i)} \neq \omega^{(j)}$:

$$\boldsymbol{\phi}^{(i)^T}\mathbf{k}\boldsymbol{\phi}^{(j)} = 0 \qquad \boldsymbol{\phi}^{(i)^T}\mathbf{m}\boldsymbol{\phi}^{(j)} = 0 \tag{2.13}$$

The orthogonality of natural modes implies that the following square matrices are diagonal:

$$\mathbf{K} \equiv \mathbf{\Phi}^T\mathbf{k\Phi} \qquad \mathbf{M} \equiv \mathbf{\Phi}^T\mathbf{m\Phi} \tag{2.14}$$

where the diagonal elements are:

$$K^{(i)} = \boldsymbol{\phi}^{(i)^T}\mathbf{K}\boldsymbol{\phi}^{(i)} \qquad M^{(i)} = \boldsymbol{\phi}^{(i)^T}\mathbf{M}\boldsymbol{\phi}^{(i)} \tag{2.15}$$

Since $\mathbf{M}$ and $\mathbf{K}$ are positive definite, the diagonal elements of $\mathbf{K}$ and $\mathbf{M}$ are positive and they are related by:

$$K^{(i)} = \omega^{(i)^2} M^{(i)} \tag{2.16}$$

Normalization of modes

As mentioned before, the eigenvalue problem defines the natural modes to only within a multiplicative factor. It is thus possible to apply scale factors to these natural modes mantaining their shape. This process is called normalization and can be done in many different ways.

One of the most commonly used procedure of normalization is the following, where the modal shapes are normalized with respect to the mass matrix. For each mode r the quantity:

$$M_n^{(r)} = \boldsymbol{\phi}^{(\boldsymbol{r})^T}\mathbf{m}\boldsymbol{\phi}^{(\boldsymbol{r})} \tag{2.17}$$

is computed, and the normalized modal shapes $\boldsymbol{\phi}_{\boldsymbol{n}}^{(\boldsymbol{r})}$ are found as

$$\boldsymbol{\phi}_{\boldsymbol{n}}^{(\boldsymbol{r})} = \frac{\boldsymbol{\phi}^{(\boldsymbol{r})}}{\sqrt{M_n^{(r)}}} \tag{2.18}$$

in such a way that $M_n^{(r)} = \boldsymbol{\phi}^{(\boldsymbol{r})^T}\mathbf{m}\boldsymbol{\phi}^{(\boldsymbol{r})} = 1$ holds for all N modes, or also:

$$\boldsymbol{\Phi}^{\mathbf{T}}\mathbf{m}\boldsymbol{\Phi} = \mathbf{I} \tag{2.19}$$

where $\mathbf{I}$ is the identity matrix with unit values along the main diagonal. It is said that the natural modes are thus not only orthogonal but also normalized, thus defined as a mass orthonormal set.

System under a seismic action

In the case damping is also introduced and the system is subjected to a seismic action, Equation 2.3 becomes:

$$\mathbf{m}\ddot{\boldsymbol{u}}(t) + \mathbf{c}\dot{\boldsymbol{u}}(t) + \mathbf{k}\boldsymbol{u}(t) = -\mathbf{m}\mathbf{J}\ddot{u}_g(t) \tag{2.20}$$

where $\mathbf{c}$ is the NxN damping matrix and $\mathbf{J}$ is defined as the influence vector containing 1 in the equations corresponding to the DoF influenced by the ground acceleration $\ddot{u}_g(t)$.

Expressing the equation in modal coordinates and pre multiplying all the elements by a generic $\phi^{(\mathbf{r})^{\mathbf{T}}}$:

$$\boldsymbol{\phi}^{(\boldsymbol{r})^T}\mathbf{m}\boldsymbol{\phi}^{(\boldsymbol{r})}\ddot{\boldsymbol{q}}(t) + \boldsymbol{\phi}^{(\boldsymbol{r})^T}\mathbf{c}\boldsymbol{\phi}^{(\boldsymbol{r})}\dot{\boldsymbol{q}}(t) + \boldsymbol{\phi}^{(\boldsymbol{r})^T}\mathbf{k}\boldsymbol{\phi}^{(\boldsymbol{r})}\boldsymbol{q}(t) = -\boldsymbol{\phi}^{(\boldsymbol{r})^T}\mathbf{m}\mathbf{J}\ddot{u}_g(t) \tag{2.21}$$

Exploiting the condition of orthogonality of modes and dividing for each mode by the corresponding element of the diagonal matrix $\mathbf{M}$ as defined in Equation 2.15,

Equation 2.21 can be written as N uncoupled equations.
For a generic mode r:

$$\ddot{q}^{(r)}(t) + 2\zeta^{(r)}\omega^{(r)}\dot{q}^{(r)}(t) + \omega^{(r)^2}q^{(r)}(t) = -\alpha^{(r)}\ddot{u}_g(t) \tag{2.22}$$

where $\alpha^{(r)}$ is defined as the participation factor for the generic mode r, and is computed as:

$$\alpha^{(r)} = \frac{L_i^{(r)}}{M^{(r)}} = \frac{\boldsymbol{\phi^{(r)^T}\mathbf{m}\mathbf{J}}}{\boldsymbol{\phi^{(r)^T}\mathbf{m}\phi^{(r)}}} \tag{2.23}$$

If equation 2.22 is then multiplied by the i-th component of the r-th modal shape, it is obtained the contribution of the mode to the displacement at the i-th coordinate:

$$\phi_i^{(r)}\ddot{q}^{(r)} + 2\zeta_r\omega_r\phi_i^{(r)}\dot{q}^{(r)} + \omega_r^2\phi_i^{(r)}q^{(r)} = -\phi_i^{(r)}a_r\ddot{x}_g \tag{2.24}$$

$$\ddot{x}_i^{(r)} + 2\zeta_r\omega_r\dot{x}_i^{(r)} + \omega_r^2x_i^{(r)} = -\beta_i^{(r)}\ddot{x}_g \tag{2.25}$$

where $\beta_i^{(r)}$ is the so-called i-th component of the effective participation factor for the r-th modal shape, that will be further discussed in Chapter 3.

Effective modal mass and effective modal height

Many different parameters useful to describe the dynamic behaviour of a structure could be introduced in the current paper.
Nevertheless, just the one used in the thesis are presented.
The base shear effective modal mass, or for brevity the effective modal mass, indicates the mass that contributes to have the base shear for a general mode r. The modes that have thus the highest influence on the dynamic response of the structure will display a higher value of the effective modal mass. It is defined as:

$$M_{eff}^{(r)} = \alpha^{(r)}L_i^{(r)} = \frac{L_i^{(r)^2}}{M^{(r)}} \tag{2.26}$$

for which it happens that

$$\sum_{r=1}^{N} M_{eff}^{(r)} = \sum_{i=1}^{N_f} m_i \tag{2.27}$$

where N_f is the total number of floors in the structure and m_i is the mass of the i-th floor.
To compute the base overturning moment, an additional parameter has to be introduced: the base-moment effective modal height, or simply the effective modal height. Physically, it can be seen as the distance from the base of the structure at which the effective modal mass has to be applied to produce the base overturning moment of the mode r. It is defined as follows [33]:

$$h_{eff}^{(r)} = \frac{\sum_{i=1}^{N_f} h_i m_i \phi_i^{(r)}}{\sum_{i=1}^{N_f} m_i \phi_i^{(r)}} \tag{2.28}$$

for which is happens that

$$\sum_{r=1}^{N} h_{eff}^{(r)} M_{eff}^{(r)} = \sum_{i=1}^{N_f} h_i m_i \tag{2.29}$$

where h_i is the height at which mass m_i is applied.
Unlike $\alpha^{(r)}$ and $\beta_i^{(r)}$ the two just introduced parameters are independent on how the mode is normalized.

Chapter 3

3D method of sensors optimization

In the current chapter, an existing method of sensors placement optimization in a multi-storey structure is presented. This method was developed by Professor Limongelli, supervisor of this thesis, and simplifies a generic 3D structure (such as the one in Figure 3.1.a) to a 2D frame (such as the one in Figure 3.1.b), considering thus just the flexural modes of the frame [28].
For symmetric structures without important torsional behaviour, this method can well estimate the optimal positioning of the sensors, as the flexural modes well approximate the actual dynamic response.
Nevertheless, for a torsionally flexible building, a 2D model can be too simplistic. Torsional modes can have an important contribution in these situations, leading to the need of a wider method, that takes into account also of these modes.
The influence of these modes in sensors placement throughout the structure before this work was still unknown. In this thesis a wider method is proposed, with the aim to consider not just the flexural modes in one direction (X-axis in 3.1), but also of the ones in the orthogonal out-of-plan direction (Y-axis in 3.1) and of the torsional modes.

3.1 Existing 2D method

For the purpose of the work conducted in this section, the conclusions that were drawn from the publication by Limongelli [28] were replicated. This replication study was ultimately conducted to have a better understanding of the formulations and the steps involved in the method.
At the time of the publication (2003) the Software FORTRAN was used for coding and SAP2000 for the FE models. In this thesis, MATLAB was chosen for coding and Seismostruct for the FE models.
To avoid excessive repetition from the mentioned article [28], in this paper just the main conclusions are presented. The reader in this thesis is also given an appropriate contextualization of the 2D method with all the needed formulations to fully understand the 3D one. For a more comprehensive understanding of all the steps, it is in any case recommended consulting the original article.

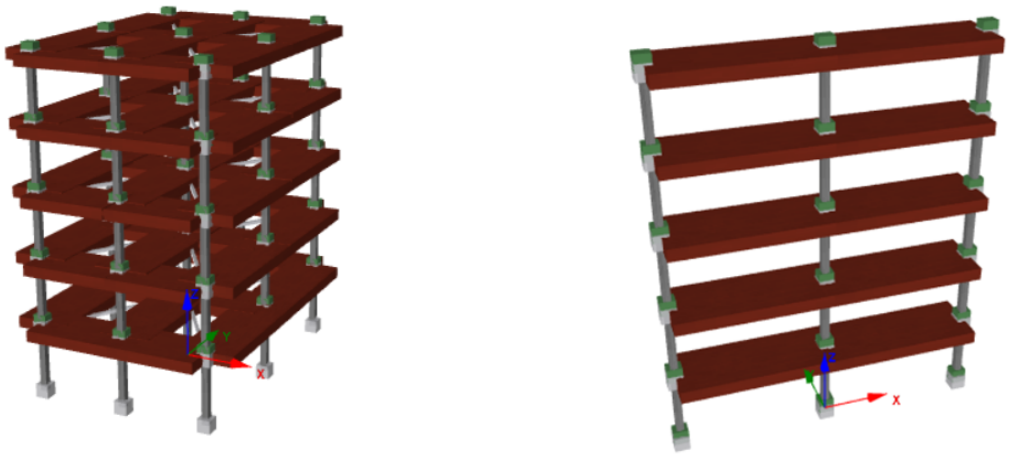

(a) 3D structure (b) 2D frame structure in XZ plane.

Figure 3.1: Example of real structure (a) and its simplified 2D (b) version.

3.1.1 Model formulation

In the work by Limongelli [28], the technique used to reconstruct unknown signals from a limited number of known measured accelerations is based on the use of cubic spline functions interpolation (see Appendix A). By interpolating the known accelerations with these functions, you gain the advantage of minimizing the overall curvature compared to other twice-differentiable alternatives. This approach helps prevent the wild oscillations that can occur with certain interpolation methods, such as polynomial ones. [13].
It is assumed that the base input acceleration $\ddot{u_g}(t)$ is known, and taking into account adequate boundary conditions (see Table 3.1), where x is the relative displacement and u_g is the displacement due to the ground motion, the floors of known measured accelerations are assumed as the knots of the cubic spline function. It is noted that the boundary conditions in Table 3.1 refer to a cantilever behaviour of the structure, which is a common approximation for multi-storey buildings. In the specific case where the top storey's response $\ddot{u_H}(H,t)$ is known, the condition of $\ddot{u}'''(H,t)$=0 is replaced by $\ddot{u}(H,t) = \ddot{u_H}(H,t)$.

	Absolute displacement $u = x + u_g$	**Absolute acceleration** $\ddot{u} = \ddot{x} + \ddot{u}_g$
$z = 0 \forall t$	$u(0,t) = u_g(t)$ $u'(0,t) = 0$	$\ddot{u}(0,t) = \ddot{u}_g(t)$ $\ddot{u}'(0,t) = 0$
$z = H \forall t$	$u''(H,t) = 0$ $u'''(H,t) = 0$	$\ddot{u}''(H,t) = 0$ $\ddot{u}'''(H,t) = 0$

Table 3.1: Cantilever boundary conditions for a multi-storey building.

To validate the method, three numerical models of 5, 10 and 20 floors were created. They consist of simple 2D frames with two bays of 6 meters each and 3 meters between storeys as seen in Figure 3.2.

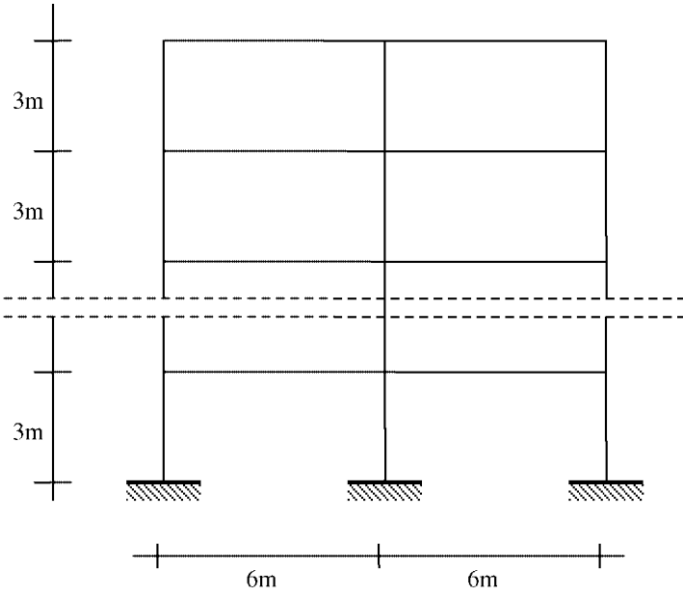

Figure 3.2: Geometry of analysed frames [28].

The structures are considered as shear buildings with the following characteristics: fixed supports on rigid ground (so same acceleration applied on all the base nodes), infinitely rigid and incompressible beams (so same horizontal displacement at the top of each column), lumped masses at each floors. Indeed, all the masses of the structure, even the one of the columns, are lumped in the three nodes of each floor, according to Table 3.2.
Consequently, the material used in the numerical model for all the structural members are considered massless.

	Side nodes [tons]	**Central nodes [tons]**
Roof	1.34	2.34
Other floors	1.68	2.68

Table 3.2: Mass distribution throughout the structure.

The resulting mass matrix was then a diagonal N_fxN_f matrix, where N_f is the number of floors of the building, with on the diagonal the sum of each floor's masses which is $m_1 = m_2 = ... = m_{N_f-1}$=6.04 tons for all the floors, except for the roof, with a total mass m_{N_f}=5.02 tons. The resulting mass matrix is the following:

$$\boldsymbol{m} = \begin{bmatrix} m_1 & 0 & 0 & \cdots & 0 \\ 0 & m_2 & 0 & \cdots & 0 \\ 0 & 0 & m_3 & \cdots & 0 \\ \vdots & \vdots & \vdots & \ddots & \vdots \\ 0 & 0 & 0 & \cdots & m_{N_f} \end{bmatrix} \tag{3.1}$$

Running an eigenvalue analysis, the modal shapes Φ_i^r were extracted. They were then normalised with respect to the mass matrix as presented in Chapter 2, such

that:

$$\boldsymbol{\phi_n^{(r)^T} m \phi_n^{(r)}} = 1 \tag{3.2}$$

After the normalization, the previously introduced effective participation factors β_i^r were computed. These factors describe the contribution of each mode r at each location i. A 2D model of the structure has been assumed, for which only flexural modes in the plane of the frame are considered (N of modes=N of floors). The displacement at the i-th storey can be written in terms of the modal contributions as follows:

$$x_i(t) = \sum_{r=1}^{N} x_i^{(r)}(t) = \sum_{r=1}^{N} \alpha^{(r)} \phi_i^{(r)} D^{(r)}(t) = \sum_{r=1}^{N} \beta_i^{(r)} D^{(r)}(t) \tag{3.3}$$

The effective participation factor β_i^r of a mode r and location i is defined as the product between the r-th modal participation factor α^r and the i-th component of the r-th modal shape $\phi_i^{(r)}$. The displacement at the i-th storey is obtained by multiplying it by the r-th modal response to the base excitation $D^{(r)}$.

The sum $s(N_m, i)$ of the effective participation factors of N_m modes in the generic i-th location is:

$$s(N_m, i) = \sum_{r=1}^{N_m} \beta_i^{(r)} \tag{3.4}$$

where N_m is the number of modes considered. In the particular case in which $N_m = N$ the function $s(N, i)$ converges at 1. To measure the distance between function $s(N_m, i)$ and unity for a generic considered number of modes N_m, the following function is defined:

$$\gamma(N_m, i) = 1 - s(N_m, i) \tag{3.5}$$

The gamma function is a measure of the importance on the response at the i-th location, of the modes neglected in the summation. The higher gamma, the higher the importance of such modes. Conversely, the lower gamma, the higher the importance of the N_m considered modes, on the response at the same location. The lowest values of gamma identify the locations where the N_m considered modes provide most of the contribution to the response or, in other words, where the neglected modes have the lowest influence. Figures 3.3, 3.4 and 3.5 show that for a number of considered modes $N_m < \frac{N}{2}$, where N is the total number of modes for the structure, the absolute value of the $\gamma(N_m, i)$ function normalized to its maximum value presents N_m points of local minimum. These points of local minimum represent the positions where the higher modes have less influence. Placing N_m sensors in these N_m points of local minimum would allow capturing the contributions of the modes that most affect the response at those locations. They are then the ideal nodes to reconstruct the dynamic response of the structure with a cubic spline function interpolation.

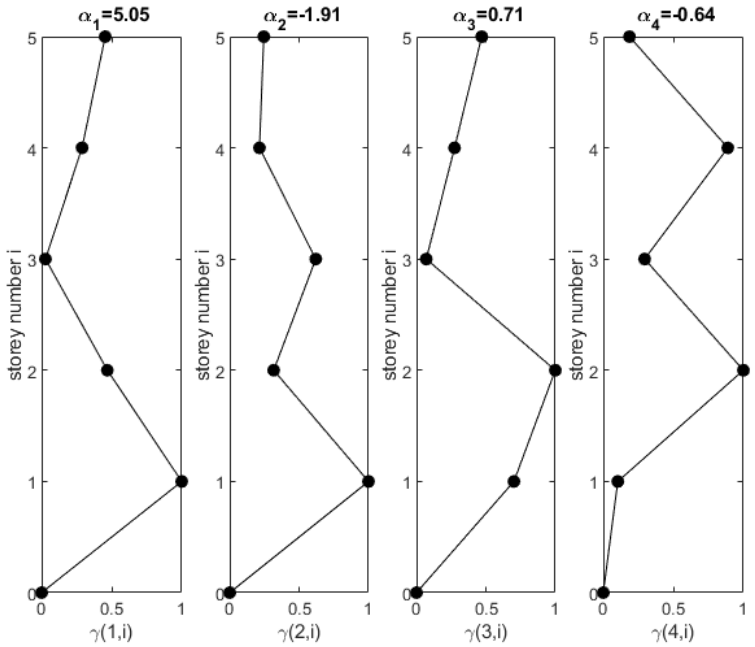

Figure 3.3: 5 storey structure: evolution of γ function in function of N_m modes considered.

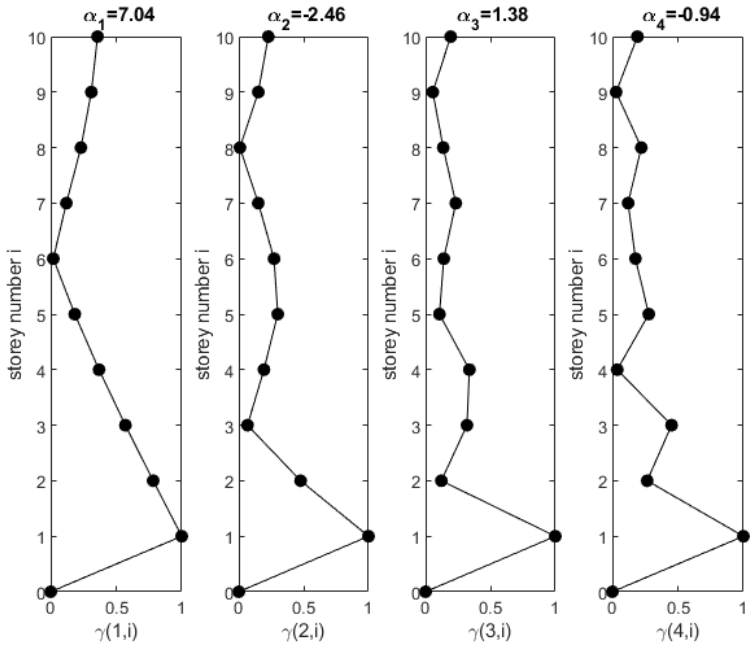

Figure 3.4: 10 storey structure: evolution of γ function in function of N_m modes considered.

Additionally, some particular modes are defined as dominant modes, being the modes in which the N_m points of minimum coincide with the lowest values of the γ function. For the three structures of 5,10 and 20 storeys, the dominant modes result

to be respectively the first two, the first three and the first five.

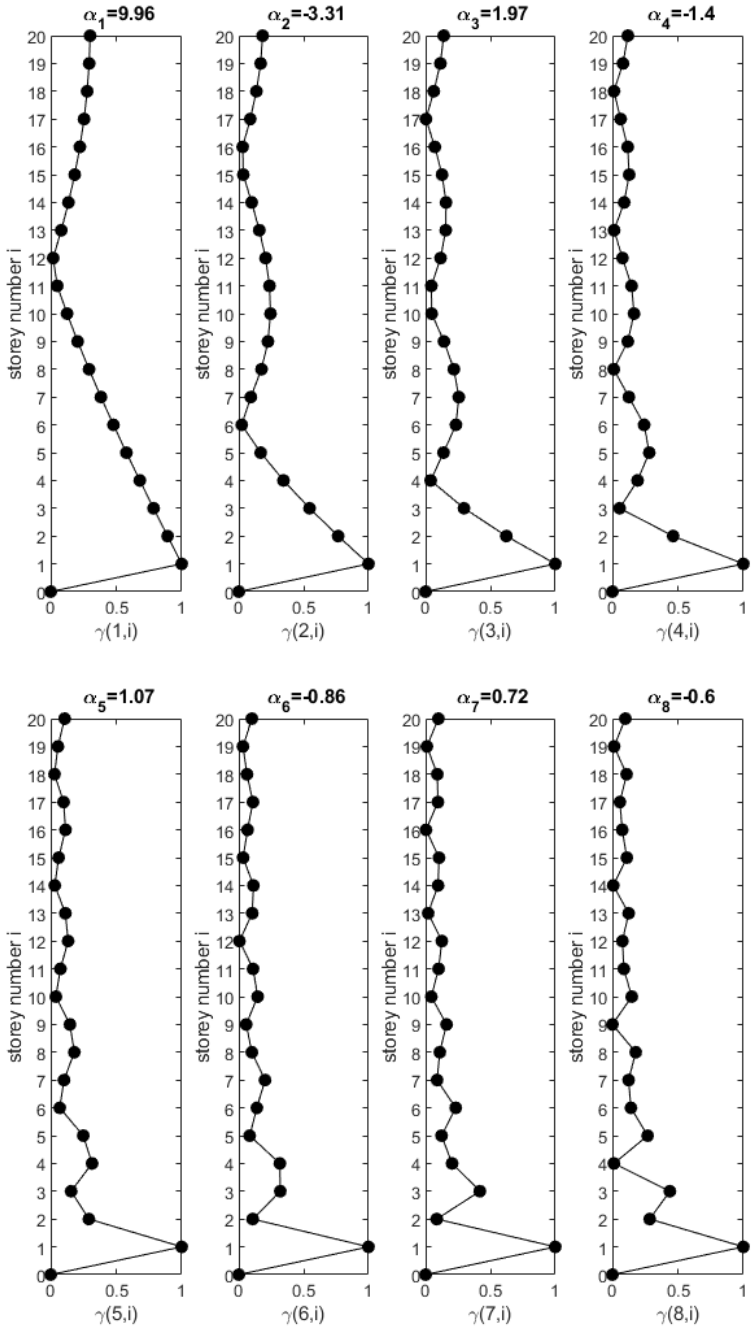

Figure 3.5: 20 storey structure: evolution of γ function in function of N_m modes considered.

3.1.2 Computation of the error associated to spline function interpolation

The results obtained with the just presented methodology were then compared with the results from a time-history analysis where all the possible combinations, for a given number of sensors N_s, were computed and assumed as benchmarks.
The ground motion associated to the El Centro earthquake recorded in 1940 at the Imperial Valley, California, was applied as input motion at the base of the numerical models.
Then, for each possible configuration of sensors through the structure, the absolute accelerations at the relevant floors were used as nodes in a cubic spline interpolation to compute the accelerations at the non-instrumented floors. These computed accelerations were then compared with the actual measured ones.
To define how well the spline using the selected nodes was reconstructing the real motion at the floor i, an error function has been defined at the i-th storey as follows:

$$\varepsilon_i = \sqrt{\frac{\sum_{j=1}^{N_T} \left(a_{r,i}(t_j) - a_{c,i}(t_j)\right)^2}{\sum_{j=1}^{N_T} a_{r,i}^2(t_j)}} \tag{3.6}$$

where $a_{r,i}(t_j)$ is the real acceleration at the i-th storey and at the j-th time instant computed with the time-history analysis, $a_{c,i}(t_j)$ is the computed acceleration with the cubic spline interpolation at the i-th floor and at the j-th time instant and N_t is the total number of time instants of the analysis. To have a general error of the given configuration of sensors, a global mean error was defined as follows:

$$\varepsilon_M = \frac{\sum_{j=1}^{N_f} \varepsilon_i}{N_f} \tag{3.7}$$

where N_f is the number of floors of the structure. This procedure is computationally very heavy as it considers a number of combinations which is equal to :

$$\sum_{n=1}^{k} \binom{k}{n} = \sum_{n=1}^{k} \frac{k!}{n!(k-n)!} = 2^k - 1 \tag{3.8}$$

where k is the number of floors of the structure, resulting in 31, 1023 and 1048575 combinations for 5,10 and 20 floors respectively. For each of the three numerical models and for each number of given sensors the best solution, i.e. the one with the lower mean error for a given N_s number of sensors, was eventually extracted.
In Table 3.3 and 3.4 are respectively presented the results of the method of the first paragraph with their respective error and the ones where the combinations with the minimum error were selected for each N_s number of sensors.

Frame	N_s	$\boldsymbol{z_\beta}$	$\varepsilon_M(\boldsymbol{z_\beta})$ (%)
Five storey	1	0-3	12
	2	0-2-4	5
Ten storey	1	0-6	31
	2	0-3-8	11
	3	0-2-5-9	4
Twenty storey	1	0-13	55
	2	0-6-16	29
	3	0-4-11-17	13
	4	0-3-8-13-18	7

Table 3.3: Optimal location of sensors corresponding to the minimum of γ function with the respective error [28].

Frame	N_s	$\boldsymbol{z}$	$\varepsilon_M(\boldsymbol{z})$ (%)
Five storey	1	3	12
	2	1-4	4
Ten storey	1	7	31
	2	3-8	11
	3	2-5-9	4
Twenty storey	1	13	55
	2	7-16	27
	3	4-10-17	12
	4	3-7-13-19	6

Table 3.4: Optimal location of N_s recording sensors for spline shape function method application [28].

3.2 Proposed 3D method

In this second part of the chapter, 3D models of the frames are considered, resulting in 3D structures with two bays in the X and Y directions. These models are a more realistic representation of structures with respect to a 2D frame. The masses in the structures were modelled as lumped masses generalizing the 2D model and expanding it out of plan as seen in Figure 3.6. For simplicity, the roof's mass was considered to be the same as that of the other floors.
The same sections of beams and columns were considered, as well as the material used. At each floor, all the elements were linked to work rigidly with a rigid diaphragm constraint.
In addition, in order to have different modal parameters in the two X and Y directions, it was considered a frame with different span length in the two directions. In particular, it was considered to have a span of 4 m along the X direction and of 6 m along the Y direction.
In space each storey would have 3 translational and 3 rotational DoFs, resulting in a total of $6 \cdot N_f$ DoFs, where N_f is the number of floors. Nevertheless, in this thesis it was decided to reduce the DoFs of each floor to 3 (two translational along X and Y-axis and one rotational around Z-axis) as often done in the literature [10]. The result is a generalization in 3D of a shear building with columns that have infinite axial stiffness. Practically, this reduction of DoF was applied in the numerical model by restraining all the nodes along the Z-axis.

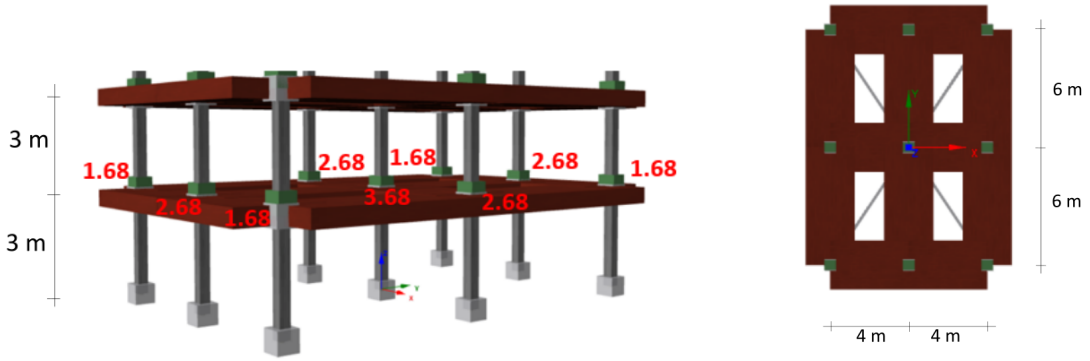

(a) Perspective view (b) Top view

Figure 3.6: Geometry and distribution of masses.

For the sake of brevity, In the following elaborations just the 10 floors structure has been considered, as it is an intermediate model between the 5-storey one which is extremely simple and the 20-storey one which has a higher number of dominant modes and thus is more meaningful. Additionally, in Chapter 4, a structure with 9 floors is examined, allowing for a direct comparison with the 10-storey structure discussed in this chapter.

Nevertheless, all the steps were also applied to the 5 and 20-storey models, and their corresponding conclusions are presented at the end of the chapter.

3.2.1 Symmetric mass distribution

At first, the simplest case of a symmetric mass distribution in plan as the one in Figure 3.6 was considered. As in the 2D frame, the masses of the structure were lumped in specific nodes throughout the slab. The resulting centre of mass CM coincides with the geometric centre of the structure.
For each floor, the total mass along the X and Y-axis in this case is m_x=m_y=21.12 tons, while the rotational inertia with respect to the centre of mass CM is I_0=628.16 tons $\cdot$ m^2.
The mass matrix becomes thus a $3N_f$x$3N_f$ matrix created assembling three mass matrices as the one in Equation 3.1 along the three directions:

$$\boldsymbol{m} = \begin{bmatrix} \boldsymbol{m_x} & 0 & 0 \\ 0 & \boldsymbol{m_y} & 0 \\ 0 & 0 & \boldsymbol{I_0} \end{bmatrix} = \begin{bmatrix} m_{x,1} & 0 & \cdots & 0 & 0 \\ 0 & m_{x,2} & \cdots & 0 & 0 \\ \vdots & \vdots & \ddots & \vdots & \vdots \\ 0 & 0 & \cdots & I_{0,N_f-1} & 0 \\ 0 & 0 & \cdots & 0 & I_{0,N_f} \end{bmatrix} \tag{3.9}$$

Compared to the 2D frame, the structure presents also some torsional modes.
For the 10 floors structure, the first 20 modes are the one presented in Table 3.5, where the value of the highest participation factor is bolded, showing which DoF is dominating the mode.

Mode	Period [s]	α_x	α_y	α_{rz}
1	0.772	0.000	**13.364**	0.001
2	0.764	**13.370**	-0.000	0.007
3	0.686	0.001	0.000	**-72.981**
4	0.259	0.000	**-4.401**	0.000
5	0.256	**4.399**	0.000	0.000
6	0.230	0.000	0.000	**23.963**
7	0.157	0.000	**-2.574**	0.000
8	0.156	**2.568**	0.000	0.000
9	0.140	0.000	0.000	**13.936**
10	0.114	0.000	**-1.764**	0.000
11	0.113	**1.755**	0.000	0.000
12	0.103	0.000	0.000	**9.474**
13	0.091	0.000	**1.289**	0.000
14	0.091	**-1.279**	0.000	0.000
15	0.082	0.000	0.000	**-6.860**
16	0.077	0.000	**-0.964**	0.000
17	0.077	**0.953**	0.000	0.000
18	0.068	0.000	**-0.716**	0.000
19	0.068	**0.705**	0.000	0.000
20	0.062	0.000	**0.510**	0.000

Table 3.5: First 20 modes and corresponding component of the participation factor.

For the three DoF, the two main modes according to the α factor are presented

below.

α_x=13.370

α_y=13.364

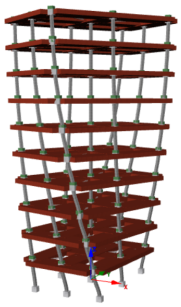

α_{rz}=-72.981

α_x=4.399

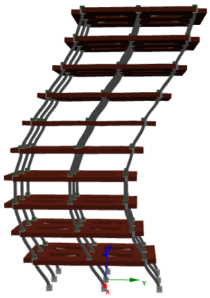

α_y=-4.401

α_{rz}=23.963

Figure 3.7: First two modes for each direction with respective α factor.

For the expansion of the method to take into account also of the torsional modes the definition of the effective participation factor β in the 2D method was replicated in the three directions with three separated effective participation factors:

$$\boldsymbol{\beta_x^{(r)}} = \alpha_x^{(r)} \cdot \boldsymbol{\Phi_n^{(r)}} \tag{3.10}$$

$$\boldsymbol{\beta_y^{(r)}} = \alpha_y^{(r)} \cdot \boldsymbol{\Phi_n^{(r)}} \tag{3.11}$$

$$\boldsymbol{\beta_{rz}^{(r)}} = \alpha_{rz}^{(r)} \cdot \boldsymbol{\Phi_n^{(r)}} \tag{3.12}$$

where

$\alpha_x^{(r)}$, $\alpha_y^{(r)}$, $\alpha_{rz}^{(r)}$ are the components of the participation factor relevant to the input in the X,Y and RZ directions for the r-th mode

$\boldsymbol{\Phi_n^{(r)}}$ is the modal shape normalized with respect to the mass matrix for the r-th mode, with a size [$3N_f$x1]

In this case, accordingly with the statements from the previous section, defining

$$\boldsymbol{s_x}(N_m) = \sum_{r=1}^{N_m} \boldsymbol{\beta_x^r} \qquad\qquad \boldsymbol{\gamma_x}(N_m) = 1 - \boldsymbol{s_x}(N_m) \tag{3.13}$$

$$\boldsymbol{s_y}(N_m) = \sum_{r=1}^{N_m} \boldsymbol{\beta_y^r} \qquad \boldsymbol{\gamma_y}(N_m) = 1 - \boldsymbol{s_y}(N_m) \tag{3.14}$$

$$\boldsymbol{s_{rz}}(N_m) = \sum_{r=1}^{N_m} \boldsymbol{\beta_{rz}^r} \qquad \boldsymbol{\gamma_{rz}}(N_m) = 1 - \boldsymbol{s_{rz}}(N_m) \tag{3.15}$$

in the case in which N_m corresponds to the total number of modes, the components of s_x, s_y and s_{rz} respectively in the X,Y and RZ direction converge to 1.
It is noted that in a 3D model, a lower mode with a higher period does not always have a higher $|\alpha|$ factor, and thus higher effective modal mass. Consequently, the γ functions are computed and plotted as in the 2D procedure.
Their evolution with respect to N_m is presented in Figure 3.8.

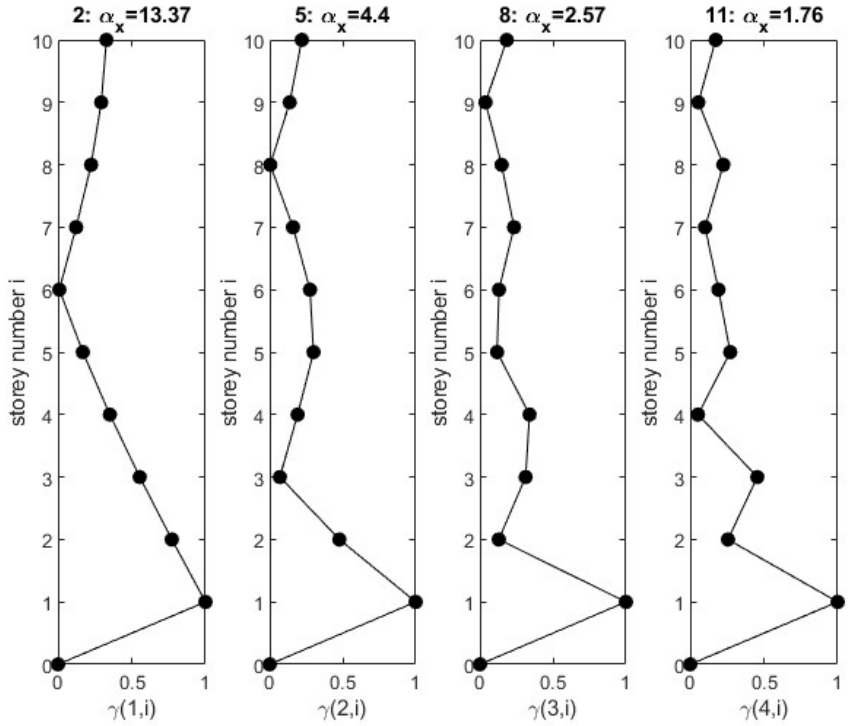

Figure 3.8: Evolution of γ along X in function of N_m modes considered.

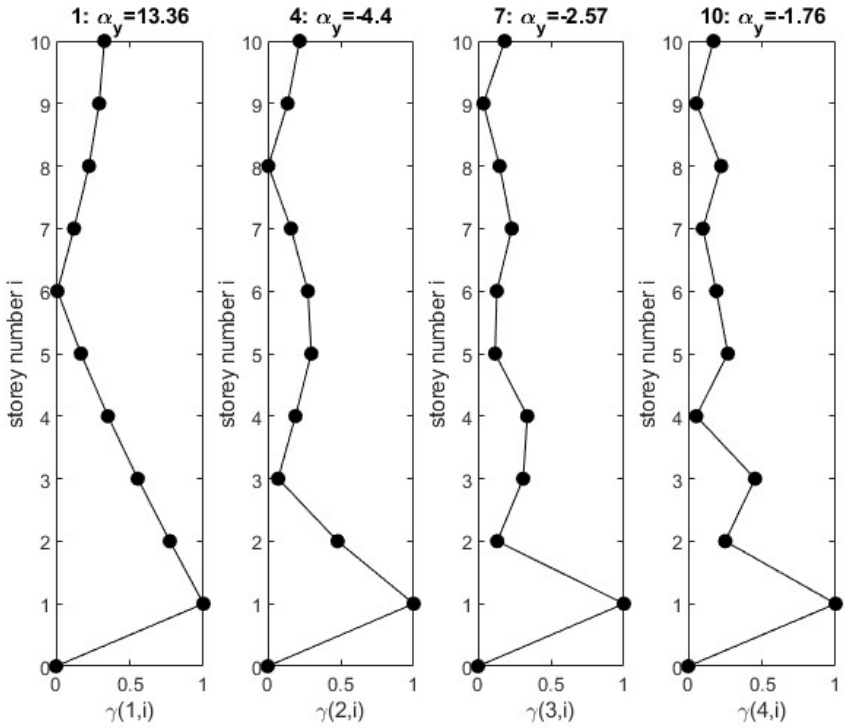

Figure 3.9: Evolution of γ along Y in function of N_m modes considered.

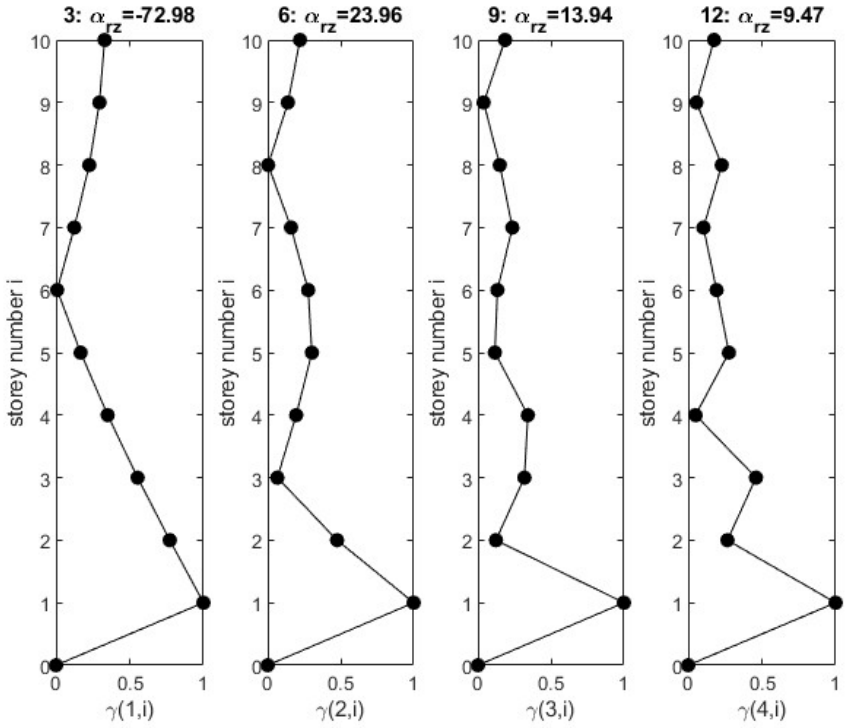

Figure 3.10: Evolution of γ around Z in function of N_m modes considered.

As it can be seen from Figures 3.8, 3.9 and 3.10, in this initial case where the

mass distribution is symmetric in plan the behaviour of the γ function for the three directions is similar to the one of the 2D frame. In other words, the minimums of the γ function for the dominant modes (the first three for this case of 10-storey structure) are located at the same floors as in the case where just flexural modes in one direction are considered.
This conclusion is coherent with what was expected, as a structure with centre of mass corresponding with the centre of stiffness does not display high torsional behaviour, thus just the flexural modes can be used for describing the dynamic behaviour of the structure. In order to remark a torsional response of the structure, it is necessary to have the presence of some eccentricities, as presented in Section 3.2.2.

3.2.2 Non-symmetric mass distribution

In this second section all the masses were removed apart from the ones on the East side, leaving unchanged the rest of the numerical model. In such a way, the centre of mass would shift from the geometric centre of the previous situation to an eccentric node, highlighted in Figure 3.11.

With respect to the structure considered in Section 3.2.1, the torsional response in this case would be really important with a ground motion along the Y-axis as the eccentricity of the centre of mass with respect to the geometric centre e_x=4 m, while on the X-axis the behaviour would remain unchanged, as e_y=0 m.
Because of the reduced number of masses considered, the parameters inside the mass matrix had to be changed. For each floor, the total mass along the X and Y-axis in this case is m_x=m_y=6.04 tons, while the rotational inertia with respect to the centre of mass CM is I_0=120.96 tons $\cdot$ m^2.

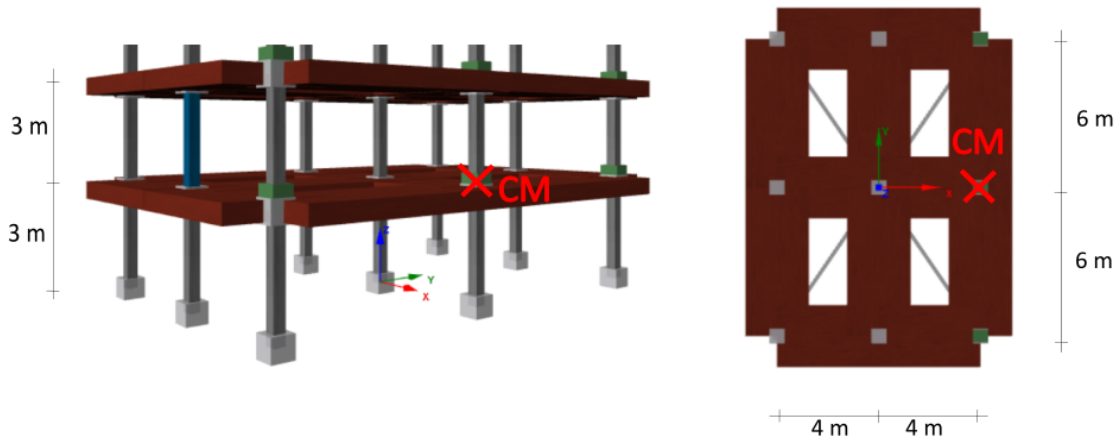

Figure 3.11: Geometry and position of the centre of mass CM.

Due to the eccentricity of the centre of mass, each mode is no longer purely in one degree of freedom. Indeed, the eigenvalue analysis presents a set of modes that

are either purely flexural along the X-axis or flexural-torsional along the Y-axis and around the Z-axis. In Table 3.6, the whole set of modes for the 10-stories model is presented, where the DoF along which the mode mainly develops is underlined in bold.

It is noted that there are 10 flexural modes along the X-axis and 20 flexural-torsional modes along the Y-axis and around the Z-axis. These latter modes can be divided in 10 couples, characterised by a similar modal shape: for instance modes 3 and 1 have the classic modal shape of the first mode (displacements and rotations with the same sign for all floors), see Figure 3.12.
In Table 3.7 all the couples of modes behaving with a similar modal shape are shown.

Mode	Period [s]	α_x	α_y	α_{rz}
1	0.527	0.000	**6.562**	**12.722**
2	0.408	**-7.150**	0.000	0.000
3	0.236	0.000	**2.824**	**-29.403**
4	0.177	0.000	**-2.173**	**-4.029**
5	0.137	**2.352**	0.000	0.000
6	0.108	0.000	**-1.257**	**-2.454**
7	0.083	**1.373**	0.000	0.000
8	0.079	0.000	**-0.785**	**9.790**
9	0.078	0.000	**-1.002**	**-0.051**
10	0.063	0.000	**-0.627**	**-1.191**
11	0.061	**-0.939**	0.000	0.000
12	0.053	0.000	**-0.460**	**-0.955**
13	0.049	**0.684**	0.000	0.000
14	0.048	0.000	**-0.545**	**5.626**
15	0.047	0.000	**-0.367**	**-0.428**
16	0.043	0.000	**0.246**	**0.451**
17	0.041	**-0.510**	0.000	0.000
18	0.041	0.000	**-0.157**	**-0.305**
19	0.039	0.000	**0.076**	**0.153**
20	0.036	**-0.377**	0.000	0.000
21	0.035	0.000	**-0.385**	**3.820**
22	0.033	**-0.268**	0.000	0.000
23	0.031	**0.173**	0.000	0.000
24	0.030	**-0.085**	0.000	0.000
25	0.028	0.000	**0.280**	**-2.778**
26	0.024	0.000	**0.210**	**-2.064**
27	0.021	0.000	**0.156**	**-1.523**
28	0.019	0.000	**-0.111**	**1.080**
29	0.018	0.000	**0.072**	**-0.694**
30	0.018	0.000	**-0.035**	**0.340**

Table 3.6: Modes and corresponding component of the participation factor.

α_x=-7.150

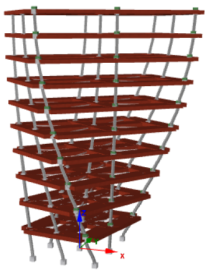

α_y=-2.036
α_{rz}=-29.403

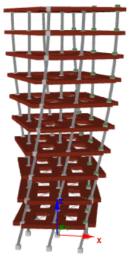

α_y=6.562
α_{rz}=12.722

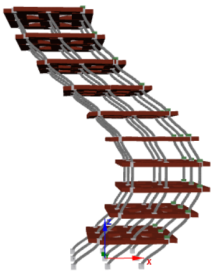

α_x=2.352

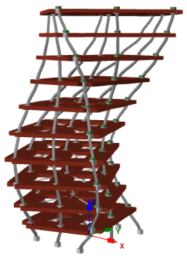

α_y=-0.785
α_{rz}=9.790

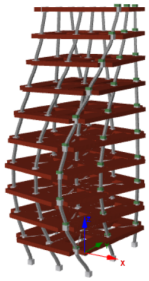

α_y=-2.173
α_{rz}=-4.029

Figure 3.12: First two modes for the X direction (left) and first four modes for the Y and RZ direction, sorted by the $|\alpha_{rz}|$ factor (centre and right).

Modal shape	1st mode	2nd mode	3rd mode	4th mode	5th mode
Mode	1-3	4-8	6-14	9-21	10-25

Table 3.7: Pairs of modes grouped by their modal shape.

In this case, it becomes clear that the lower modes are not necessarily the ones with the highest value of $|\alpha|$, particularly for those along RZ.

For this reason, before computing the sum functions, the modes were ordered with respect to their corresponding $|\alpha|$ factor. As previously done for the structure with symmetrically distributed masses, the definition of the effective participation factor was applied and the corresponding results discussed.

Applying Equations 3.10 to 3.12, and subsequently Equations 3.13 to 3.15 to the current scenario, the γ functions were plotted with respect to the number of modes N_m considered.

While along the X-axis the evolution of γ is unchanged, for the two other DoF some differences are found. It is remarked that since the Y and RZ DoF are coupled,

the order in which the sum function was implemented for both DoF was based on the following criteria:

- The modes were grouped according to the couples in Table 3.7
- Among the two modes of each couple, the one with a higher $|\alpha_{rz}|$ was placed before

This was not the case when all the modes were decoupled: in that situation, the modes along each DoF were ordered just in function of the α factors respective to that DoF.

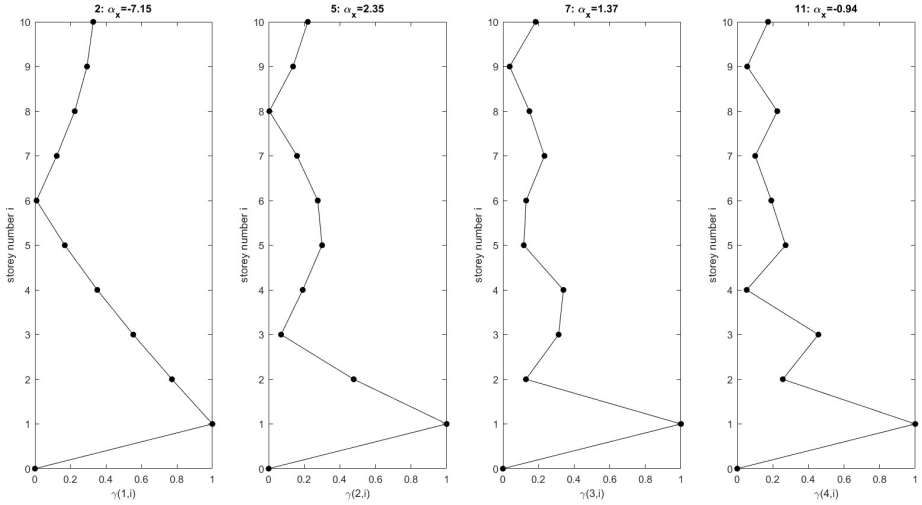

Figure 3.13: Evolution of γ along X in function of N_m modes considered.

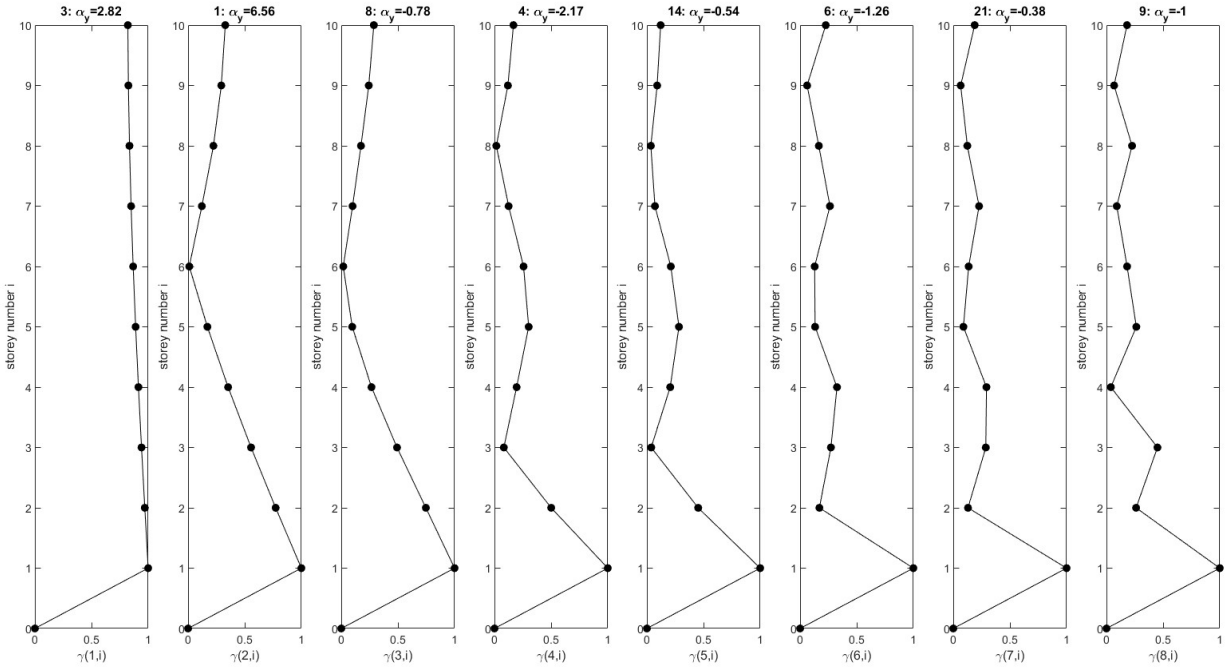

Figure 3.14: Evolution of γ along Y in function of N_m modes considered.

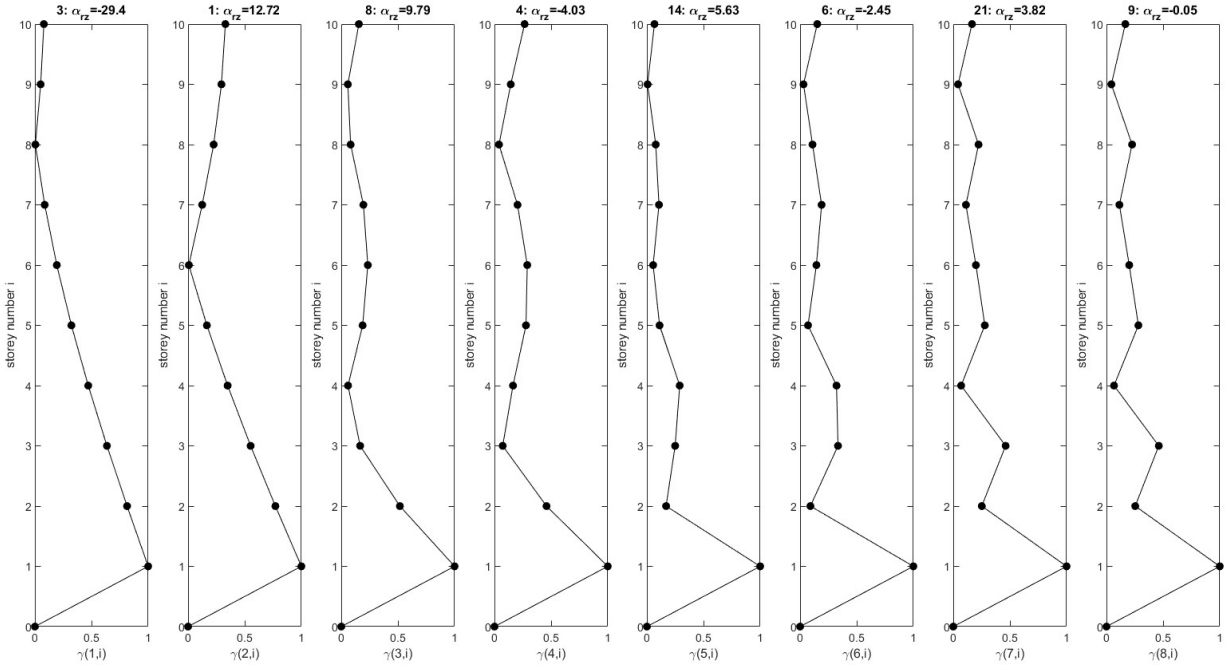

Figure 3.15: Evolution of γ around Z in function of N_m modes considered.

In contrast to Section 3.2.1, the behavior of the γ functions is less straightforward to interpret. It is found that N_{min} does not always equal N_s, where N_{min} represents

the number of local minima of the γ function and N_s denotes the number of modes considered. This is because in this 3D model there are more modes having a similar modal shape (see Table 3.7). Thus, to draw consistent conclusions on the optimal positioning of sensors in this situation, the cumulative behaviour of the couple of modes with similar modal shape has to be analysed. As a result, the first couple (modes 3 and 1) displays a local minimum at the third floor for both Y and RZ directions. The second couple (modes 8 and 4) displays two local minimums at the second and fourth floors for both Y and RZ directions.

The results are summarized in Table 3.8, where with a given number of sensors the optimal placement is specified in the three directions :

N_s	Direction		
	X	Y	RZ
1	6	6	6
2	3-8	3-8	3-8
3	2-5-9	2-5-9	2-5-9

Table 3.8: Optimal placement of sensors for a 10-storey structure.

3.3 Conclusions

According to the results from Section 3.2, for both 3D structures analysed the outputs of the γ functions are the same as the ones of the 2D structure from Section 3.1, found in Table 3.3.

For a model with Centre of Mass coincident with the Centre of Stiffness of the structure the modes are all almost purely along one DoF, and the procedure to compute the optimal positioning of sensors results to be straightforward as in the 2D case. Conversely, when the CM is eccentric with respect to the CS some modes can become coupled along different DoFs. To obtain the ideal position, it is thus necessary to select the modes with the same modal shape and consider the contribution of both of them. The points of local minimum in the 3D case, just discussed, coincide with the ones of the 2D case, leading to conclude that the optimal positioning in the two situations coincides.

The procedure was also applied to the 5-storey and 20-storey numerical models, with similar conclusions. In Appendix B the steps of the analysis are presented also for these other two frames, with the corresponding behaviour of γ functions.
It is then possible to state that regardless the high or low torsional response of a structure, since the behaviour of the torsional modes is analogous to the one of the flexural modes, to identify the optimal position of sensors it is sufficient to just consider the flexural behaviour of the structure, and thus to simplify it considering just the flexural modes in one direction, as done in the 2D frame.

Chapter 4

Numerical modelling-Australian Structure

In the intent to apply the principles seen in the previous chapter in the specific context of this thesis, a numerical model of a classic Australian Structure was created. The software used for this process of numerical modelling was, as in the previous chapter, Seismostruct.
The initial part of this chapter is dedicated to some numerical considerations related to modelling the considered structure, the second part is devoted to assess and measure the global characteristics of the structure given by different analyses (e.g. pushover curve, occurrence of cracking and yielding respectively of concrete and steel) while the third part concerns mainly the application of the method of the previous chapter to the structure.

Dr. Scott Menegon, a lecturer at Swinburne University of Melbourne and the main coordinator of the AEES's program for S^2HM in Darwin, provided significant support for this thesis. Dr. Menegon supplied detailed plans of traditional Australian structures, located in Melbourne, which were used for the research and analysis conducted in this study.

In Appendix C, all the provided plans for three different structures can be found. They are all flat slabs reinforced concrete structures, of respectively 8, 10 and 6 floors (plus the roof). In this thesis, just the plans related to the first structure have been used to create a numerical model. The choice of this specific structure was made based on the fact that its height is intermediate if compared to the other two, and also because it is characterized by a simpler geometry of the concrete cores.

4.1 Description of the structure and modelling

The considered structure is a flat slab reinforced concrete multi-storey office building with a rectangular plan measuring 58.8 m by 28 m. The building has 7-storey with a total height of 36.8 m. The interstory height is the same for all the floors and equal to 4 m, except the first floor, placed at 4.8 m from the street level.
The gravity loads are sustained by vertical elements, i.e. columns and concrete

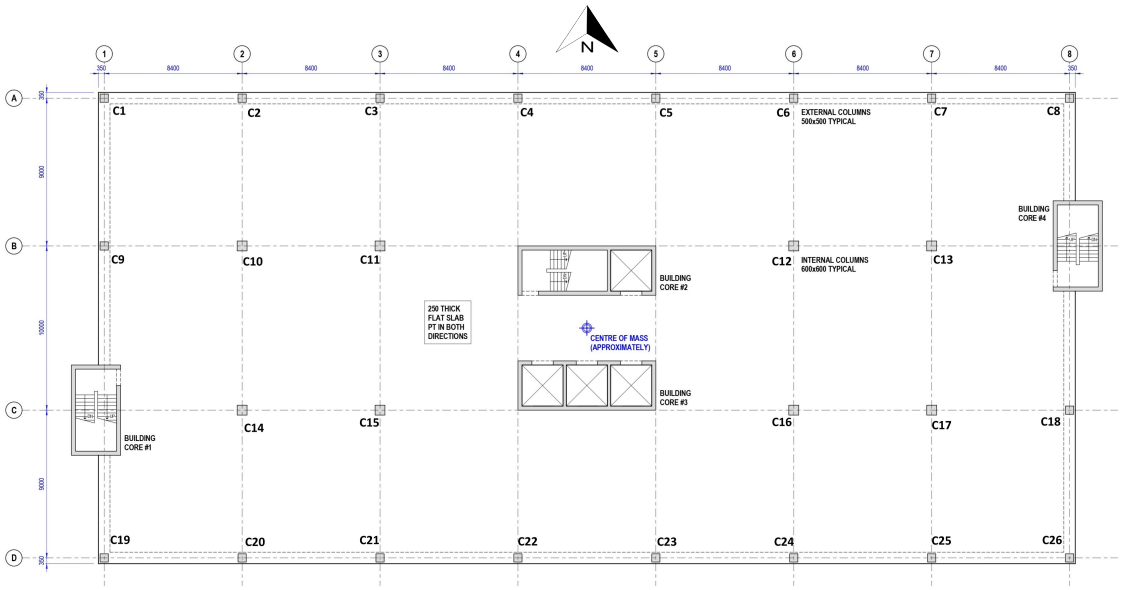

Figure 4.1: Typical floor framing plan for levels 1 to 8, adapted from the given plan.

cores, linked between them with a 250 mm thick slab. A perimeter beam goes all around the structure, linking the external columns.
Four concrete cores, symmetrically positioned in the plan, house the stairs and elevators and provide an adequate capacity to sustain lateral loads.

In the given plan, a set of design notes related to the structure and its loadings were provided. The whole list of these notes can be found in Appendix C. In the following, the most important are presented:

1. The case study building was designed to comply with the 2016 National Construction Code (NCC), Volume 1: The Building Code of Australia (BCA), Class 2 to Class 9 buildings.

2. Design criteria in accordance with the 2016 NCC, with a building importance level of 2 and a design return period for earthquake action of 500 years

3. The case study building is an office building and has been designed for the following loads:

   - 4 kPa imposed on general levels (L1 to L7)
   - 1.5 kPa imposed on the roof level (L8)
   - 1.2 kPa superimposed dead load on general levels (L1 to L7)
   - 1.5 kPa superimposed dead load on the roof level (L8)
   - 0.25 kPa facade load

4. Wind actions for the building have been determined in accordance with AS/NZS 1170.2:2011, but for the current study they were neglected

5. Earthquake actions for the building have been determined in accordance with AS 1170.4:2007 based on the following parameters:

Parameter	Value
EDC	2
Probability factor	1.0
Peak ground acceleration hazard	0.08 g
Site sub-soil class	C
Building ductility factor	2.0
Structural performance factor	0.77

Table 4.1: Parameters used in the design.

6. All concrete elements (i.e., floors, walls and columns) are designed for a fire resistance level of 120 minutes.

Since the purpose of this numerical model was to validate the method presented in the previous chapter, which is applied in the frame of S^{2}HM, the combination of loads considered was the one at the ULS related to earthquake actions.
According to both Australian Standards AS-NZS 1170.0 (section 4.2)[38] and Eurocode 0 (section 6.4.3.4)[17] they are defined as follows:

$$E_d = E\left\{G_{k,j}; P; A_{Ed}; \psi_{2,i}Q_{k,j}\right\} \quad j \geq 1; i \geq 1 \tag{4.1}$$

Which can be expressed also as:

$$\sum_{j\geq 1} G_{k,j} + P + A_{Ed} + \sum_{i\geq 1} \psi_{2,i}Q_{k,i} \tag{4.2}$$

where $G_{k,j}$, P, A_{Ed} and $Q_{k,i}$ are respectively the permanent, prestressed, accidental, i.e. earthquake, and variable loads and where $\psi_{2,i}$ is a reduction factor equal to 0.3 for office buildings, as seen in Figure 4.2. It has to be remarked that in the current combination the wind loads were neglected.

Action	ψ_0	ψ_1	ψ_2
Imposed loads in buildings, category (see EN 1991-1-1)			
Category A : domestic, residential areas	0,7	0,5	0,3
Category B : office areas	0,7	0,5	0,3
Category C : congregation areas	0,7	0,7	0,6
Category D : shopping areas	0,7	0,7	0,6
Category E : storage areas	1,0	0,9	0,8
Category F : traffic area, vehicle weight ≤ 30kN	0,7	0,7	0,6
Category G : traffic area, 30kN < vehicle weight ≤ 160kN	0,7	0,5	0,3
Category H : roofs	0	0	0
Snow loads on buildings (see EN 1991-1-3)*			
Finland, Iceland, Norway, Sweden	0,70	0,50	0,20
Remainder of CEN Member States, for sites located at altitude H > 1000 m a.s.l.	0,70	0,50	0,20
Remainder of CEN Member States, for sites located at altitude H ≤ 1000 m a.s.l.	0,50	0,20	0
Wind loads on buildings (see EN 1991-1-4)	0,6	0,2	0
Temperature (non-fire) in buildings (see EN 1991-1-5)	0,6	0,5	0
NOTE The ψ values may be set by the National annex. * For countries not mentioned below, see relevant local conditions.			

Figure 4.2: Table A1.1 in Eurocode 0 with the ψ factors for different structures, in the red rectangle the one for office areas, used in this thesis [17].

In the following sections, all the reasoning behind the modelling of each structural member is presented, with a special attention to the procedure implemented for

modelling the concrete cores. Indeed, it is crucial to pay significant attention to accurately modelling a structure, as an incorrect model can result in outcomes that significantly deviate from the real behaviour, leading to incorrect conclusions.

4.1.1 Concrete cores: Wide Column Method

For an accurate modelling of the structure, sufficient attention had to be taken on modelling the concrete cores. This chapter is dedicated to the description of the method that was used to model these parts, the so-called Wide Column Method.
In the following lines, a brief description of the most common approaches used for reinforced concrete cores modelling is presented, to justify the choice of such method among the others [3]:

- **the Simple Stick Method (SSM)**: in this model, the concrete core is considered as a one-dimensional vertical cantilever with a defined section corresponding to the one of the core. This type of analysis is extremely simple but does not take into account of tridimensional effects. For this reason, it is a method that is not suitable for modelling non-planar walls

- **the Wide Column Method (WCM)**: in this case, each side of the core is modelled as an independent element and then linked with rigid links. Unlike the previous method, it allows taking into account of tridimensional effects, keeping the model simple.

- **the Shell Element Method (SEM)**: In this analysis, the concrete cores are represented by multiple superimposed shell elements with a small thickness. While this approach is the most accurate as it allows capturing the stress variation in the concrete over the thickness of the wall, it is computationally intensive and is not practical for routine numerical analysis in everyday design [3].

Among the three, the WCM was chosen as a good compromise between accuracy and computational cost. This method also proved to be well-suited for modelling concrete cores.

The guidelines given by Beyer et al. [3] in their research on Inelastic Modelling of U-shaped walls with the Wide Column Method were used to model the concrete cores of the Australian Buildings considered in this paper.
In particular, the main guidelines used for the numerical model are:

- the reinforcement in the corners between each side of the concrete core has been divided in such a way that the total amount of reinforcement is unchanged (Figure 4.3).

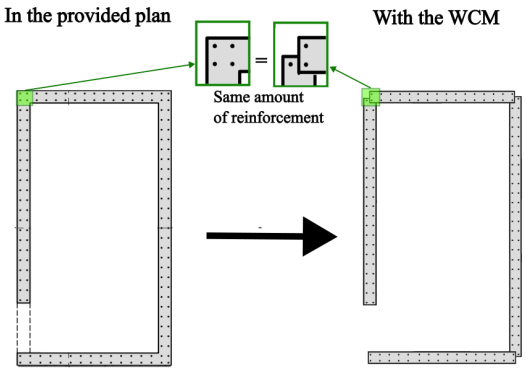

Figure 4.3: Equal distribution between the two wall elements of the reinforcement in each core's corner, example with core #4.

- the spacing in between the horizontal links h_{sp} connecting the single walls is set as the minimum between one fifth of the shear span and half of the larger wall length. In order to have the same nodes' height for all the four cores, the spacing between rigid links was defined in function of the minimum larger wall length among the cores:

$$h_{sp} = min\left(\frac{0.7h}{5}; \frac{min(l_w)}{2}\right) \tag{4.3}$$

  where $0.7h$ is the shear span, in function of the total height h. As shown in Table 4.2, the maximum h_{sp} is 2.75 m. To ensure that the nodes align with the height of the floors, it was decided to use a value of h_{sp} such that the interstory height would be a multiple of it.
  Two h_{sp} had thus to be considered, as in the structure considered in this chapter the first interstory height differs from the one of the other floors.

Parameter	**Value [m]**
total height	36.80
shear span	25.76
min(l_w)	5.50
maximum h_{sp}	2.75
h_{sp}^{1} chosen	2.40
h_{sp}^{2-roof} chosen	2.00

Table 4.2: Values to define h_{sp}

- the horizontal rigid links are assigned a torsional flexibility to allow warping. According to Raynouard and Fardis [34] the rotational stiffness is set as:

$$GK = 0.25G\frac{h_{sp}t_w^3}{3} \tag{4.4}$$

where t_w is the wall's thickness (considered everywhere 250 mm) and G is the shear modulus of concrete, defined as $G = \frac{E}{2(1+\nu)}$ with E that is the Young modulus and ν is the Poisson's ratio. This parameter was selected to be within the typical range of 0.1 to 0.2, representing a common interval for concrete. The chosen value was set at an intermediate point within this range (0.15) [15]. Since in the structure different types of concrete have been used, different values of GK have been computed:

Australian class	N50		N40
Equivalent European class	C50/60		C40/50
E [MPa]	37278		35220
G [MPa]	16208		15313
h_{sp} [m]	2.4	2	2
GK $\cdot 10^{10}$[KN/mm^2]	5.07	4.22	3.99

Table 4.3: Different values of GK used in the numerical model [16].

- for the vertical elements, for inelastic structures, each member should be divided in sub-elements with a height of $\frac{h_{sp}}{2}$, which means that intermediary nodes have to be placed between horizontal links. Although the method described in Chapter 3 was developed for materials with elastic behaviour, this recommendation was implemented in the case study to obtain a more accurate pushover curve.

- Fibre sections were assigned to the vertical elements. In this way the interaction of axial and flexural capacities, as well as the axial elongation at the centre of the sections, were well captured.

4.1.1.1 Reproduction of existing models in the literature

In order to model properly following the above indications, some existing models of concrete cores developed with the WCM were analysed and reproduced.
In particular, it was decided to reproduce the numerical models created during the research that was carried out in the above-mentioned paper by Beyer et al. [3]. Their research aimed to understand how to properly apply the WCM to accurately model the behaviour of some U-shaped cores. To understand the precision of the method, they carried out a sensitivity analysis over the different numerical variables of the cores, using an experimental test as a benchmark. This experimental campaign was done in ETH of Zurich's laboratories, where two U-shaped cores named TUA and TUB, with respective wall thicknesses of 150 mm and 100 mm, were poured and tested (Figure 4.5). The axial load ratio (ALR) for the two walls was respectively 0.02 and 0.04, where the axial load is applied with vertical actuators. Three horizontal actuators were also used in the experiment, placed as displayed in Figure 4.4 in order to successfully apply a quasi-static cyclic load on the core with cycles in different directions.

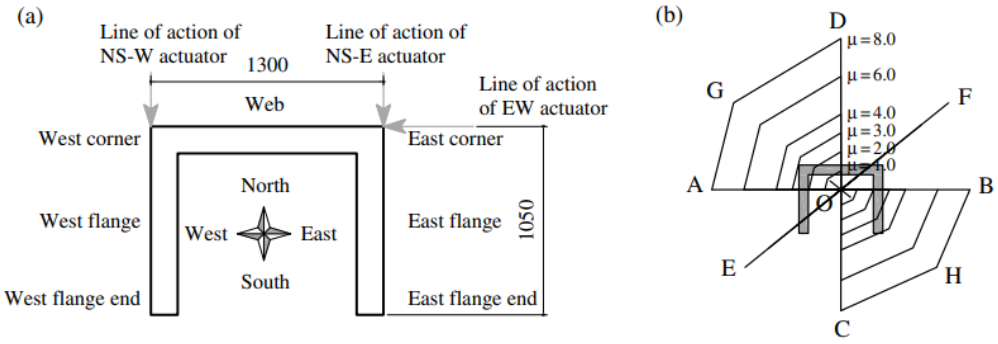

Figure 4.4: Cardinal points and labelling of different wall sections (a) and bidirectional loading history with target displacements (b) [3].

In Figure 4.5 the two cores are presented in plan, with their corresponding experimental setup. In order to properly redistribute the applied quasi-static cyclic loading, a thicker collar was poured at the top of both walls.

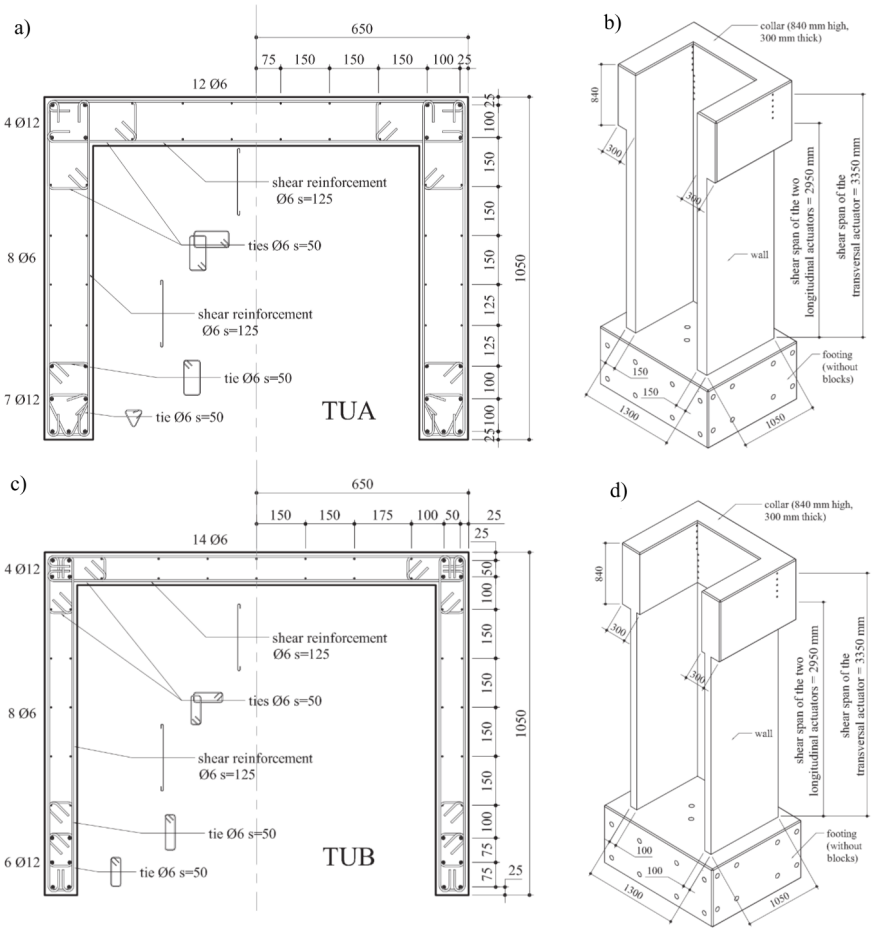

Figure 4.5: Representation in plan (a)-(c), and perspective (b)-(d), of the two concrete cores tested in ETH, adapted from [4].

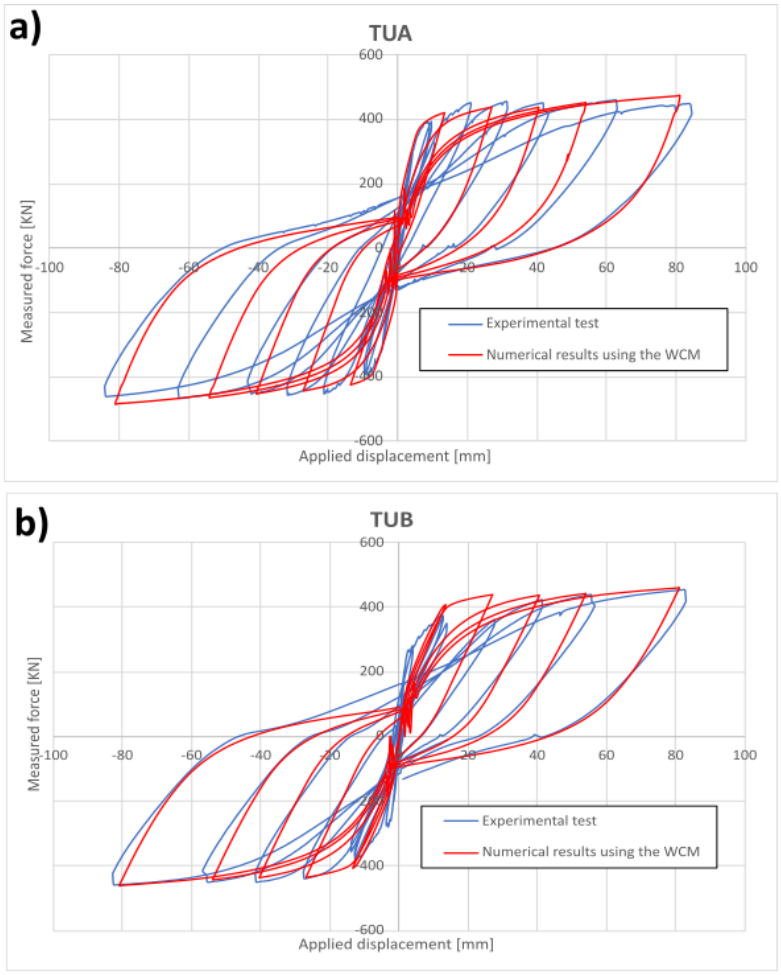

Figure 4.6: Force-displacement curve associated to the quasi-static cyclic load along A-B for TUA (a) and TUB (b).

In the work of the current thesis, the force-displacement diagrams obtained experimentally with cycles along the A-B direction were compared with the one from the numerical model, as it was done in the just mentioned research. In Figure 4.6 the force-displacement diagrams show that the numerical model using the WCM well simulates the measured behaviour of the core in the ETH of Zurich's laboratories. This method therefore seems suitable for modelling non-planar reinforced concrete cores, which is why it was selected in this thesis to model the concrete cores of the structure.

4.1.1.2 Australian Structure

As mentioned before, in the considered Australian Structure's plan there are four concrete cores, arranged symmetrically with respect to the centre of mass (Figure 4.1).
Core #1 and core #4 are respectively placed on the Western and Eastern edge of the building, while core #2 and core #3 are located next to its geometric centre.
Core #4 has the same geometry as core #1, but with a rotation of 180° (Figure

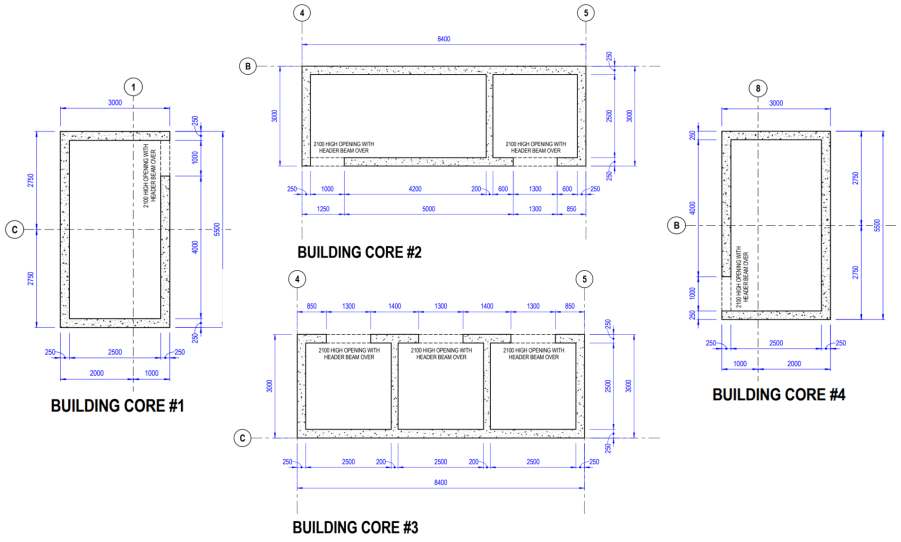

Figure 4.7: four cores

4.7). On the other hand, core #2 and #3 have a different geometry, even if the same main two dimensions.

For what concerns the reinforcement of the cores, 6 different layouts are defined based on the core and on the storey. Intuitively, the higher the floor, the lower amount of reinforcement was used. In Figure 4.8 the spacial disposition over the height of the 6 types is shown, with information also on the concrete cover (30 mm everywhere) and on the type of concrete. The prefix N in front of the steel rebars' diameter stands for "Normal Ductility Class Deformed Reinforcing Bar", and they are made with a steel grade which corresponds to the B500 in Europe. The same principle is applied to the concrete, where the prefix N stands for "Normal Class". It is noted that, the transversal reinforcement is just placed to satisfy shear requirements and comply with SLS provisions on minimum reinforcement, without providing any confinement to the cores. This happens also in some low-to-moderate seismic regions in Europe.
Nevertheless, often in Europe some additional reinforcement is placed in specific regions of the cores, to provide confinement and increase the performance of the element. An example is found in Figure 4.5, where at the end of the U-shaped wall there is some additional transversal reinforcement, indicated as "tie".

To achieve better control over the modelling of the cores and on their behaviour, they were initially created in separate Seismostruct files and a pushover analysis was applied to extract their capacity curve. These files were then combined and linked with rigid diaphragms at each floor to ensure a global response. Due to initial convergence issues in the dynamic time-history analysis, some suggestions from the Seismostruct Verification Report were followed. All the elements were modelled with inelastic force-based frame elements (infrmFB) with the exception of short elements which display better convergence behaviour with displacement-based elements (infrmDB) [36] (Figure 4.9).

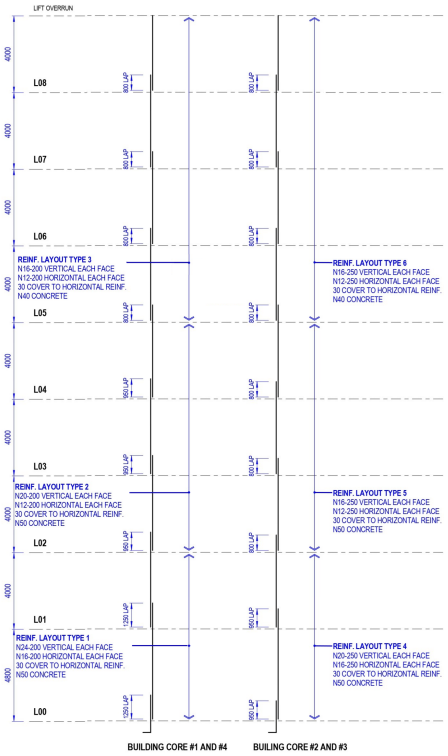

Figure 4.8: Layout of vertical reinforcement for the four cores, adapted from the given plan.

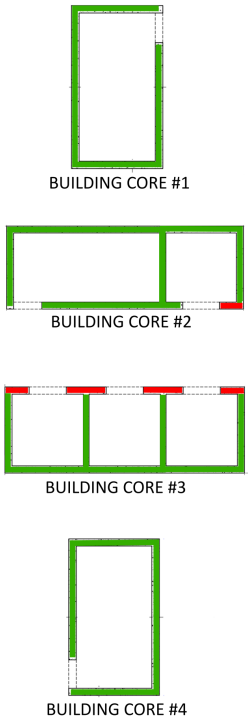

Figure 4.9: Walls of the cores modelled with infrmFB (in green) and with infrmDB (in red).

Regarding the applied loads on the cores, each core was loaded with the distributed load calculated using the expression presented in Section 4.1, multiplied by the influence area of each core. The border of this area was computed considering half of the distance between the core and an adjacent column. Core #1 and core #4 have an influence area of A_{infl}= 71.03 m^2 while the one of core #2 and core #3 is A_{infl}=159.6 m^2. In Table 4.4 the load of each floor insisting on each core is presented.
For core #1, core #2 and core #4 the total load was then divided equally by the four external walls of the core. For core #3, however, the load concerning the northern side was split in two equal parts between the two central short walls.
Finally, as described in Chapter 3, the 3D method involves lumping the masses in each slab. Therefore, the weight of the cores was included in the applied load at each slab. The loads were modelled as lumped masses at the nodes where they were applied, in such a way that they were accounted for also in the dynamic analysis. This is why they were all converted in ktons in Table 4.4.
Considering the portion of wall with the highest load, which is the one at the base, the resulting Axial Load Ratio (ALR) is 0.079 (7.9 %) and 0.106 (10.6%) respectively for cores 1-4 and cores 2-3.

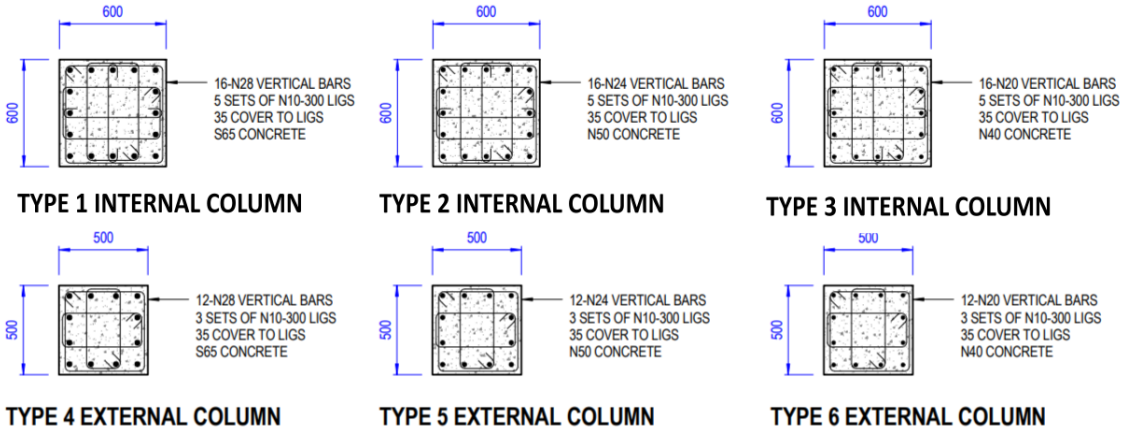

Figure 4.10: Different types of column, adapted from the provided plan.

4.1.2 Columns

The columns were added subsequently in the model. These structural elements are designed to support vertical loads, with the cores primarily bearing the lateral loads, and they were modelled with infrmFB elements, as these elements are the most accurate among the four inelastic frame element types of SeismoStruct, since they are capable of capturing the inelastic behaviour along the entire length of a structural member, even when employing a single element per member [36]. Both for internal and external columns, three different sections were defined, based on the floor at which they are found. This change in section with height is due to the lower loads that higher columns have to sustain. Thus, six different sections of columns are defined in total, presented in Figure 4.10.

In the same manner as for the concrete cores, the load on each column was determined by multiplying the distributed load by the influence area, adding the facade load by its corresponding area and finally its own weight. The influence area was computed for each column in the structure's geometry by considering an equal repartition between two adjacent columns, or between an adjacent column and core wall.

	A [m^2]	**Facade [m^2]**	**1-7 [KN]**	**1-7 [kton]**	**8 [KN]**	**8 [kton]**	**9 [KN]**	**9 [kton]**
C1&C26	18.90	6.09	188	0.0191	157	0.0160	-	-
C2-C7 & C20-C25	37.80	5.88	347	0.0354	315	0.0321	-	-
C8 & C19	13.13	5.13	138	0.0141	109	0.0111	-	-
C9 & C18	34.13	5.69	316	0.0322	284	0.0290	-	-
C10 -C12 & C15-C17	79.80	0.00	710	0.0724	664	0.0677	-	-
C13 & C14	34.44	0.00	327	0.0333	287	0.0292	-	-
Core #1 & Core #4	71.03	6.75	979	0.0998	979	0.0998	591	0.0603
Core #2 & Core #3	159.60	0.00	1899	0.1935	1899	0.1935	1329	0.1354

Table 4.4: Influence areas and applied lumped mass at each floor, on each column and core.

4.1.3 Horizontal elements

As presented at the beginning of this chapter, the considered structure is of flat slab type. As seen in Figure 4.1, the slab is a 250 mm thick two-way slab made of

reinforced concrete. No information was given on slab's reinforcement. To maintain consistency with the previous modelling done in Chapter 3 and due to the aforementioned reason, a rigid diaphragm constraint was applied at each floor level. This constraint was preferred over the rigid link constraint, which would have induced a much higher stiffness to the frame.
For the applied rigid diaphragm constraint, the centre of mass relative to each floor was defined and used as the master node in the constraint.

It should be noted that in the rigid diaphragm constraint all the constrained nodes will rotate/displace in a given plane maintaining their relative position unvaried, as if they were all connected by rigid lever-arms [36].
Hence, there is no flexural stiffness in the model's slab. In addition, the perimeter beam was not included in the model, as no section of it was provided in the given plans.
For the purpose of this research and for the application of the method to this building, these approximations are acceptable. Nevertheless, for having the optimal numerical model with the same exact behaviour of the real structure, also these contributions should be taken into account.

4.2 Numerical model characteristic

After the model was created, several analyses were conducted to gain a better understanding of its characteristics and behaviour. An eigenvalue analysis was initially conducted to determine the modal parameters of the structure and to understand the significance of each mode. Afterwards, a pushover analysis was carried out to define the capacity curve related to the structure, showing the displacements associated to a certain applied force in the force-displacement diagram.
Lastly, a non-linear dynamic time-history analysis was conducted to get the behaviour of the structure under a certain type of earthquake, also to understand if the hypothesis of the structure remaining linear is acceptable with this type of excitation. The modal properties, derived through further processing of the accelerations obtained from this analysis, were then compared to the results of the eigenvalue analysis.

4.2.1 Eigenvalue analysis

Eigenvalue analysis is used to define modal frequencies, modal shapes and other modal parameters. It is a purely elastic type of structural analysis, since material properties are taken as constant throughout the entire computation procedure [36].

For the specific building, where there are 8 floors and the roof over the lift overrun, 27 modes were requested. This to capture about 3 DoFs for each of the 9 slabs modelled with rigid diaphragms. Just the modes relative to the DoF along NS and EW direction and around Z axis will be considered.
It has to be noted that in a practical application higher modes are often difficult to be detected and thus are in practice neglected, accordingly with Eurocode 8 part 1

where it is stated that just modes whose effective modal mass is higher than 90 % should be considered (Section 4.3.3.3.1) [18]. In the table below are presented the first three modes for the three considered directions, with their respective modal mass. As it can be seen, they satisfy the just mentioned condition of having the cumulative Effective Modal Mass (EMM)> 90%. In Table 4.5 the direction along which the mode is mainly directed is underlined in bold. The modes along the NS have natural frequencies which are lower than the ones in the EW direction. This is mainly due to the geometry of the structure: the X axis results to be the weak axis along which there is a lower inertia and thus lower bending stiffness provided along that axis, which in an eigenvalue analysis results in lower natural frequencies of the flexural modes.

Mode	**Period [s]**	**Frequency [Hz]**	**$\mathbf{EMM_{NS}}$[%]**	**$\mathbf{EMM_{EW}}$[%]**	**$\mathbf{EMM_{Tor}}$[%]**
1	1.281	0.781	**67.97**	0.35	0.04
2	1.099	0.910	0.33	**66.78**	0.34
3	1.031	0.970	0.05	0.32	**67.68**
4	0.274	3.648	**18.32**	0.05	0.01
5	0.220	4.551	0.06	**18.58**	0.00
6	0.217	4.617	0.01	0.00	**18.37**
7	0.112	8.940	**6.19**	0.01	0.00
8	0.087	11.528	0.00	0.61	**5.60**
9	0.086	11.592	0.00	**4.05**	0.69
		Total	**92.93**	**90.76**	**92.71**

Table 4.5: Eigenvalue Analysis Results

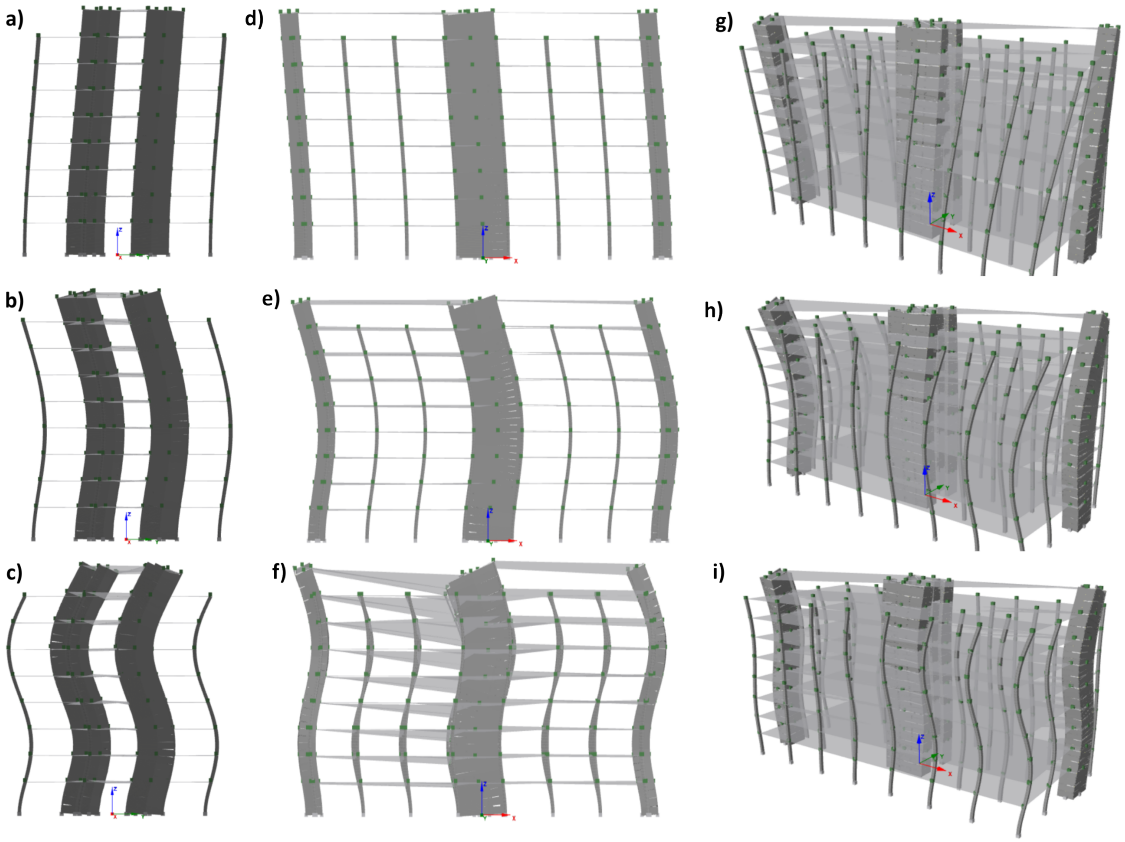

Figure 4.11: First three modes in the NS direction (a,b and c), in the EW direction (d, e and f) and in the Torsional direction (g, h and i).

4.2.2 Pushover analysis

In this type of analysis, an incremental load is applied to the nodes belonging to a certain slab of the structure. The incremental load P is proportional to a nominal load P^0 and is defined as:

$$P = \lambda P^0 \tag{4.5}$$

where λ is the load factor, whose interval is defined by the user. The analysis runs until a limit maximum load factor or when numerical failure is reached. This analysis is really useful to extract the capacity curve of the structure, i.e. the force-displacement curve. Since the Method presented in Chapter 3 holds on the hypothesis that the structure behaves linearly, it is important to understand until which applied load the hypothesis is valid, and when the structure enters the inelastic branch. For this reason, in Section 4.3, the 3D method was applied only after verifying that the accelerograms used as input did not induce any plasticity in the structure, ensuring that the hypothesis of linearity remained valid.

The effective height of the structure had to be computed to understand at which floor the incremental load should be applied. This parameter was computed in the NS and EW direction doing a weighted average of the effective modal heights relative

to N modes for which the total Effective Modal Mass (EMM)> 90 %:

$$h_{eff,NS/EW} = \frac{\sum_{r=1}^{N} h_{eff,NS/EW}^{(r)} EMM_{NS/EW}^{(r)}}{\sum_{r=1}^{N} EMM_{NS/EW}^{(r)}} \tag{4.6}$$

where $EMM_{NS/EW}^{(r)}$ and $h_{eff,NS/EW}^{(r)}$ are respectively the effective modal mass and the effective modal height in the NS or EW direction for the r-th mode. As previously introduced in Chapter 2, the latter is defined as [33]:

$$h_{eff,NS/EW}^{(r)} = \frac{\sum_{i=1}^{N_f} h_i m_i \Phi_i^{(r)}}{\sum_{i=1}^{N_f} m_i \Phi_i^{(r)}} \tag{4.7}$$

where h_i and m_i are respectively the height and the total mass of the i-th floor (see Table 4.6), and $\Phi_i^{(r)}$ is the modal shape for the r-th mode.

	Total mass [kton]	**Total rotational inertia [kton · m²]**
1-7	1.64	6.32E+02
8	1.54	5.86E+02
9	0.39	1.10E+02

Table 4.6: Total mass and rotational inertia for different floors

	Effective modal height [m]	
Mode	**NS**	**EW**
1	25.625	25.703
2	6.045	6.654
3	5.742	3.720
Effective height [m]	20.748	20.416

Table 4.7: Effective modal heights and effective heights in NS and EW directions.

Since as seen in Table 4.7 in both directions the weighted effective modal height is around 20 m, the incremental load was applied on the nodes belonging to the slab at the fifth floor (h=20.8 m).

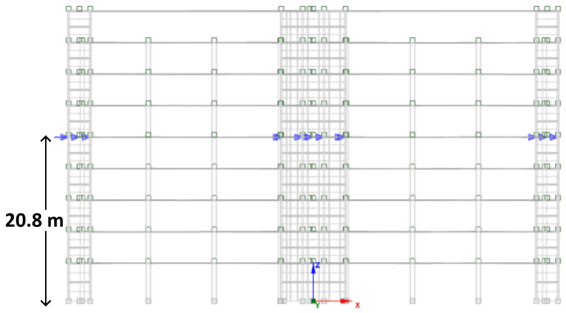

Figure 4.12: Height of the incremental force's point of application in the pushover analysis.

As suggested in the Seismostruct User manual (pg. 238)[36], to capture also the softening part of the curve a Load Control phase, with forces applied as incremental load, was followed by a Response Control one.
Some material reference points were also sought, to have a better understanding on how do the materials in the structure evolve with the increasing force-displacement being applied. The points material reference points that have been created in the Performance Criteria tab of Seismostruct are:

- the first cracking of concrete: considered, based on an average of the material properties of the different concrete classes used, to first occur at a strain of 0.00015 (0.015 %)
- the first crushing of concrete: set, according to the literature [31] for unconfined walls in Australia such as the ones in the considered structure, to occur with a strain of -0.006 (-0.6 %)
- the first yielding of steel: as for concrete, doing an average between material properties, it was set to occur at a strain of 0.0024 (0.24 %)
- the first fracture of steel: set, as suggested by the Seismostruct User Manual [36], at a value of strain of 0.05 (5 %).

To extract the correct force-displacement curves, the displacement of the nodes at the previously considered height (20.8 m) were considered (Figure 4.13).

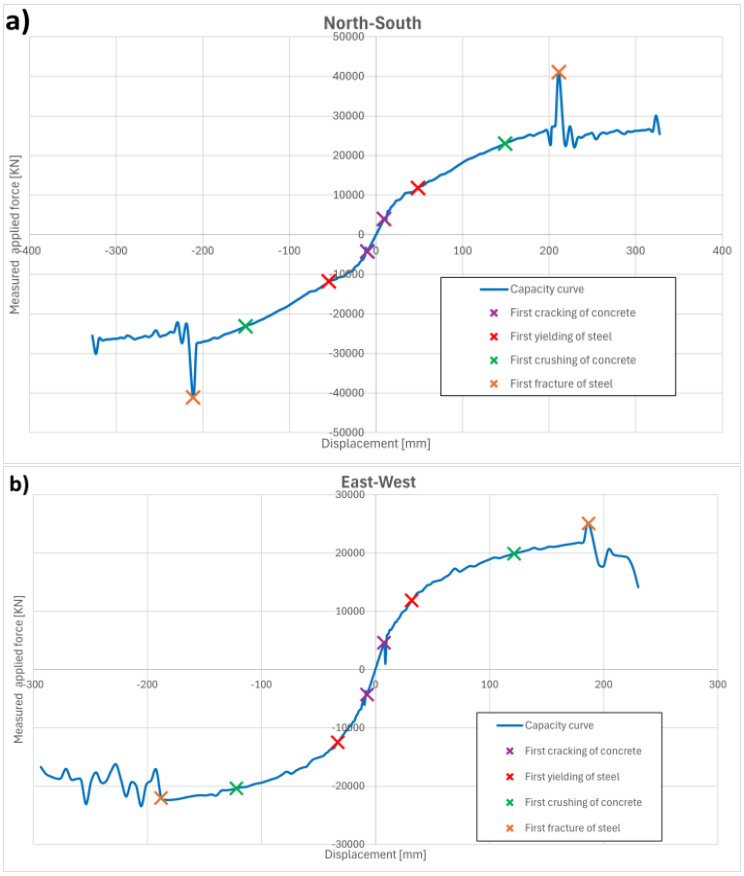

Figure 4.13: Capacity curves in the NS (a) and EW (b) directions, with some material reference points.

As shown in the two curves, the global behaviour of the structure is initially elastic in both directions, with a gradual inelastic response starting around 10000 KN. The elastic curve is slightly steeper in the EW direction, confirming the results of the eigenvalue analysis on a higher stiffness along that direction.

Additionally, in the East-West direction, a snap-through phenomenon is observed, corresponding to the initial cracking of concrete. This results in a sudden loss of capacity due to the redistribution of stress from a section where both concrete and steel contribute, to a section where the concrete contribution is eliminated due to cracking.
As the building is symmetric in the two directions, it is remarked that the capacity curve is almost symmetric in the two positive and negative branches.
At the same time, since there are different dimensions in plan in the two NS and EW directions, the total capacity when bending the structure in one direction differs from the other. In particular, it is noted that when bending occurs along the weak axis, with the load applied in the NS direction, the structure exhibits greater capacity and reaches numerical failure after a larger displacement. Additionally, as soon as the steel's fracture limit is reached, the global behaviour is more irregular, with a short softening branch occurring right before numerical divergence.
Both in the N-S and E-W direction the reference points are reached in the follow-

ing order: cracking of concrete in tension, yielding of steel, crushing of concrete in compression and fracture of steel.

4.2.3 Dynamic time-history analysis

After determining the capacity curve, which indicates the boundaries between the elastic and inelastic behaviour of the structure, a dynamic time-history analysis was performed. This analysis provided a detailed understanding of how the structure responds to time-varying loads, offering insights into its performance under realistic conditions.
In this type of analysis, the load, which is applied at the base nodes, consists in a set of time-history accelerations simulating seismic motion. These accelerations can be from a recorded past earthquake or can be artificially created.

The advantage of this analysis is that it can simulate the response of the considered structure under any possible seismic event. Additionally, this type of analysis closely mirrors a real-world scenario where a structure is equipped with accelerometers to compute its dynamic properties. It allows replicating the procedures that would be done on an actual structure. However, compared to a real structure, a numerical model offers much greater control over all parameters, enabling more detailed and precise understanding of results.

Important attention has to be dedicated to a correct modelling of damping. Looking through similar models among the verification models provided by Seismostruct it was decided to impose a tangent stiffness proportional damping with a damping ratio ξ=5%. With the first natural period of the structure being T_1=1.28 s, the damping parameter is computed as [36]:

$$\alpha_K = \frac{T_1 \xi}{\pi} = 0.02037 \tag{4.8}$$

In this section, the natural frequencies and modal shapes were computed through the use of the Fourier Analysis. They were then compared with the results from the Eigenvalue analysis presented in Section 4.2.1.
It was initially assumed that the input accelerogram was a white noise acceleration. This choice was done as the latter can be filtered in such a way that it covers a wide range of frequencies, so that all the natural frequencies in a defined interval can be extracted with the use of a Fast Fourier Transform.
The considered filtered white noise accelerations had the following characteristics, applied also through the use of an Infinite Impulse Response (IIR) filter:

- PGA of 0.1g
- duration of 120 s
- frequency lower and upper cut-off of respectively 0.1 and 20 Hz
- sampling frequency of 50 Hz (time step of 0.02 s)

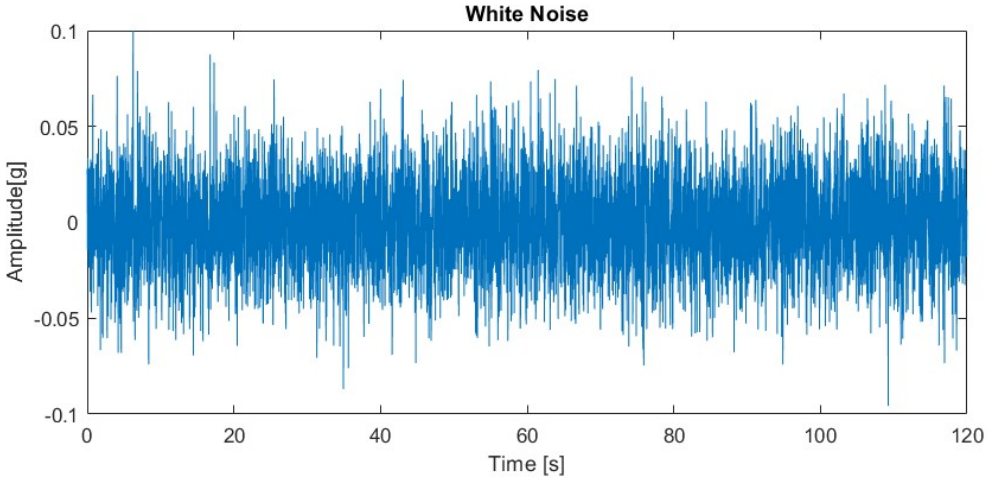

Figure 4.14: White noise excitation

The generated white noise accelerogram was then applied in both NS and EW directions at the base nodes. To simulate a real instrumentation layout, accelerations were extracted from specific designated nodes, where it would be likely that an accelerometer could be placed in a real structure. To capture in the best manner the flexural behaviour in the two directions and the torsional behaviour, as found in many guidelines presented in Chapter 2, three uniaxial accelerometers are needed. For each floor, in the NS direction two set of accelerations were extracted, positioned in the two opposite sides of the slab, while in the EW direction just one acceleration was considered in one of the points where the NS accelerations had already been taken, as seen in Figure 4.15.
Even if the sensor in the EW direction is not perfectly coincident with the centre of mass along for the Y coordinate, it was observed that the torsional contribution was negligible in that point, and thus it was an acceptable approximation to consider it as if it was aligned with the centre of mass.

Additional information about the structure in the frequency domain can be obtained by computing the Fourier Transform using a Fast Fourier Transform (FFT) algorithm. In Figure 4.16 the three diagrams represent the amplitude of the Fast Fourier Transform with respect to the frequency, respectively for N-S, E-W and Torsional direction. These diagrams were generated using an adapted version of an existing code. The original code source was adapted from a previous study by Hoult [24], which had its corresponding data available for download via an open-data repository [23].
The presence of two accelerometers in the N-S direction at the East and West side of each slab (see Figure 4.15) made possible to compute the FFT of the rotational acceleration, obtained in the following way:

$$acc_{rot} = \frac{acc_{NS_1} - acc_{NS_2}}{B} \tag{4.9}$$

where acc_{NS_1} and acc_{NS_2} are the two accelerations in the N-S direction and B is the distance in plan between the two accelerometers.

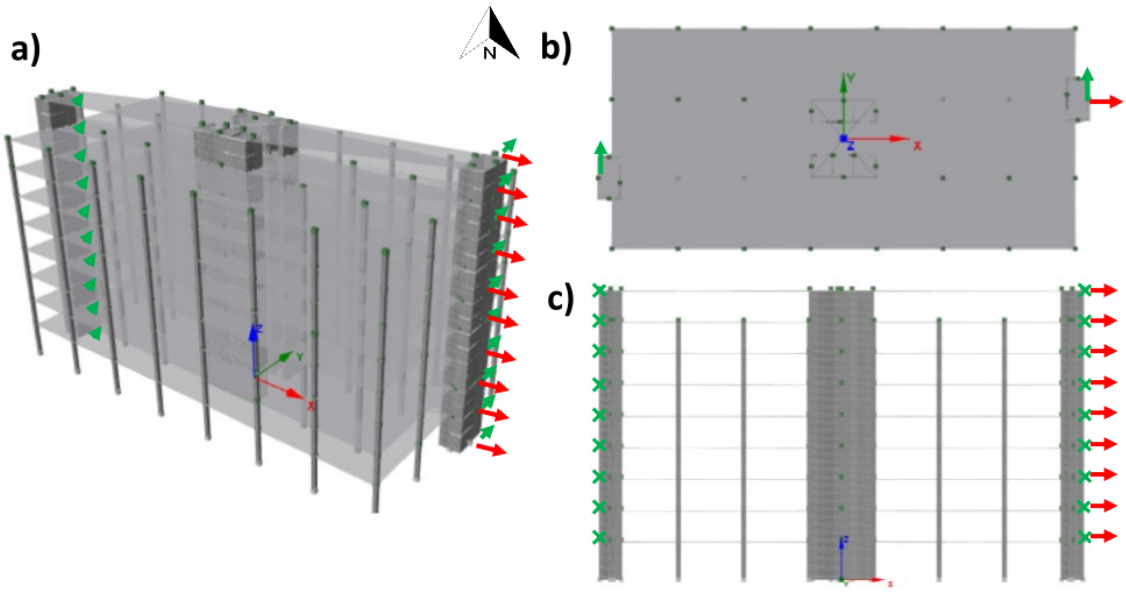

Figure 4.15: Position of accelerometers considered, seen in perspective (a), from the top (b) and from the front (c) of the structure. The red arrows stand for accelerations measured along the EW direction, while the green ones for accelerations along the NS direction.

As it can be seen in Figure 4.16, despite the structure was excited with a white noise ground acceleration, the higher modes result to be difficult to detect from the diagrams. Probably with a longer duration in time of the input accelerogram also the higher modes would have been more easily detected. For this reason, just the first two were considered as meaningful in this situation. The results obtained by this procedure were then compared with the ones from the eigenvalue analysis, presented in Section 4.2.1. Also in this case, the natural frequency along the NS are lower due to lower stiffness in this direction.

Since for the 3D method of Chapter 3 the modal shapes are needed, they were obtained by comparing, for a given natural frequency, the magnitude in the amplitude Fourier Spectrum at each floor with the so-called peak picking procedure. They were all normalised and adapted in sign so that they could be compared with the ones given as output from the eigenvalue analysis (Figure 4.18). The results obtained with the FFT algorithm are very similar to the modal shapes from the eigenvalue analysis, specially for the first mode. The biggest difference is observed for the Torsional natural frequencies, where at the second mode there is a reduction of 30 % from the eigenvalue's one.

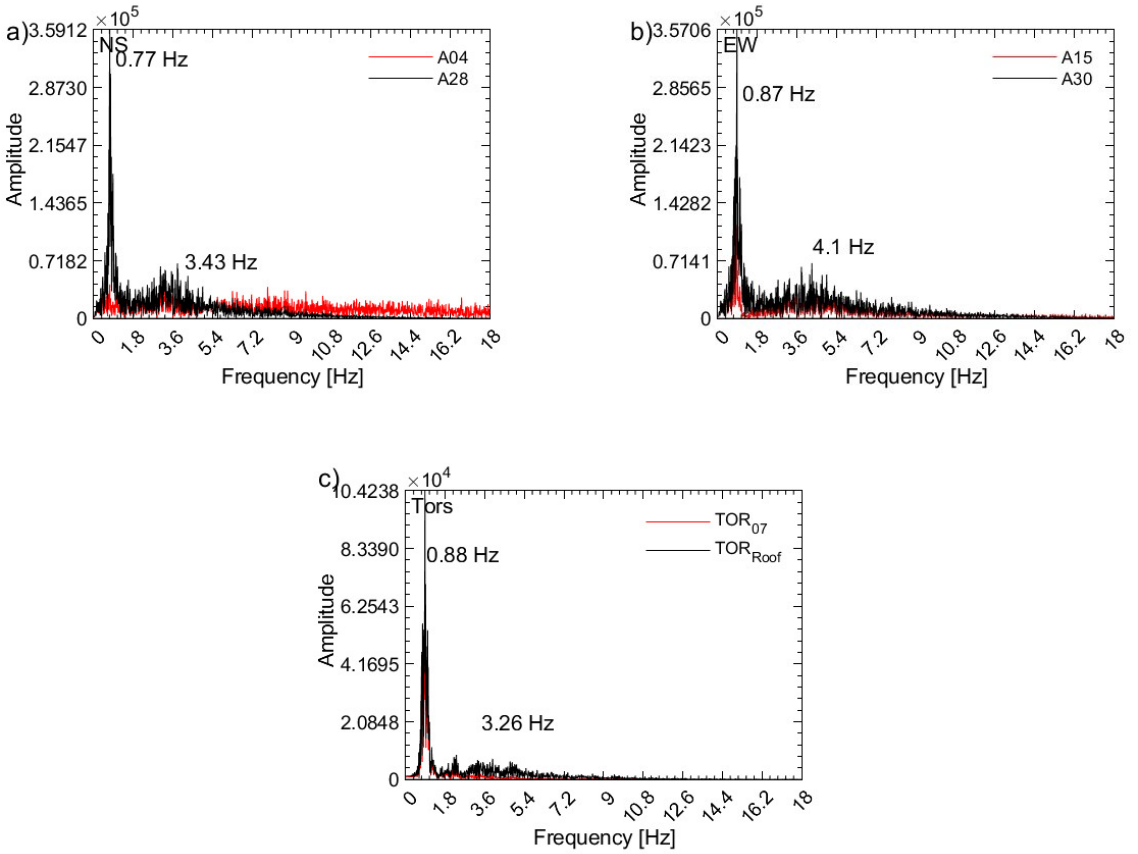

Figure 4.16: Amplitude of the Fourier Transform for the NS (a), EW (b) and Torsional (c) direction.

Mode	FFT [Hz]	Seismostruct [Hz]
1	0.77	0.78
2	3.43	3.65

(a) NS

Mode	FFT [Hz]	Seismostruct [Hz]
1	0.87	0.91
2	4.10	4.55

(b) EW

Mode	FFT [Hz]	Seismostruct [Hz]
1	0.88	0.97
2	3.26	4.62

(c) Torsional

Figure 4.17: Comparison between computed natural frequencies (FFT) and those obtained from the eigenvalue analysis in Seismostruct.

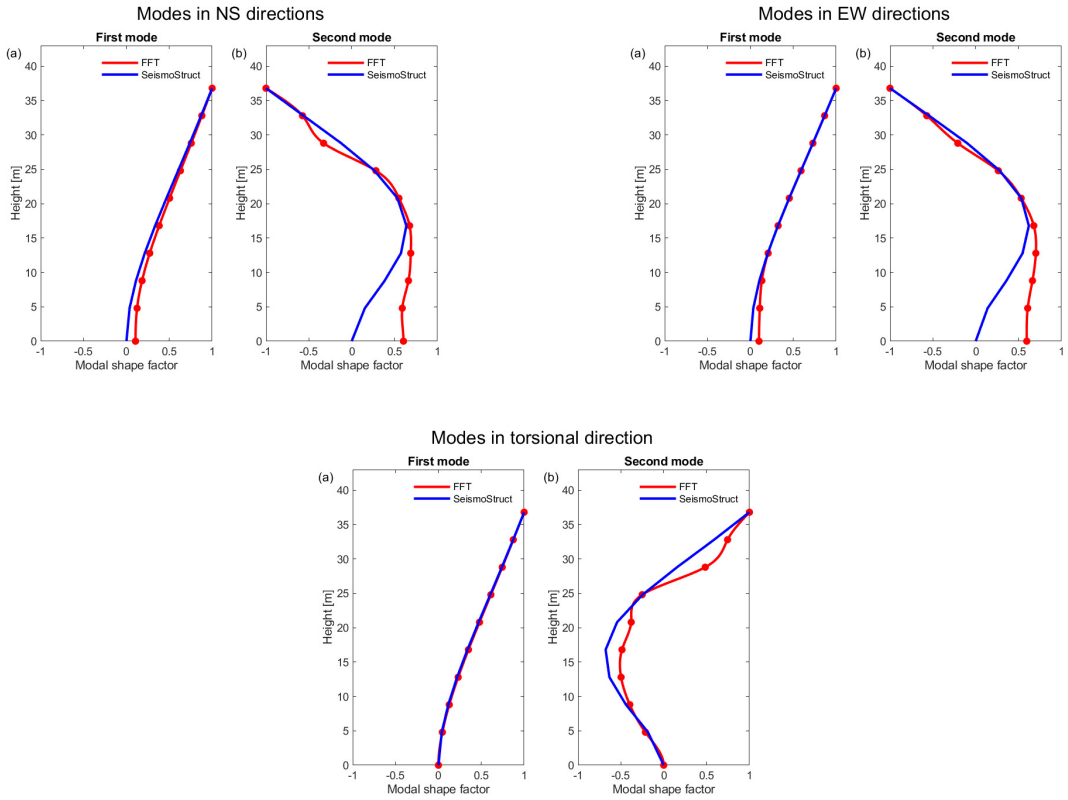

Figure 4.18: For the three directions, first (a) and second (b) mode, both computed with eigenvalue analysis from Seismostruct (in blue) and with the white noise excitation applied to the structure (in red).

4.3 Application of the method

In this third part of the chapter, the method proposed in Chapter 3 was applied to the numerical model, and the results are presented. The purpose of this part is to study if the conclusions drawn previously still hold if applied to a more realistic numerical model.
A numerical model is a crucial tool for maintaining precise control over the behaviour of a structure and achieving clearer results. At first, the method was applied using the modal shapes extracted from the eigenvalue analysis. After, the same procedure was applied but with the outputs from the dynamic time-history analysis.
While previously a white noise excitation was used to compute alternatively the modal parameters of the structure, in this case to represent a more realistic situation a recorded and a worst case scenario earthquake accelerograms have been applied to the model as ground motion.

4.3.1 Values from eigenvalue analysis

The outputs of the eigenvalue analysis are the most precise ones as they compute, with the given masses and stiffnesses, the modal parameters. The optimal placement of sensors in this situation will thus be used as a benchmark for the following cases, where the modal parameters are computed with measured accelerations. In the following, the γ functions computed with Equations 3.13 to 3.15 are plotted for this specific case. In Figure 4.19 the evolution of the three γ functions with N_m modes is shown. The positions of one and two sensors are easily identifiable. However, for understanding the optimal placement of three sensors, simply considering the third mode of each DoF does not lead to have three points of local minimum of the γ functions, as seen in Figure 4.19. Conversely, it is noticed that there are some subsequent floors at which the smaller values of γ are found, such as floor 6,7 and 8 for the EW direction. Placing the sensors at these floor could on one side have the advantage of having a measure on the interstory drift, but at the same time diverges largely from the values found in Chapter 3 for a structure with 10 floors.
Considering higher modes with similar modal shape could be a solution to converge to the results of that chapter. In effect, also in the previous chapter, with the structure having an eccentric mass distribution, modes with similar modal shapes were also found.

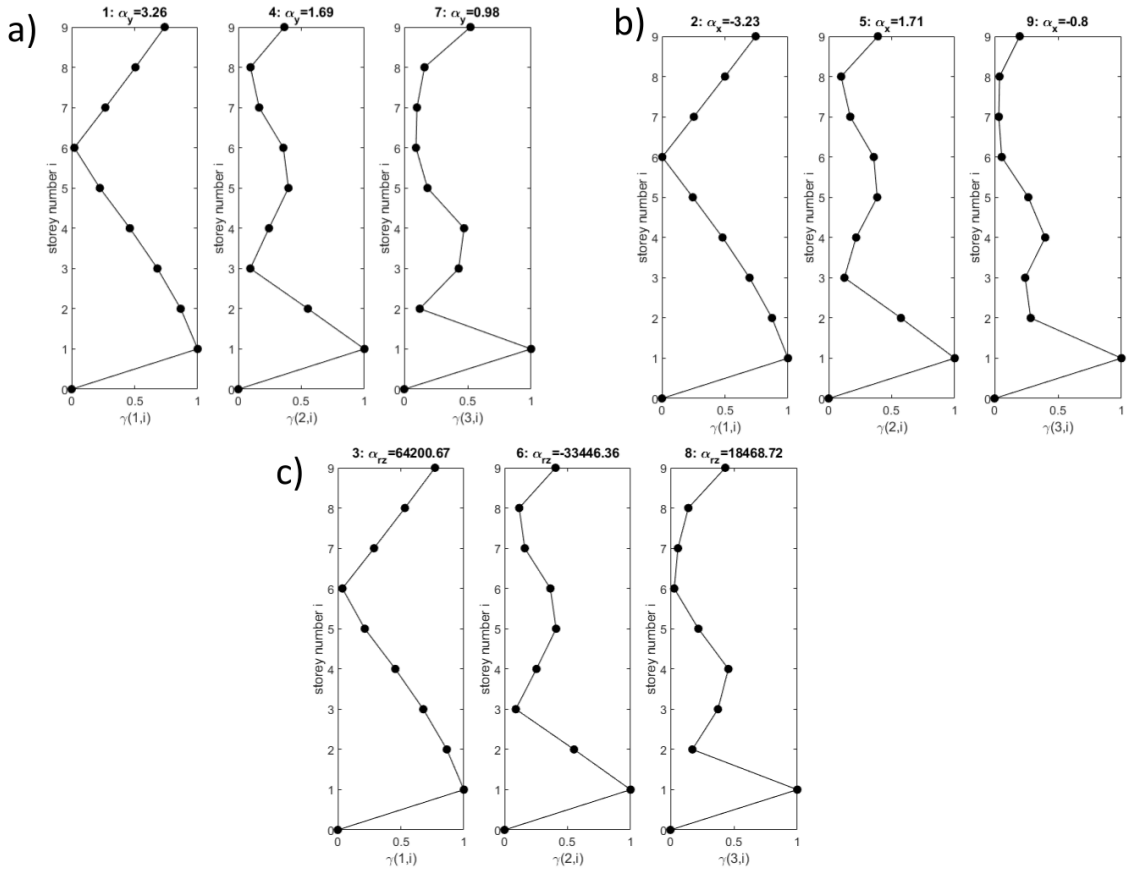

Figure 4.19: Evolution of γ in NS (a), EW (b) and torsional (c) direction in function of N_m modes considered.

N_s	Direction		
	NS	EW	Tor
1	6	6	6
2	3-8	3-8	3-8
3	2-6-7	6-7-8	2-6-7

Table 4.8: Table showing optimal sensor placement, according to the first three modes of each direction.

The results in any case are coincident in the NS and Torsional direction, showing coherently to the results of the previous chapter that the torsional modes behave similarly to the flexural ones.

Figure 4.20: Epicentre of the recoded earthquake [21].

4.3.2 Earthquake recorded in Darwin

For this second analysed situation, it was considered that the numerical model, representing a typical Australian Structure, was undergoing the soil motion measured during the 7.6 M_w Banda Sea's earthquake which happened on the 09/01/2023 and that was measured in Darwin by the DRS (Darwin Rock Store) seismogram, located 600 km away from the epicentre (Figure 4.20).

Parameter	Value
Distance from epicentre [km]	600
Hypocentral depth [km]	67
Moment magnitude [M_w]	7.6
PGA in Darwin [g]	NS:0.017-EW:0.019

Table 4.9: Data for Banda Sea's earthquake [21].

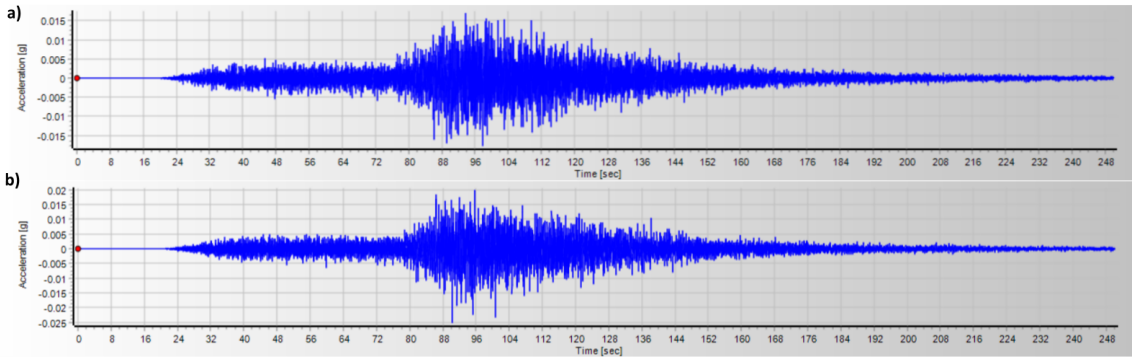

Figure 4.21: Recorded accelerograms in the DRS seismogram, in the NS direction (a) and in the EW direction (b).

Following a similar procedure as the one applied with the White Noise excitation, also in this case the amplitude of the Fourier Transform was computed and used to detect the natural frequencies and, consequently, the modal shapes of the detected modes with the peak peaking procedure.

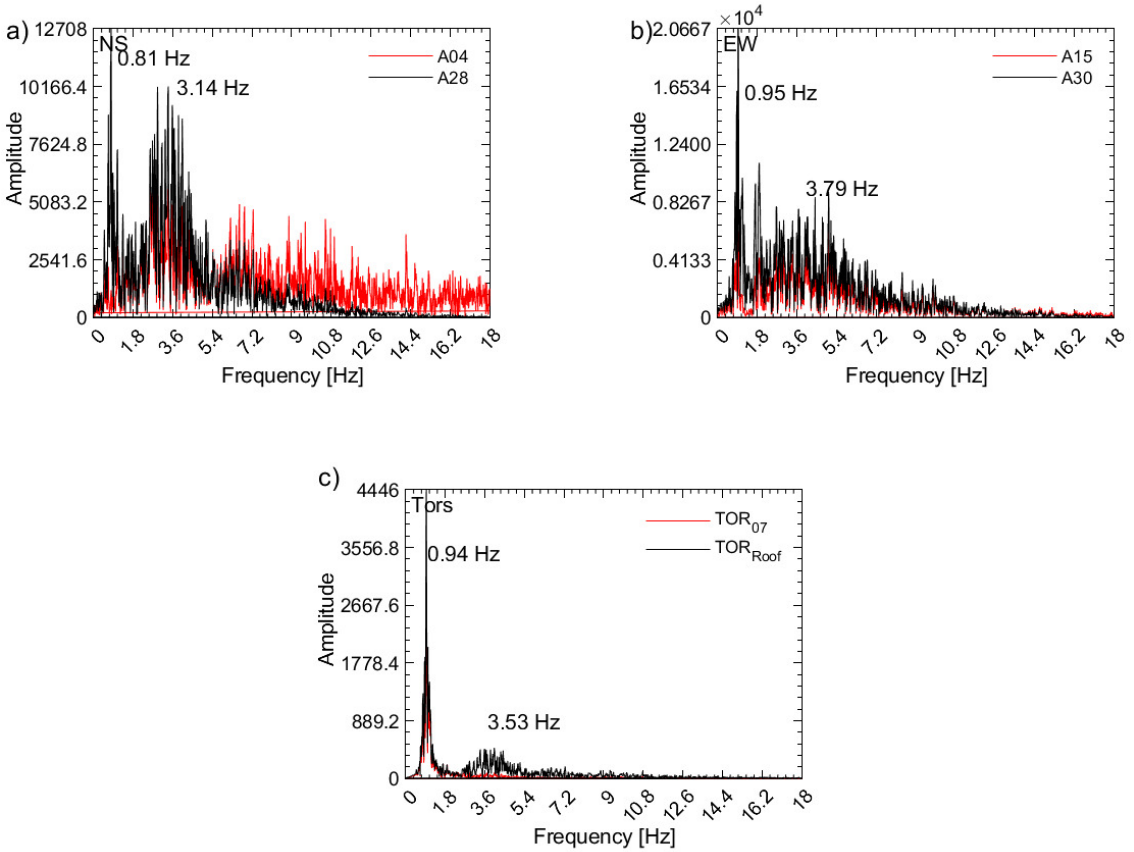

Figure 4.22: Amplitude of the Fourier Transform for the NS (a), EW (b) and Torsional (c) direction.

Mode	FFT [Hz]	Seismostruct [Hz]
1	0.81	0.78
2	3.14	3.65

(a) NS

Mode	FFT [Hz]	Seismostruct [Hz]
1	0.95	0.91
2	3.79	4.55

(b) EW

Mode	FFT [Hz]	Seismostruct [Hz]
1	0.94	0.97
2	3.53	4.62

(c) Torsional

Figure 4.23: Comparison between computed natural frequencies from the response measured with the recorded earthquake (FFT) and those obtained from the eigenvalue analysis in Seismostruct.

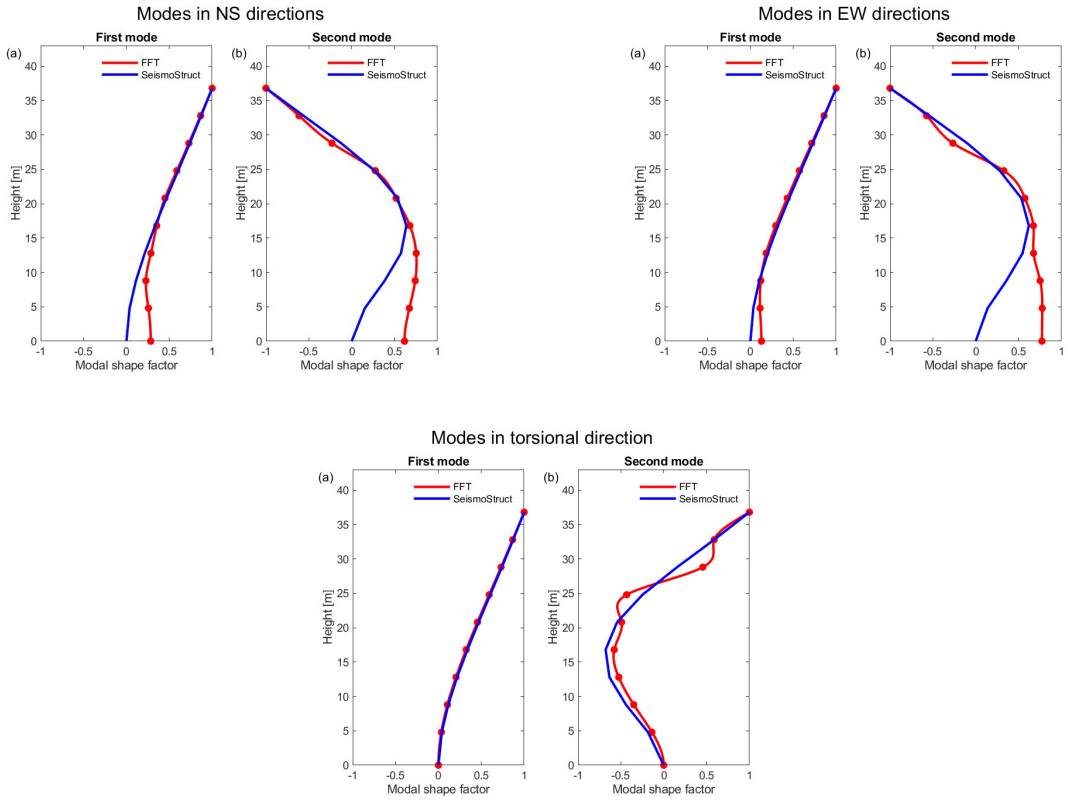

Figure 4.24: For the three directions, first (a) and second (b) mode, both computed with eigenvalue analysis from Seismostruct (in blue) and with the recorded earthquake excitation applied to the structure (in red).

Once the modal shapes were defined, the 3D method was applied to this case, resulting in the following γ functions. As seen in Figure 4.25 and Table 4.10, for one sensor the point of minimum coincides with the one found in the previous Section, suggesting the ideal placement of one sensor at the sixth floor.

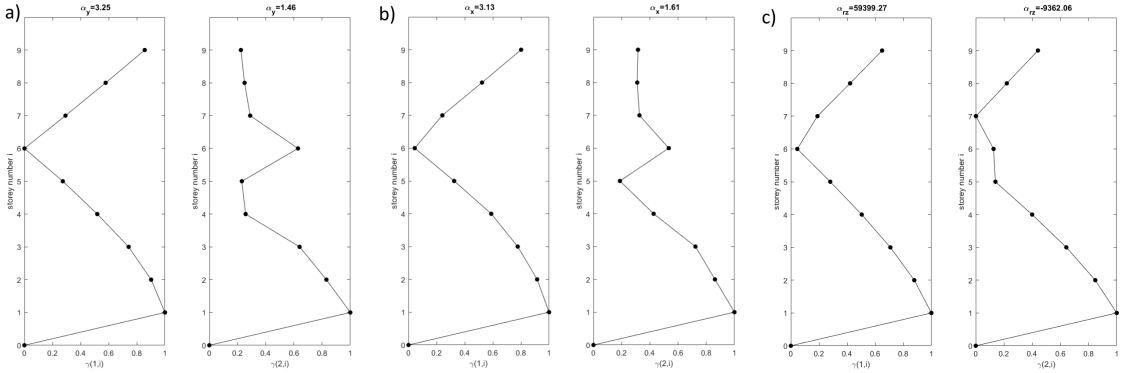

Figure 4.25: Evolution of γ in NS (a), EW (b) and torsional (c) direction in function of N_m modes considered.

On the other hand, the results when considering just the first two modes display two points of local minimum just in the EW direction (5 and 8), while in the other two directions the floors with the smaller value of γ were selected. Comparing the results for two sensors with those from the previous section a significant difference is revealed, particularly in the position of the lower sensor. As shown in Figure 4.24, the modal shapes for the first mode are nearly coincident. However, there is a noticeable difference for the second mode. Specifically, in the NS and EW directions, there is a significant shift at the base of the structure, which accounts for the lower sensor being placed at a higher floor.

N_s	Direction		
	NS	EW	Tor
1	6	6	6
2	5-9	5-8	6-7

Table 4.10: Table showing optimal sensors' placement, according to the first two modes in each direction.

4.3.3 Artificial earthquake

After analysing the structure under a real earthquake that shook the city of Darwin, another scenario was considered.
In order to see the behaviour of the structure in the worst case scenario that could happen in the zone, an earthquake with a moment magnitude M_w=9 with epicentre at a distance from Darwin of 400 km was considered, according to Leonard et al. [27].
Starting from the information in Table 4.11, the medium Response Spectrum was generated, and through the use of the software SeismoArtif an artificial accelerogram could be extracted(4.26).

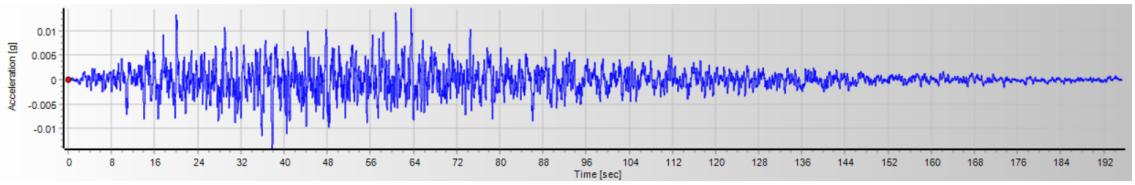

Figure 4.26: Artificial accelerogram produced with the data in Table 4.11.

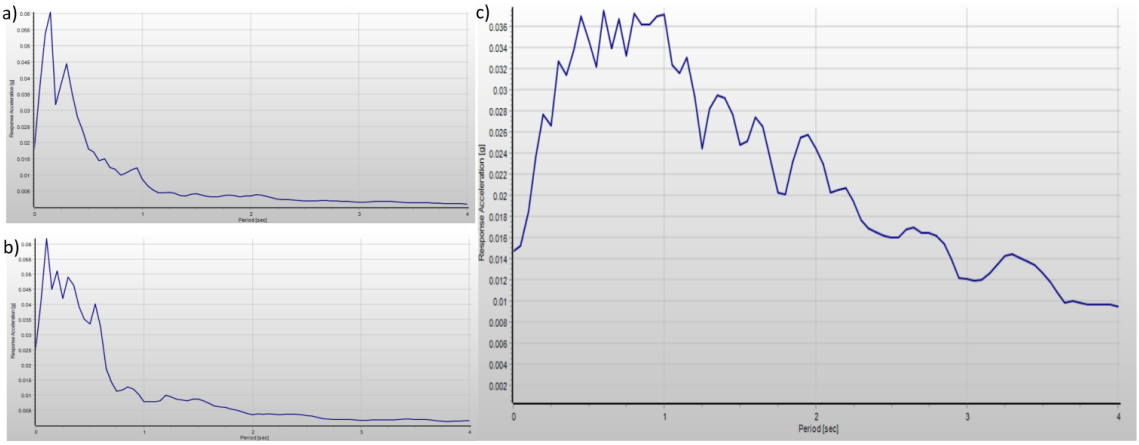

Figure 4.27: Pseudo-acceleration response spectrum of the recorded earthquake in the NS (a) and EW (b) direction, and of the artificial earthquake (c).

Parameter	Value
Distance from epicentre [km]	400
Hypocentral depth [km]	55
Magnitude [M_w]	9
PGA in Darwin [g]	0.015

Table 4.11: Data used to produce the artificial earthquake

It is noted that in this case the PGA is lower (0.015g) than in the recorded earthquake (EW=0.0199g and NS=0.0170g). Nevertheless, this does not mean that the earthquake would have a lower impact on the population of Darwin. A whole set of other parameters determine the gravity of an earthquake, such as its duration, its natural frequencies and the local soil conditions.
Indeed, as it can be seen from the Pseudo-acceleration Response Spectrum (Figure 4.27), this earthquake would affect a wider range of structures, covering a wide range of natural periods with an almost constant pseudo-acceleration. On the other hand, in the previous section, the response spectra were with higher maximum intensities of Pseudo-acceleration but in a narrower range of natural periods.
The generated artificial accelerogram was applied in both N-S and E-W direction of the structure simultaneously.

Also in this case, the peak natural frequencies and the corresponding modal shapes were computed. However, since plotting the FFT algorithm only the first natural mode in all directions could be detected, the computations in this section focus exclusively on this mode. Considering higher modes was deemed less mean-

ingful because the amplitude peaks of the Fourier Transform were significant only for the first mode, as seen in Figure 4.28.
These findings suggest that a strong earthquake, such as the one presented herein, would primarily excite only the first mode of the modelled structure, which is the only one that can be visualized.

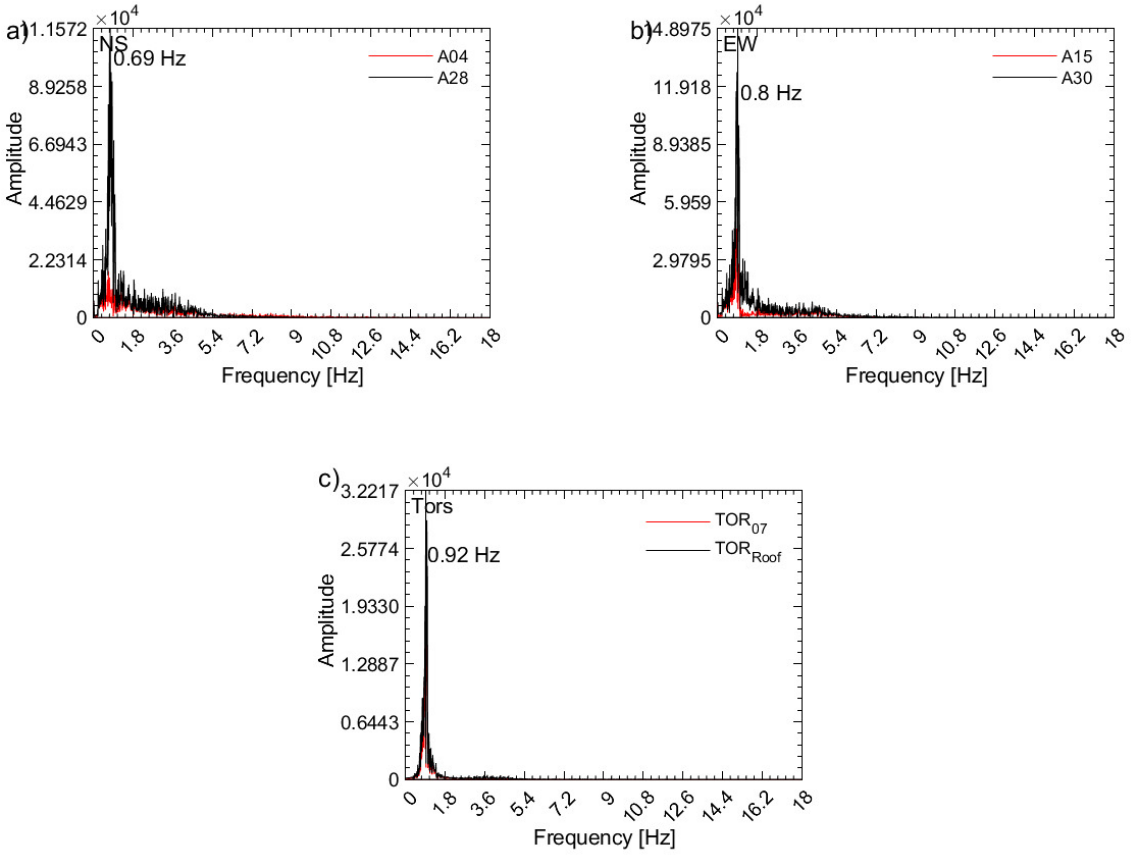

Figure 4.28: Amplitude of the Fourier Transform for the NS (a), EW (b) and Torsional (c) direction.

Direction	FFT [Hz]	Seismostruct [Hz]
NS	0.69	0.78
EW	0.8	0.91
Torsional	0.92	0.97

Table 4.12: Comparison, for the first mode, between computed natural frequencies from the response measured with the artificial earthquake (FFT) and those obtained from the eigenvalue analysis in Seismostruct.

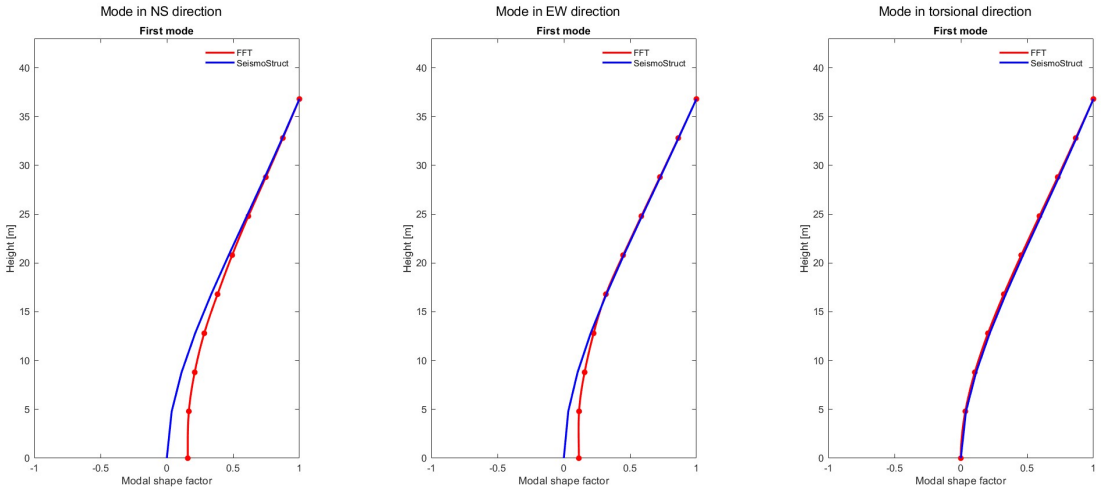

Figure 4.29: First mode for the three directions, both computed with eigenvalue analysis from Seismostruct (in blue) and with the artificial earthquake excitation applied to the structure (in red).

Once the modal shapes were defined, the 3D method was applied to this case resulting in the following γ functions. The position of one sensor coincides with the sixth floor for all the three directions, in the same way as it did in the previous sections.
Despite the totally different nature of the earthquake and the different scenario, the optimal placement of one sensor results to be the same. Unfortunately, it was not possible to capture the higher modes to have a wider comparison with the previous sections regarding also two or three sensors.

As mentioned before, it is likely that with a longer excitation also the higher modes could have been detected.
For a structure of this type, it can be concluded that it would be more effective to use a long duration white noise excitation. This approach would enable the identification of at least the first two or three modes, providing the modes whose sum of the effective modal mass exceeds 90 %. By capturing multiple modes, applying a white noise excitation offers a more comprehensive understanding of the structure's dynamic behaviour.

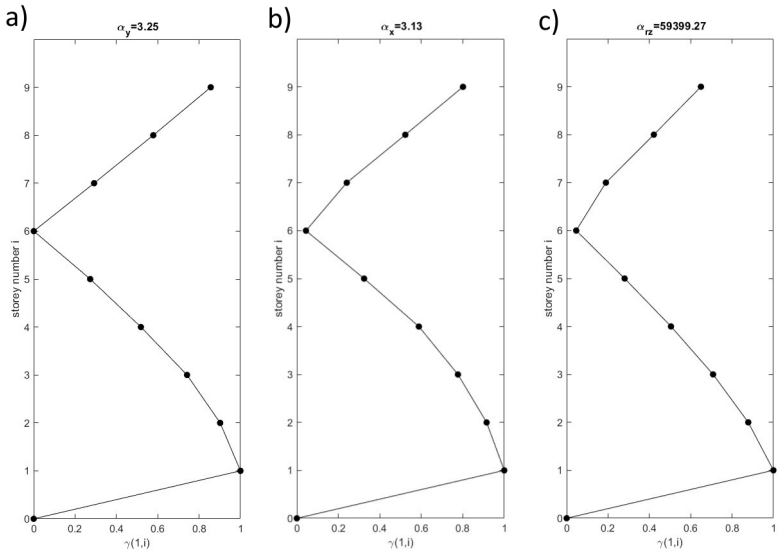

Figure 4.30: Evolution of γ in NS (a), EW (b) and torsional (c) direction considering the first mode.

4.3.4 Comparison between the different cases and with the 2D method

In this final section of the chapter, the previously presented results are compared and discussed, to have a proper overview and draw consistent conclusions.

First, since the natural frequencies and the modal shapes of the structure have been extracted in different ways, a comparison has been done in the tables in Figure 4.31. It is remarked that globally the natural frequencies computed with the FFT algorithm well approximate the results obtained in the eigenvalue analysis, with the general tendency to decrease their values. Nevertheless, as the reconstructed modal shapes were quite similar for the different cases, the 3D method resulted to converge to similar optimal placement, especially for what concerns the first mode.

Secondly, it was noted that the optimal sensor placement in all three directions, accounting for both flexural and torsional modes, matched the positioning obtained when considering the building as a 2D frame and focusing solely on the flexural modes. This finding is consistent with the observations from the previous chapter.

Mode	FFT white noise [Hz]	FFT recorded [Hz]	FFT artificial [Hz]	Seismostruct [Hz]
1	0.77	0.81	0.69	0.78
2	3.43	3.14	-	3.65

(a) NS

Mode	FFT white noise [Hz]	FFT recorded [Hz]	FFT artificial [Hz]	Seismostruct [Hz]
1	0.87	0.95	0.8	0.91
2	4.10	3.79	-	4.55

(b) EW

Mode	FFT white noise [Hz]	FFT recorded [Hz]	FFT artificial [Hz]	Seismostruct [Hz]
1	0.88	0.94	0.92	0.97
2	3.26	3.53	-	4.62

(c) Torsional

Figure 4.31: Comparison between computed natural frequencies (FFT) and those obtained from the eigenvalue analysis in Seismostruct.

Chapter 5

Case study-Atwood Building

Until this chapter, the 3D method was applied in the controlled environment of numerical analysis. After modelling a structure in a Finite Element software, the procedure was applied to the numerical model. Modelling in a FE software has the advantage that all the parameters can be extracted and monitored, allowing the user to have a wide control over the different quantities and thus on the results.

However, in a real situation it is not always possible to have a corresponding digital twin of the structure under investigation, or there is not enough time or information to create it.
The purpose of this chapter is to apply the aforementioned passages to find the optimal placement of sensors in a real existing structure, starting from accelerations recorded on the structure, and having limited control over the parameters characterising it.
The purpose of these elaborations is to have a quick output of sensors' optimal positioning without having to create a numerical model of the structure but just with a defined set of recorded accelerations.

For the purpose of this chapter, it was chosen to consider the Atwood Building in Anchorage, Alaska (Figure 5.1). This structure was evaluated as appropriate for this research as it is extensively equipped with accelerometers throughout its height, reason why it was often used for S^2HM researches.
The Atwood Building, placed in a highly seismic active region, also showed to have an important torsional response [6], making it ideal for the application of the method considered in this thesis, were the contribution of torsional modes in the dynamic behaviour of the structure was investigated.

At first, a general overview of the structure will be presented, followed by a section dedicated to the computations of modal parameters with ambient vibrations and application of the 3D method. Finally, it was evaluated if the conclusions driven from the previous analysis were still valid in the case of a strong earthquake shaking the structure.

Figure 5.1: Atwood building [8].

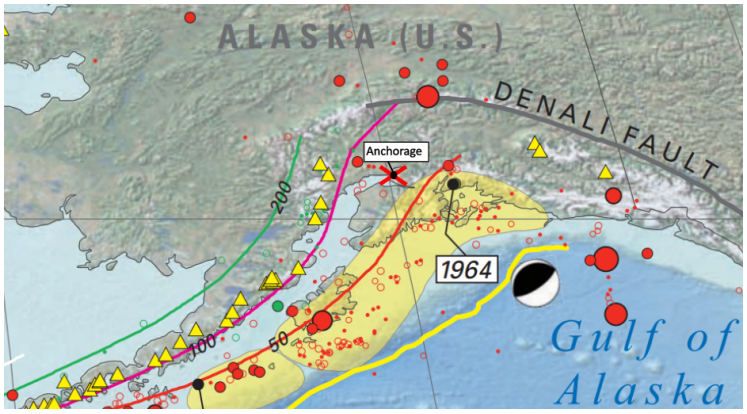

Figure 5.2: Map showing the main faults, the most important earthquakes (red dots) and volcanoes (yellow triangles) near Anchorage, adapted from [46].

5.1 The Atwood Building: general description

The Atwood building is a 20-storey moment resisting framed (MRF) office building that was build in 1980 according to provisions of 1979 *Uniform Building Code UBC* [6]. It is located in North-West downtown of Anchorage, in Alaska, in a highly seismic active zone [7] (Figure 5.2). The site geology is deep alluvium, with a measured V_s30=260 m/sec and a site class D [8]. The structure measures 39.6 mx39.6 m in plan and 80.5 m in height from the street level. Counting also the basement, it reaches a total height of 84 m. In the centre of the building, a shear-walled core with 14.6 x14.6 m in-plan is placed. The building foundation does not include piles and consists of a 1.52-m thick reinforced-concrete mat under the core, along with a 1.37-m thick reinforced-concrete perimeter mat connected by grade beams.
The instrumentation consists of a 24-bit IP-based data logger and an array of 32 accelerometers distributed on 10 levels, including basement, 1st (ground), 2nd, 7th, 8th, 13th, 14th, 19th, 20th, and roof. This accelerometer array records 200 samples-per-second from each channel. Further details on the structure and instrumentation can be found in Wen and Kalkan [48].

The seismic monitoring system of the building comprises and integrates a structural superstructure and foundation array and a site surface and downhole array (Figure 5.3). This configuration, consistent with the guidelines by COSMOS presented in Chapter 2, is designed to detect lateral north-south NS and east-west EW motions throughout the building, and vertical motions in the basement to assess a) translational motion, b) torsional motion, c) interstory drift displacement between selected two consecutive floors or average drift between any two floors, and d) rocking of the building. The structural array is complemented by an extensive free-field site array, located approximately one city block (500 m) south of the building, and consisting of seven triaxial accelerometers, one at the surface and six in boreholes with depths ranging from approximately 5 to 60 m [6].

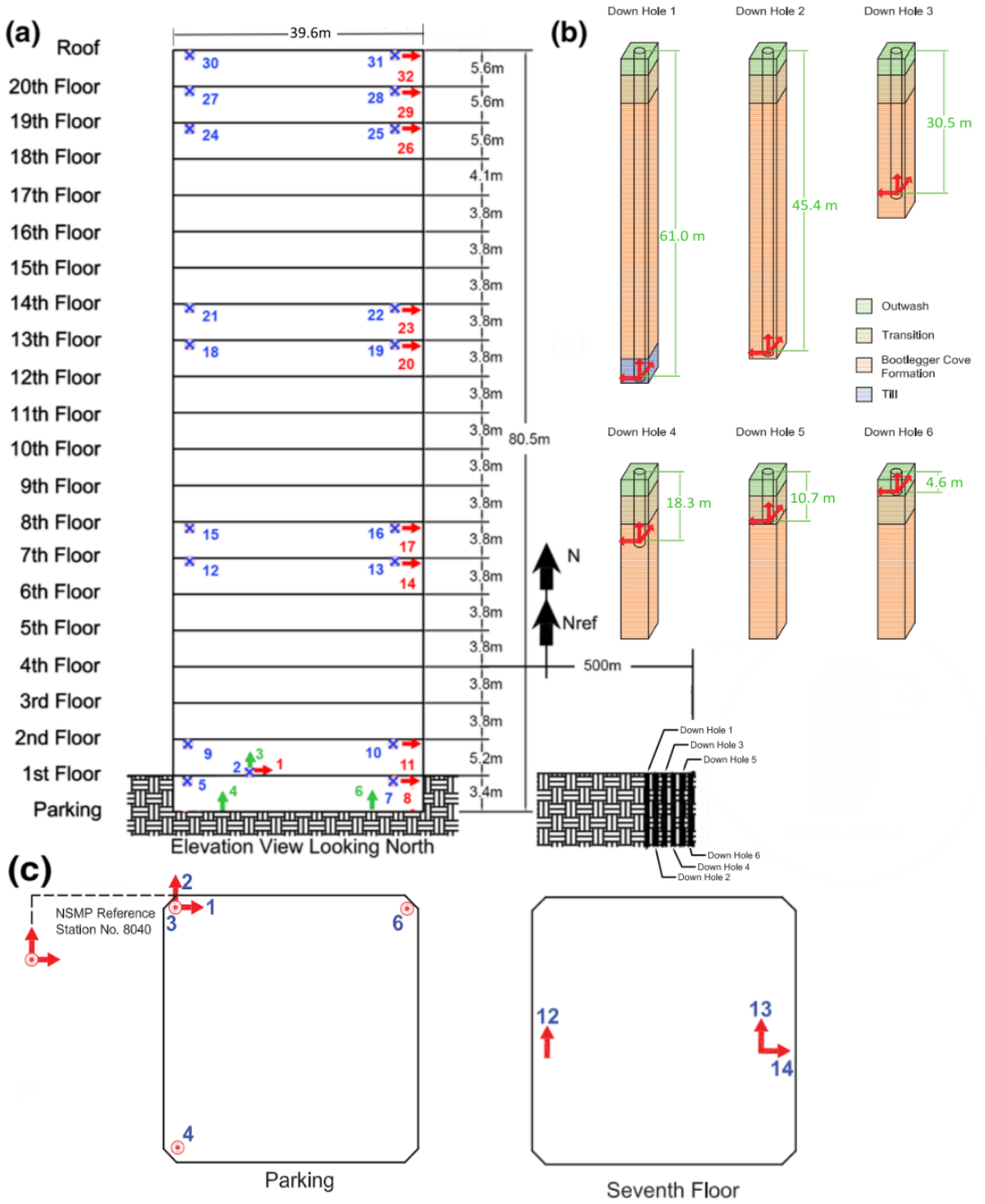

Figure 5.3: Layout of structure array throughout the building (a), site array with the different boreholes (b) and detail of the parking floor and of a typical instrumented floor (c), adapted from [24] and [8].

5.2 Ambient vibrations and optimal placement of sensors

In engineering practice, it is common to extract the most important modal parameters from measured accelerations coming from ambient vibrations. In this section, the modal parameters of the Atwood building were computed. To do so, an adapted version of the MATLAB code also used in Chapter 4 was applied to the extracted accelerations.

As mentioned in Section 5.1, the building is a 20-storey moment resisting frame building. To define the mass matrix needed for the normalization of the modal shapes in the application of the method, it was thus considered that in the structure there was a 170 mm composite slab supported by steel beams and the central concrete core. To have an estimation of the weight of each floor, the exercise sessions from the Course of Structure under Fire taught by Professor Vassart were used, where a similar multi-storey steel MRF building was studied [47]. Considering an earthquake load combination as the one presented in Chapter 4, a total mass per floor of m=1.16 ktons was obtained. Being the structure symmetric in plan, it was considered that the centre of mass CM was coincident with the geometric centre in plan.
In the hypothesis that the mass is homogeneously distributed throughout the plan, the rotational inertia with respect to the centre of mass CM can be computed as [10]:

$$I_{CM} = m\frac{a^2 + b^2}{12} = 302.20 \quad ktons \cdot m^2 \tag{5.1}$$

where m is the total mass of the floor and a and b are the lengths of the two sides of the building's plan. In this specific case $a = b = 39.6\ m$, as the plan is squared. For the formulation of the mass matrix $\mathbf{M}$ every floor was considered to have the same mass.

As previously done by Hoult [24], due to scarcity of real ambient vibrations induced by wind or traffic, six low magnitude earthquakes with $2<M_w<3$ were deemed as equivalent low-amplitude ambient vibrations (Table 5.1).

Event	Event ID	Date (dd/mm/yyyy)	Time (UTC)	Depth (km)	Distance (km)	Magnitude (M_w)
1	20328012	05/11/2018	04:10:14	40.7	24.7	2.1
2	20338975	09/11/2018	16:44:49	13.2	24.8	2.1
3	20347996	11/11/2018	12:32:35	2.9	26.4	2.0
4	20356688	12/11/2018	21:23:55	46.4	45.3	2.1
5	20357049	13/11/2018	13:33:50	33.9	39.8	2.8
6	20357205	13/11/2018	17:22:08	44.8	35.7	2.8

Table 5.1: Low-amplitude earthquake events in close proximity to the Atwood building leading up to the M_w 7.1 event [24].

All the accelerometers presented in Figure 5.3 in the structure were used to this purpose, at all the instrumented floors.

In a classical situation it is likely that there would be less available sensors in the structure as such a complete sensors' layout has an important cost, which is not affordable for the wide majority of building owners.

The Fourier amplitude spectra relative to sensors at the 7^{th} and top floors are plotted in Figure 5.4. The first natural frequencies of the structure can be easily detected from these diagrams in the three directions, in the same manner as previously done.

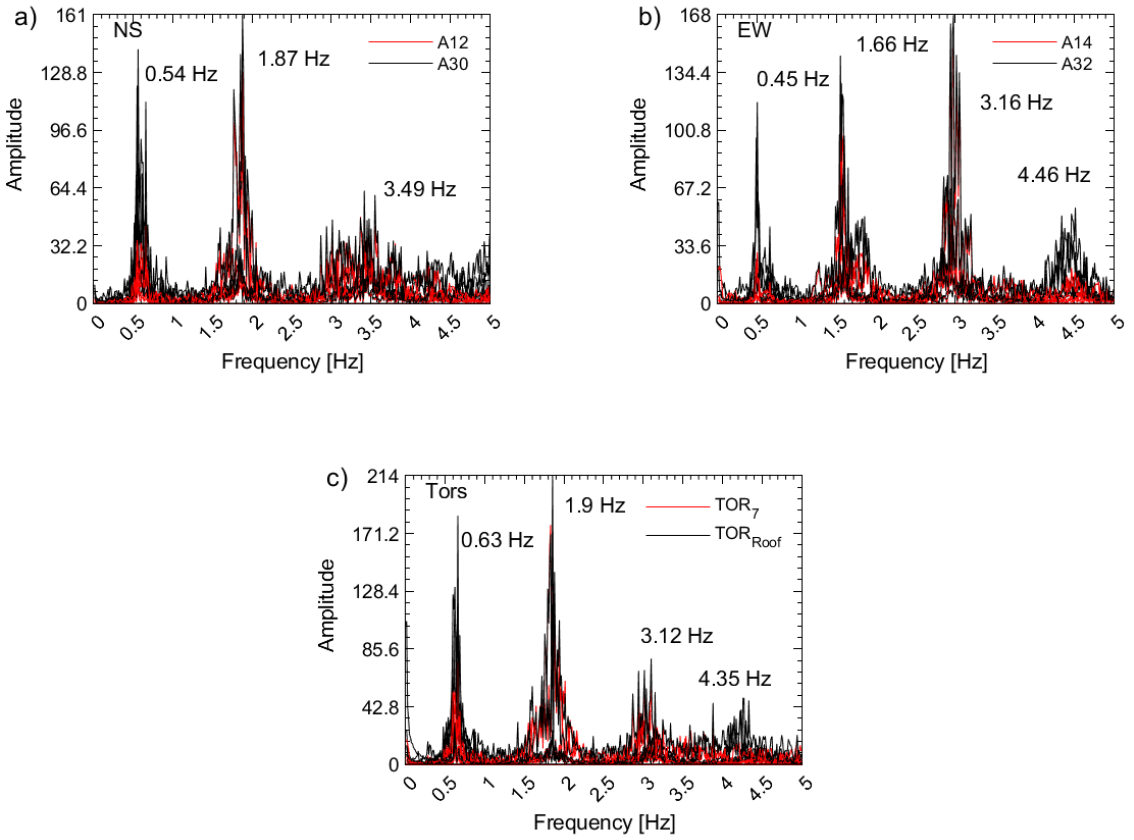

Figure 5.4: Amplitude of the Fourier Transform for the NS (a), EW (b) and Torsional (c) direction.

In the EW direction the natural frequencies are lower, due to higher stiffness along the NS direction, despite geometric symmetry. This increased stiffness is due, according to Yang et al. [50], to braced walls present in four bays along the NS direction.
Since the structure has often been used in the literature for other researches, there is a wide set of papers in which the natural frequencies of the structure have been considered. In Table 5.5.a to 5.5.c, the first three extracted natural frequencies have been then compared in each direction with the ones presented in a paper by Çelebi [6]. It is remarked that in Table (c) of Figure 5.5 for the interval of the third natural frequency there was no given information in the paper.

Mode	FFT [Hz]	Çelebi [Hz]
1	0.54	0.58
2	1.87	1.83
3	3.49	3.5

(a) NS

Mode	FFT [Hz]	Çelebi [Hz]
1	0.45	0.46
2	1.66	1.56
3	3.16	2.92

(b) EW

Mode	FFT [Hz]	Çelebi [Hz]
1	0.63	0.47-0.58
2	1.9	1.5-1.9
3	3.12	-

(c) Torsional

Figure 5.5: Comparison between computed natural frequencies (FFT) and the ones extracted from Çelebi's paper [6].

The same procedure considered in Chapter 4 was applied to this case to compute the modal shapes, resulting in the diagrams presented in blue in Figure 5.11.

With these modal shapes the 3D method was applied to the structure to understand the optimal placement of a certain N_s number of sensors, in the same way as done in the previous chapters.

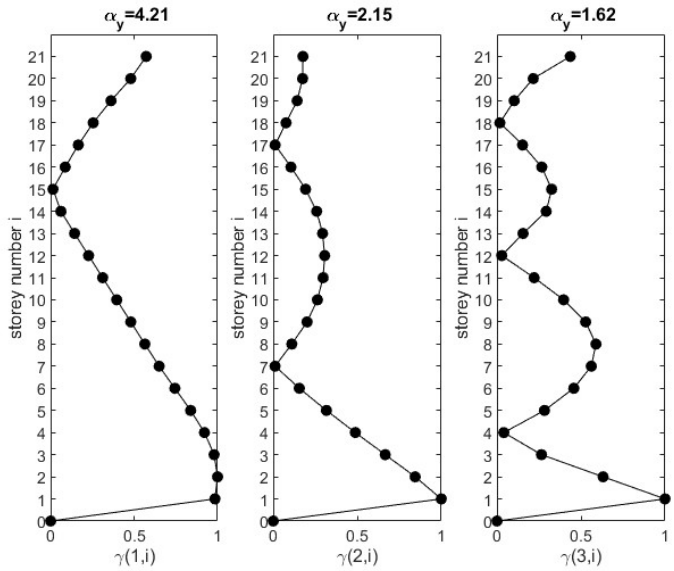

Figure 5.6: Evolution of γ in NS direction in function of N_m modes considered

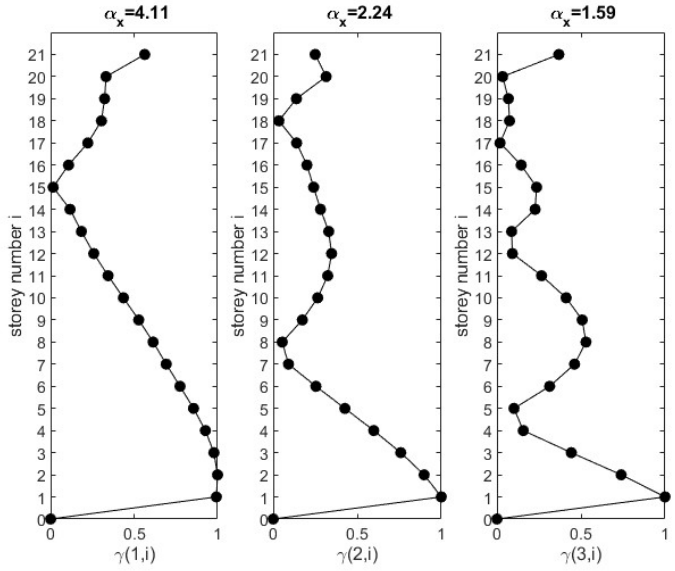

Figure 5.7: Evolution of γ in EW direction in function of N_m modes considered

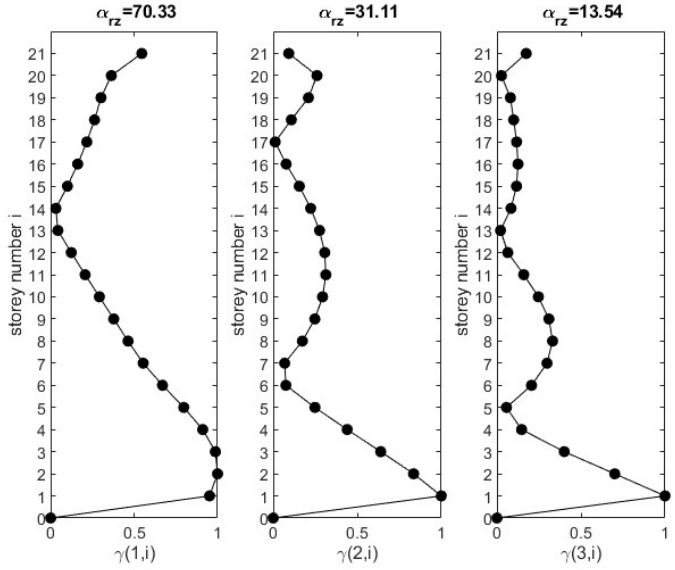

Figure 5.8: Evolution of γ around the vertical axis Z in function of N_m modes considered

As it can be seen also in this case, the optimal placement in the three directions results to be almost coincident, due to the fact that the modal shapes of the torsional modes behave similarly to the ones of the flexural modes.
In the EW direction the γ function presents for the three sensors positioning a different behaviour from the other two directions. Even if in the NS and Torsional direction the third mode is a dominant one, i.e. the local minimums of the γ function coincide with the smaller values of the γ function itself, in the EW direction this is not true. Additionally, in this diagram it is noticed that the number of local

minimums is not coincident with the number of modes considered (3 modes considered but 4 local minimums).
To decide thus an optimal position to place the sensors globally, an intermediate value was found, as seen in Table 5.2. This value was computed by doing an arithmetic average between the three values in the three directions.

N_s	Direction			
	NS	EW	Tor	Global
1	15	15	14	15
2	7-17	8-18	7-17	7-17
3	4-12-18	5-13-between 17 and 20	5-13-20	5-13-19

Table 5.2: Table showing sensor placement in different directions.

The results found are quite similar to the ones in Appendix B related to the numerical model with 20 floors. In effect, in both cases a homogeneous distribution of masses was considered throughout the structure, with the roof weighting as the other floors.

5.3 Validity with a 7.1 M_w event

Once the modal parameters were computed with low magnitude earthquakes, the excitation from a stronger earthquake with a 7.1 M_w whose epicentre was about 15 km from the Atwood Building was considered. The characteristics of this earthquake are shown in Table 5.3.

Parameter	**Value**
Event ID	20419010
Date and Hour	30/11/2018 17:29:29
Modified Mercalli Intensity (MMI)	VII in Anchorage
Hypocentral depth [km]	46.7
Magnitude [M_w]	7.1
PGA [g]	44%
Distance from Atwood Building [km]	14.4

Table 5.3: Details of the earthquake event [45]

Due to its proximity to the city of Anchorage, the event had an important impact on its inhabitants, with 117 people injured and several millions of economic losses [45] [49].
To determine if using ambient vibrations for computing the optimal placement of sensors remains valid also when strong earthquakes excite the structure, the same methodology described in the previous chapter was applied to this scenario.
In doing so, the natural frequencies and respective modal shapes could be extracted also for this case, which would lead to another set of optimal placement of sensors.

The purpose of this investigation is to understand if the placement of sensors found by ambient vibrations is the same when a stronger earthquake strikes the structure. In particular, this question arose because it is known that some modal parameters are amplitude-dependent, meaning they can vary based on the intensity of the earthquake. In Figures 5.9.a to 5.9.c the Amplitude of the Fourier Transform is being plotted for this case, where a reduction of the natural frequency is remarked. This is a well known phenomena in the literature [24] [7], and was explained by Ulusoy et al. [42] as joints and structural interfaces are mobilized more completely, reducing the response frequency and increasing the level of damping. Thus, the building becomes apparently less stiff while exhibiting a greater capacity to dissipate energy.

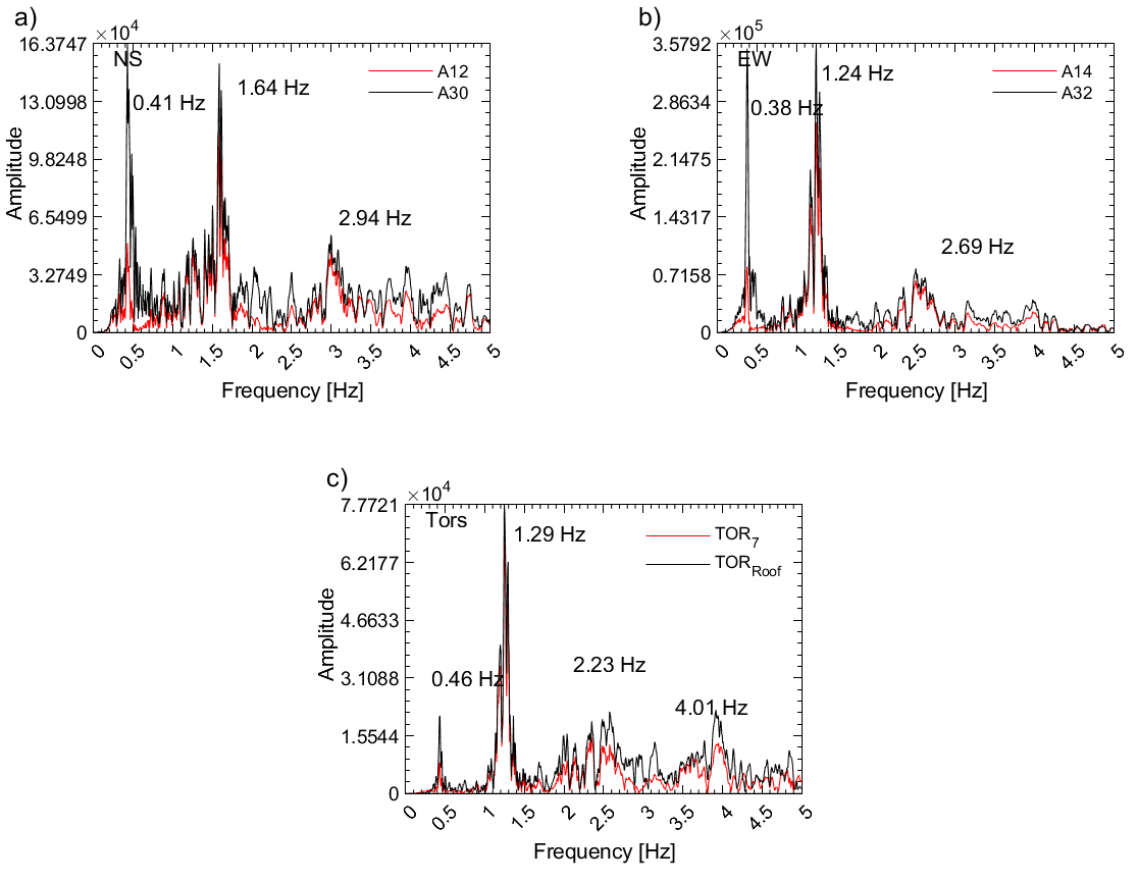

Figure 5.9: Amplitude of the Fourier Transform for the NS (a), EW (b) and Torsional (c) direction.

Mode	$FFT_{ambient}$ [Hz]	FFT_{strong} [Hz]
1	0.54	0.41
2	1.87	1.64
3	3.49	2.94

(a) NS

Mode	$FFT_{ambient}$ [Hz]	FFT_{strong} [Hz]
1	0.45	0.38
2	1.66	1.24
3	3.16	2.69

(b) EW

Mode	$FFT_{ambient}$ [Hz]	FFT_{strong} [Hz]
1	0.63	0.46
2	1.9	1.29
3	3.12	2.23

(c) Torsional

Figure 5.10: Comparison of frequencies computed with the FFT algorithm, considering the cases where the structure is under ambient accelerations ($FFT_{ambient}$) and under a 7.1 M_w earthquake event (FFT_{strong}).

In Tables (a) to (c) of Figure 5.10 it is noted that the natural frequencies are reduced by 10-20% in the case of the 7.1 M_w earthquake with respect to the response of the structure under ambient vibrations.
As in the previous scenario, the natural frequencies are slightly lower in the EW direction, due to the same reason related to higher stiffness in the NS direction.

Despite the big difference in magnitude between the analysed earthquakes, the modal shapes present a similar behaviour, as seen in Figure 5.11. The reduction of the natural frequencies does not then have a relevant impact on modal shapes' observed behaviour. Consequently, the computation of the modal participation factors and thus of the gamma functions led to similar results to the one with ambient vibrations.
Comparing Tables 5.2 and 5.4 it is noticed that the difference between the two cases is of maximum ± 1 floor.
This small difference suggests that the findings on the optimal sensors' layout using ambient vibrations or equivalent ambient vibrations hold also when a stronger earthquake strikes the structure, as long as it still remains in the elastic domain.

Once more, also for this scenario, the optimal placement of sensors in torsion closely aligns with the one in the two NS and EW directions, confirming again the findings of the previous chapters regarding the influence of the torsional modes on the global positioning.

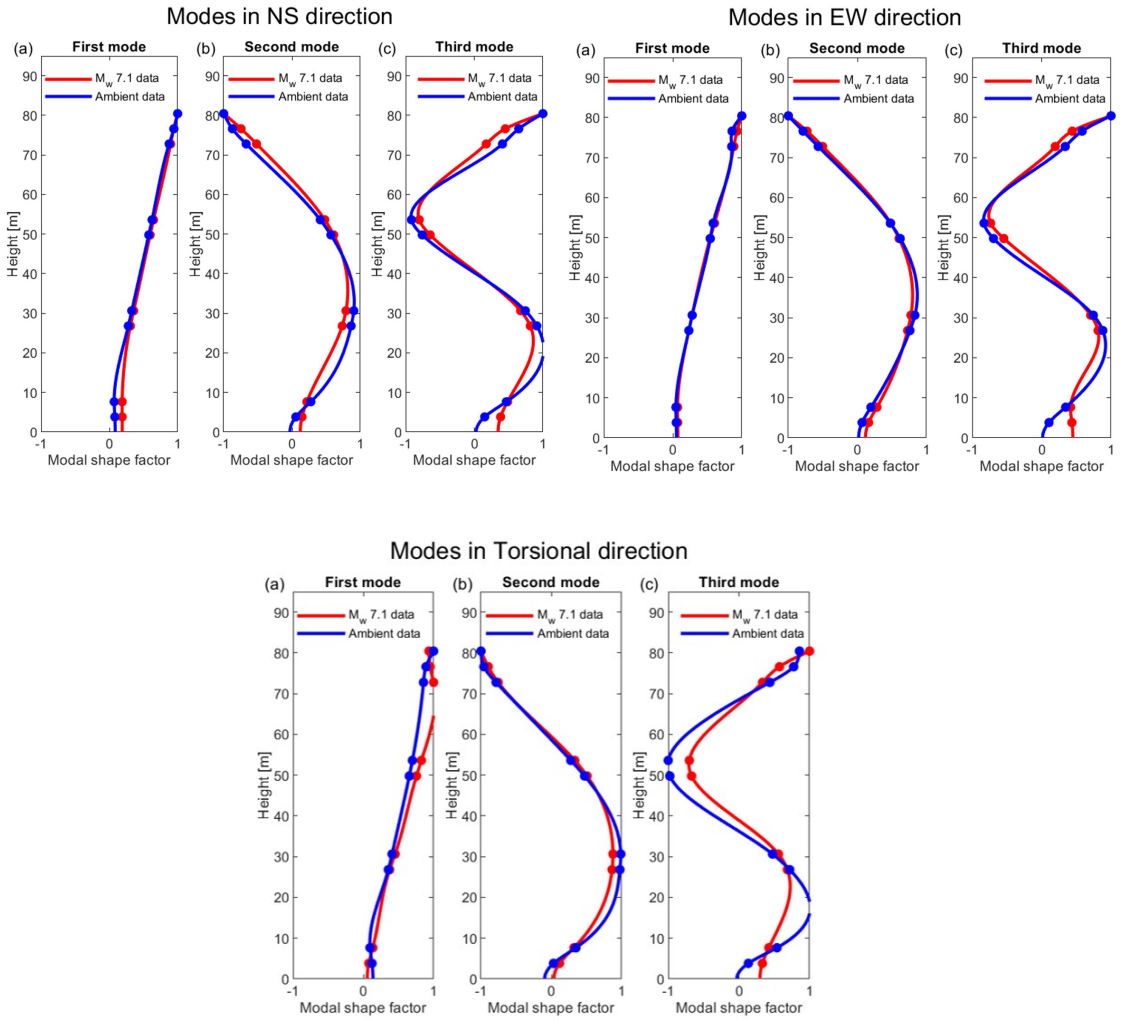

Figure 5.11: For the three directions, first (a), second (b) and third (c) mode, both computed with ambient vibrations (in blue) and with the 7.1 M_w earthquake (in red).

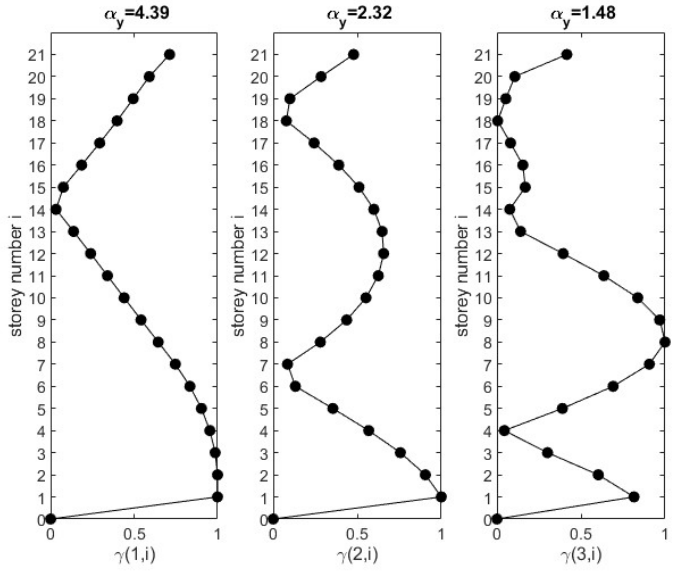

Figure 5.12: Evolution of γ in NS direction in function of N_m modes considered

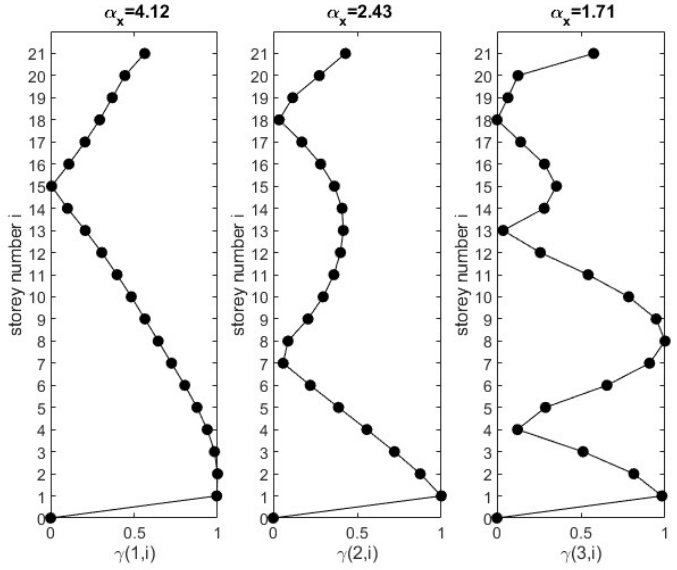

Figure 5.13: Evolution of γ in EW direction in function of N_m modes considered

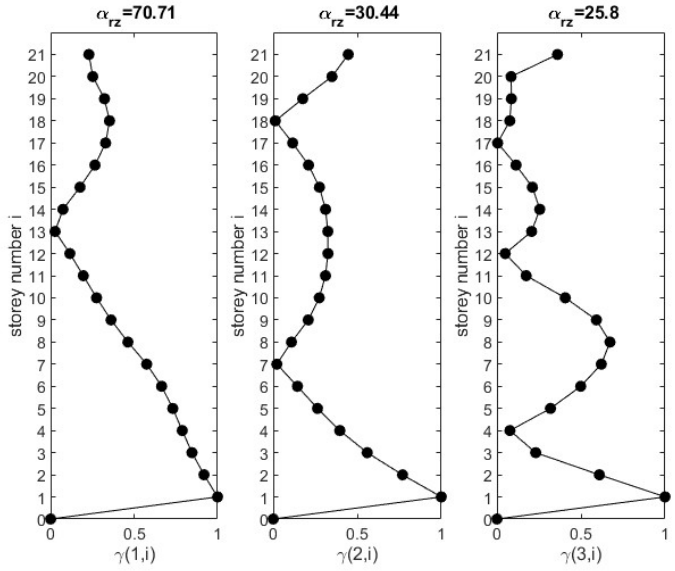

Figure 5.14: Evolution of γ around the vertical axis Z in function of N_m modes considered

N_s	Direction			
	NS	EW	Tor	Global
1	14	15	13	14
2	7-18	7-18	7-18	7-18
3	4-14-18	4-13-18	4-12-17	4-13-18

Table 5.4: Table showing sensor placement in different directions.

Chapter 6

Conclusions and future developments

Seismic Structure Health Monitoring (S^2HM) has increasingly become a utilized technique over recent decades to monitor the behaviour of civil engineering structures under seismic actions worldwide.
Many countries are progressively implementing programs to instrument their strategic structures, enabling near real-time assessment of their condition following seismic events and enhancing design provisions. Consequently, numerous guidelines regarding the placement of sensors have been published.

Despite Australia being located on a stable continental crust, the Australian Government has recently decided to equip some structures in the city of Darwin, the capital of the Northern Territories, with seismic monitoring instruments. Darwin's proximity to a tectonic border makes it susceptible to long-period earthquakes originating from the Banda Sea region.

This thesis aims to determine the optimal placement of accelerometers on selected buildings to best estimate their linear dynamic response, including torsion. Among the various methods found in the literature, the chosen approach involves optimal sensors' placement using a cubic spline function interpolation [28].
This method considers only the building's flexural modes, simplifying the structure to a 2D frame, leaving the influence of torsional modes unaddressed.
Therefore, the initial part of this thesis focuses on expanding the existing method from a 2D model to a 3D model, which also accounts for torsional modes.

Initially, the generalized method was applied to simple 3D frames and demonstrated that torsional modes have modal shapes behaving similarly to the flexural ones, resulting in an analogous optimal placement of sensors.
The analysis were conducted on simple two bays 3D frames, both with homogeneous and eccentric distribution of masses with 5, 10, and 20-stories.

To verify if the conclusions were still valid for a more realistic structure, the method was then applied to a numerical model of a typical Australian building, where special attention had to be paid to accurately model concrete cores. Different earthquakes were used as input in a dynamic time history analysis, and with the use of a Fast Fourier Transform algorithm, the modal parameters were extracted.
This allowed the application of the 3D method using modal shapes computed with different types of excitations acting on the model. In line with the results obtained with simpler frames, the findings indicated a similar optimal placement of sensors determined by both flexural and torsional modes.

Finally, the procedure was applied to an existing instrumented structure, the Atwood building in Anchorage. This structure was deemed suitable for this study as it exhibited torsional behaviour in several seismic events and is one of the most instrumented buildings worldwide.
The method was applied to the structure under small earthquakes, considered as equivalent ambient vibrations, and under a stronger event with a moment magnitude of 7.1.
Despite observing a 10-20% shift in the natural frequencies for the second scenario, the modal shapes showed only slight differences, with the structure remaining elastic even during the stronger event.
As a result, the behaviour of the γ functions remained nearly identical between the two analysed cases, meaning that the optimal sensors' placement derived from ambient vibrations is also applicable when the structure is excited by a higher magnitude event. This case study confirmed the previous observations, with torsional modes converging to a similar optimal placement of sensors as the flexural ones.

The findings from the last three chapters lead to the conclusion that torsion does not significantly influence the layout of the optimal placement of sensors in a structure. Consequently, if the structure is accurately modelled as a 2D frame, the 2D method [28] can be considered sufficient for determining the optimal placement. However, if capturing the torsional behaviour is necessary, two sensors should be placed in the same direction at opposite sides of the instrumented floors. Depending on the purpose of the instrumentation program, the layout of sensors may vary as if the torsional response is required, the focus shifts to optimizing the position of pairs of sensors (or triplets if the orthogonal flexural behaviour is also of interest) from what previously was just optimizing the position of one sensor.

The final part of this work involved creating an easy-to-use tool in Matlab, designed to suggest the optimal sensors' layout based on the characteristics of the structure and the measured accelerations. A step-by-step user guide is provided in Appendix D. This tool aims to assist building owners and authorities in making quick decisions about the optimal placement of sensors to best capture the dynamic behaviour of their structures.

Further Research

Further research on the topic could improve and extend the work of this thesis. The following are the most important areas for future research:

- **Expand 3D Method to include additional DoFs:** The 3D method discussed in this thesis considers three DoFs per floor, without accounting for translation along the Z-axis and rotations around the X and Y axes. Including these additional DoFs could extend the method to a wider range of structures, not limited to the shear building hypothesis.
- **Model additional Australian structures:** Only one of the three provided numerical models of typical Australian structures was studied. Modelling and studying the other two structures could provide a broader understanding of Australian Structures and further validation.
- **Investigate when knowing the torsional behaviour is needed:** A deeper study on the necessity of understanding torsional behaviour in a structure to determine if one sensor per floor is sufficient or if two (or three) are required.
- **Improve Matlab tool:** The Matlab tool discussed in Appendix D is rudimentary, with several simplifications and hypothesis. A more in-depth study and improvement of these simplifications could refine the tool and make it more efficient.

Bibliography

[1] ANSS Technical Integration Committee. *Technical guidelines for the implementation of the Advanced National Seismic System*. Open-File Report. U.S. Geological Survey, 2002.

[2] Australian Earthquake Engineering Society. Round one 2023-24 individual project proposal form, 2023.

[3] K. Beyer, A. Dazio, and M.J.N. Priestley. Inelastic wide-column models for u-shaped reinforced concrete walls. *Journal of Earthquake Engineering*, 12(S1):1–33, 2008.

[4] K. Beyer, A. Dazio, and M.J.N. Priestley. Seismic design of torsionally eccentric buildings with U-shaped RC walls. 2008.

[5] Building Research Institute. BRI strong motion network. https://smo.kenken.go.jp/docs/network/. Accessed: 17.11.2023.

[6] M. Çelebi. Recorded earthquake responses from the integrated seismic monitoring network of the atwood building, anchorage, alaska. *Earthquake Spectra*, 22(4):847–864, 2006.

[7] M. Çelebi. Highlights of a Cursory Study of Behavior of Three Instrumented Buildings during the Mw 7.1 Anchorage, Alaska, Earthquake of 30 November 2018. *Seismological Research Letters*, 91(1):56–65, 10 2019.

[8] Center for Engineering Strong Motion Data (CESMD). Station data for np8040. https://www.strongmotioncenter.org/cgi-bin/CESMD/stationhtml.pl?stationID=NP8040&network=NSMP/, 2024. Accessed: 17.07.2024.

[9] R. Chandramohan, L. Wotherspoon, B. Bradley, M. Nayyerloo, S. Uma, and M. Stephens. Response of instrumented buildings under the 2016 kaikoura earthquake. 2017.

[10] A. K. Chopra. *Dynamics of Structures: Theory and Applications to Earthquake Engineering*. Pearson, 5 edition, 2017.

[11] D. Clark, A. McPherson, and R. Van Dissen. Long-term behaviour of australian stable continental region (scr) faults. *Tectonophysics*, 566-567:1–30, 2012.

[12] Consortium of Organizations for Strong Motion Observation Systems. Guideline for strong motion instrumentation of tall builings. 2016.

[13] C. De Boor. *A practical guide to splines*, volume 27. springer-verlag New York, 1978.

[14] Department of Public Works and Highways. Guidelines and implementing rules on earthquake recoding instrumentation for buildings. 2015.

[15] Engineering ToolBox. Poisson's ratio. https://www.engineeringtoolbox.com/poissons-ratio-d_1224.html/, 2024. Accessed: 28.07.2024.

[16] Eurocode Applied. Eurocode applied: Free online calculation tools for structural design according to eurocodes. https://eurocodeapplied.com/, 2024.

[17] European Committee for Standardization. *Eurocode 0: Basis of Structural Design*. EN 1990:2002. CEN, 2002.

[18] European Committee for Standardization. Eurocode 8: Design of structures for earthquake resistance. 2005.

[19] M. Fawad, M. Salamak, G. Poprawa, K. Koris, M. Jasinski, P. Lazinski, D. Piotrowski, M. Hasnain, and M. Gerges. Automation of structural health monitoring (shm) system of a bridge using bimification approach and bim-based finite element model development. *Scientific Reports*, 13(1):13215, 2023.

[20] Geo Net Service. Structural array data. https://www.geonet.org.nz/data/types/structural_arrays/. Accessed: 17.11.2023.

[21] Geoscience Australia. Earthquake Event: GA2023AQBEZJ. https://earthquakes.ga.gov.au/event/ga2023aqbezj/, 2023. [Accessed: 20.06.2024].

[22] V. R. Gharehbaghi, E. Noroozinejad Farsangi, M. Noori, T. Yang, S. Li, A. Nguyen, C. Málaga-Chuquitaype, P. Gardoni, and S. Mirjalili. A critical review on structural health monitoring: Definitions, methods, and perspectives. *Archives of computational methods in engineering*, pages 1–27, 2021.

[23] R. Hoult. Dataset: A cost-effective method for determining the seismic structural health of high-rise buildings. https://doi.org/10.5281/zenodo.4626317/, 2021.

[24] R. Hoult. A computationally-effective method for rapidly determining the seismic structural response of high-rise buildings with a limited number of sensors. *Bulletin of Earthquake Engineering*, 20(9):4395–4417, 2022.

[25] International Code Council. *The international Building Code*. 2021.

[26] International Conference of Building Officials. *Uniform Building Code*. Whittier, CA : International Conference of Building Officials, 1997.

[27] M. Leonard, D.R. Burbidge, T.I. Allen, D.J. Robinson, A. McPherson, D. Clark, and C.D.N. Collins. The challenges of probabilistic seismic-hazard assessment in stable continental interiors: An australian example. *Bulletin of the Seismological Society of America*, 104(6):3008–3028, 2014.

[28] M. P. Limongelli. Optimal location of sensors for reconstruction of seismic responses through spline function interpolation. *Earthquake engineering & structural dynamics*, 32(7):1055–1074, 2003.

[29] M. P. Limongelli and M. Çelebi. *Seismic structural health monitoring: from theory to successful applications*. Springer, 2019.

[30] Los Angeles Tall Buildings Structural Design Council. *An Alternative Procedure For Seismic Analysis And Design Of Tall Buildings*. 2023.

[31] S.J. Menegon, H.H. Tsang, E. Lumantarna, N.T.K. Lam, J.L. Wilson, and E.F. Gad. Framework for seismic vulnerability assessment of reinforced concrete buildings in australia. *Australian Journal of Structural Engineering*, 20(2):143–158, 2019.

[32] E. A Okal and D. Reymond. The mechanism of great banda sea earthquake of 1 february 1938: applying the method of preliminary determination of focal mechanism to a historical event. *Earth and Planetary Science Letters*, 216(1-2):1–15, 2003.

[33] J. Pacheco de Almeida. Course of earthquake engineering at UCLouvain, 2023.

[34] J.-M. Reynouard and M. N. Fardis. "shear wall structures". *Laboratòrio Nacional de Engenharia Civil, Lisboa, Portugal.*, (Thematic Report No. 5), 2001.

[35] S. M. Schulte and W. D. Mooney. An updated global earthquake catalogue for stable continental regions: reassessing the correlation with ancient rifts. *Geophysical Journal International*, 161(3):707–721, 2005.

[36] Seismosoft. *SeismoStruct User Manual*. Seismosoft, Pavia, Italy, 2024.

[37] D. A Skolnik and J. W. Wallace. Critical assessment of interstory drift measurements. *Journal of structural engineering*, 136(12):1574–1584, 2010.

[38] Standards Australia/Standards New Zealand. AS/NZS 1170.0:2002 Structural Design Actions - General Principles. "https://ia803209.us.archive.org/28/items/as-nzs.1170.0.2002/as-nzs.1170.0.2002.pdf/", 2002. Accessed: 30.06.2024.

[39] Standards New Zealand. NZS 1170.5:2004 - structural design actions, part 5: Earthquake actions - new zealand. Wellington: Standards New Zealand, 2004.

[40] Y. Tan and L. Zhang. Computational methodologies for optimal sensor placement in structural health monitoring: A review. *Structural Health Monitoring*, 19(4):1287–1308, 2020.

[41] T. Terwagne, J. Pacheco De Almeida, and R. Hoult. Optimising the placement of a minimum number of sensors for seismic health monitoring of mid-and high-rise structures. 2023.

[42] H.S. Ulusoy, M. Q Feng, and P. J. Fanning. System identification of a building from multiple seismic records. *Earthquake Engineering & Structural Dynamics*, 40(6):661–674, 2011.

[43] S.R. Uma, A. King, J. Cousins, and K. Gledhill. The geonet building instrumentation programme. *Bulletin of the New Zealand Society for Earthquake Engineering*, 44(1):53–63, 2011.

[44] U.S.G.S. This dynamic planet: World map of volcanoes, earthquakes, impact craters, and plate tectonics. https://pubs.usgs.gov/imap/2800/, 2016.

[45] U.S.G.S. M 7.1 - 13km n of anchorage, alaska. https://earthquake.usgs.gov/earthquakes/eventpage/ak018fcnsk91/executive/, 2018. Accessed: 17.07.2024.

[46] U.S.G.S. Seismic hazard map of the anchorage, alaska, area. https://pubs.usgs.gov/sim/3064/, 2024. Accessed: 18.07.2024.

[47] O. Vassart. Course of structures under fire conditions at UCLouvain, 2023.

[48] W. Wen and E. Kalkan. System Identification Based on Deconvolution and Cross Correlation: An Application to a 20-Story Instrumented Building in Anchorage, Alaska. *Bulletin of the Seismological Society of America*, 107(2):718–740, 2017.

[49] Wikipedia contributors. 2018 anchorage earthquake. https://en.wikipedia.org/wiki/2018_Anchorage_earthquake/, 2018. Accessed: 17-07.2024.

[50] Z. Yang, U. Dutta, M. Celebi, H. Liu, N. Biswas, T. Kono, and H. Benz. Strong-motion instrumentation and structural response of atwood building in downtown anchorage, alaska. In *13th world conference on earthquake engineering*, 2004.

Appendix A

Cubic spline function

The method studied in this thesis is based on the use of a set of cubic spline interpolation functions to extract unknown accelerations by interpolating the measured accelerations using them as nodes of the spline.

In this Appendix the Cubic Spline Function is presented, similarly to what was done in the original article from Professor Limongelli [28].

A spline is a piecewise polynomial function, composed of polynomials defined within subintervals, which are linked together under certain smoothness conditions. Given a function $f(z)$ defined on the interval $[a, b]$ and the values of $f(z)$ at n points (knots) $z_1, z_2, \ldots, z_n$ with $a = z_0 < z_1 < z_2 < \cdots < z_n < z_{n+1} = b$, a cubic spline $s(z)$ interpolant to $f(z)$ consists of $n + 1$ cubic polynomials $s_i(z)$, each defined in one subinterval $[z_i, z_{i+1}]$.

$$s_i(z) = c_{0,i} + c_{1,i}(z - z_i) + c_{2,i}(z - z_i)^2 + c_{3,i}(z - z_i)^3, \quad z \in [z_i, z_{i+1}], \quad i = 0, \ldots, n \tag{A.1}$$

To ensure a continuous and smooth approximating function, $s(z)$ is assumed to be twice continuously differentiable, which means it has a continuous slope and continuous curvature. These continuity conditions imply:

$$\begin{aligned} s_{i-1}(z_i) &= s_i(z_i), \\ s'_{i-1}(z_i) &= s'_i(z_i), \\ s''_{i-1}(z_i) &= s''_i(z_i), \end{aligned} \tag{A.2}$$

where s'_i and s''_i are the first and second derivatives of $s_i(z)$ with respect to z. At each internal knot, the polynomial piece $s_i(z)$ fits the value $f(z_i) = f_i$:

$$s_i(z_i) = f(z_i) = f_i, \quad i = 1, \ldots, n \tag{A.3}$$

For each of the $n+1$ polynomials, four unknown coefficients $(c_{0,i}, c_{1,i}, c_{2,i}, c_{3,i})$ must be found, leading to a total of $4(n+1)$ equations for a unique solution. The continuity (A.2) and interpolation (A.3) conditions provide $4n$ equations. Four additional constraints are then found with the boundary conditions, defined at $z = a$ and $z = b$.

The unknown coefficients for the i-th subinterval are:

$$
\begin{aligned}
c_{0,i} &= f_i, \\
c_{1,i} &= \frac{f_{i+1} - f_i}{z_{i+1} - z_i} - \frac{(2s''_i + s''_{i+1})(z_{i+1} - z_i)}{6}, \\
c_{2,i} &= \frac{s''_i}{2}, \\
c_{3,i} &= \frac{s''_{i+1} - s''_i}{6(z_{i+1} - z_i)}
\end{aligned}
\tag{A.4}
$$

Appendix B

Functions γ in Chapter 3

In this Appendix the γ functions that were not directly plotted in Chapter 3 are presented. It was decided to place them here in order to make the reading of the report more fluent, without overfilling it with too many diagrams.
The whole chapter 3 was developed around a numerical model of 10 floors. Nevertheless, as specified in the report, the same reasoning was applied to also the numerical models of 5 and 20 floors, coherently with what was done in [28]. It is remarked that, for these two structures, all the reasoning explained in the report holds, just the number of floors changes. In the following are presented the γ functions relative to these cases both for a symmetrical and non-symmetrical mass disposition, in the three X,Y and RZ directions.
At first, the results relative to the 5-storey frame are presented. Next, the diagrams of the 20-storey frame are displayed.

B.1 Symmetric disposition of masses

B.1.1 5 floors

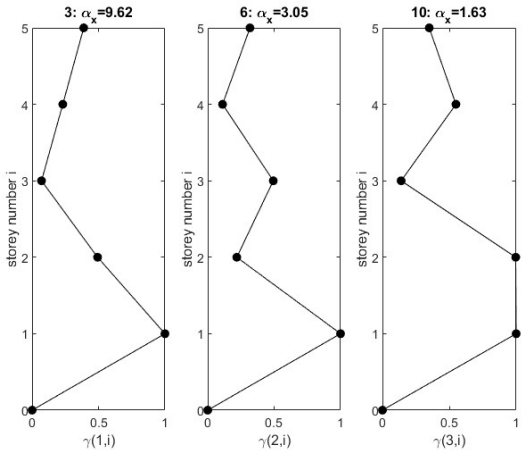

Figure B.1: Evolution of γ along X in function of N_m modes considered with a symmetric mass distribution, 5 floors.

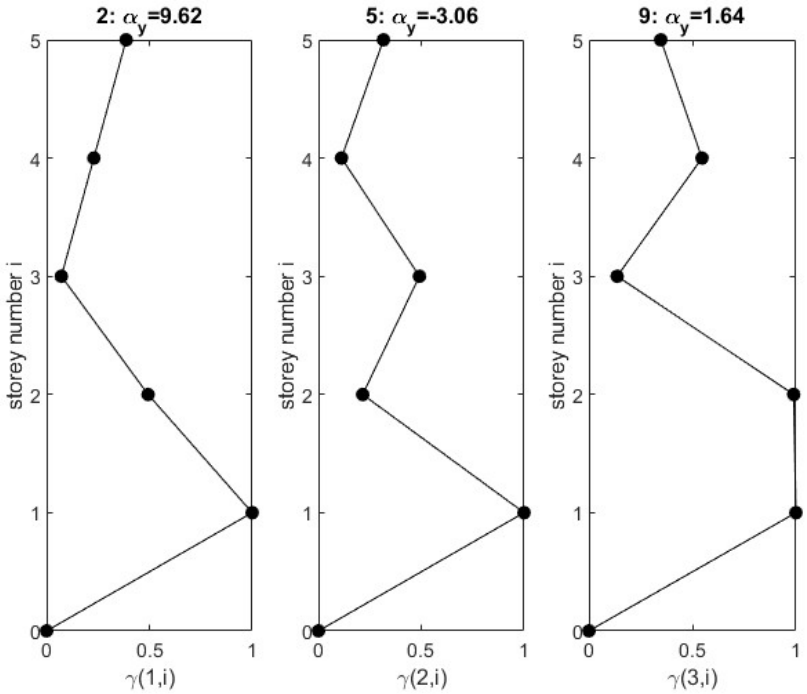

Figure B.2: Evolution of γ along Y in function of N_m modes considered with a symmetric mass distribution, 5 floors.

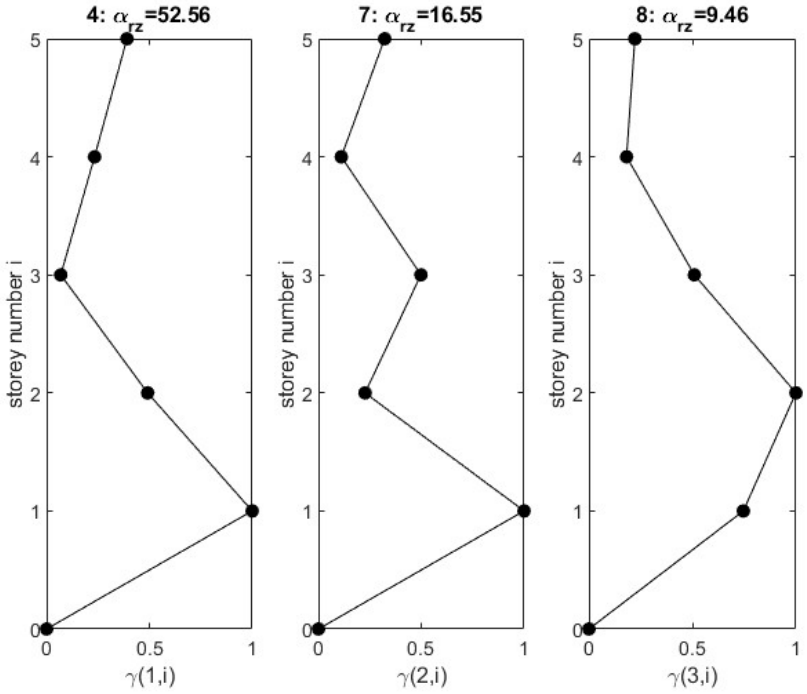

Figure B.3: Evolution of γ around Z in function of N_m modes considered with a symmetric mass distribution, 5 floors.

B.1.1.1 20 floors

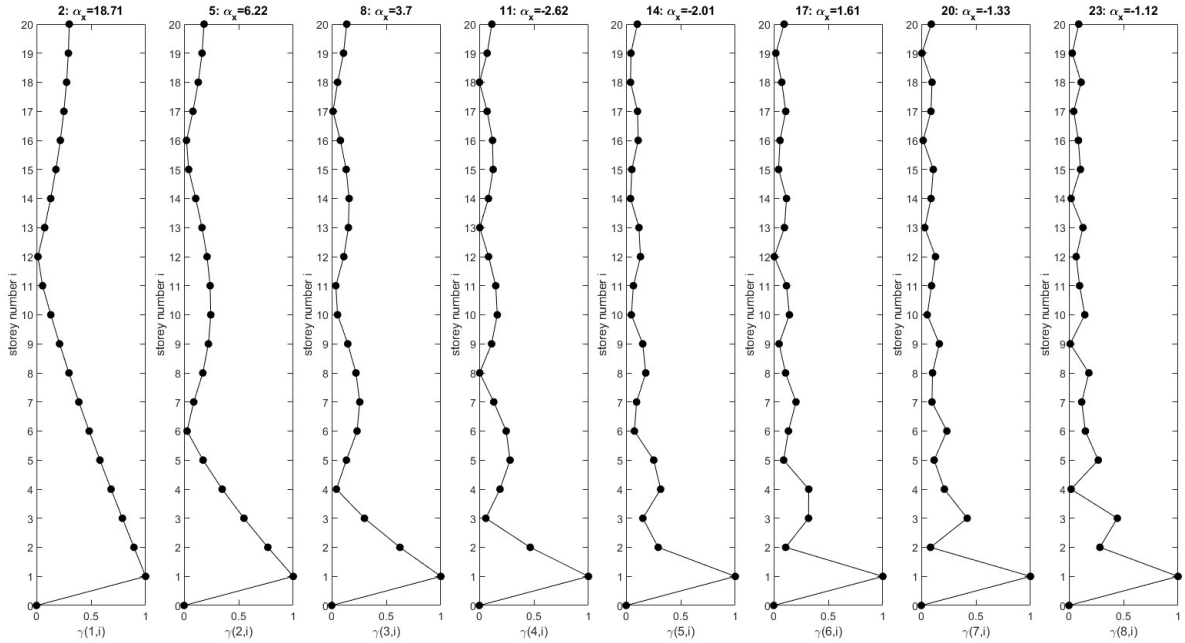

Figure B.4: Evolution of γ along X in function of N_m modes considered with a symmetric mass distribution, 20 floors.

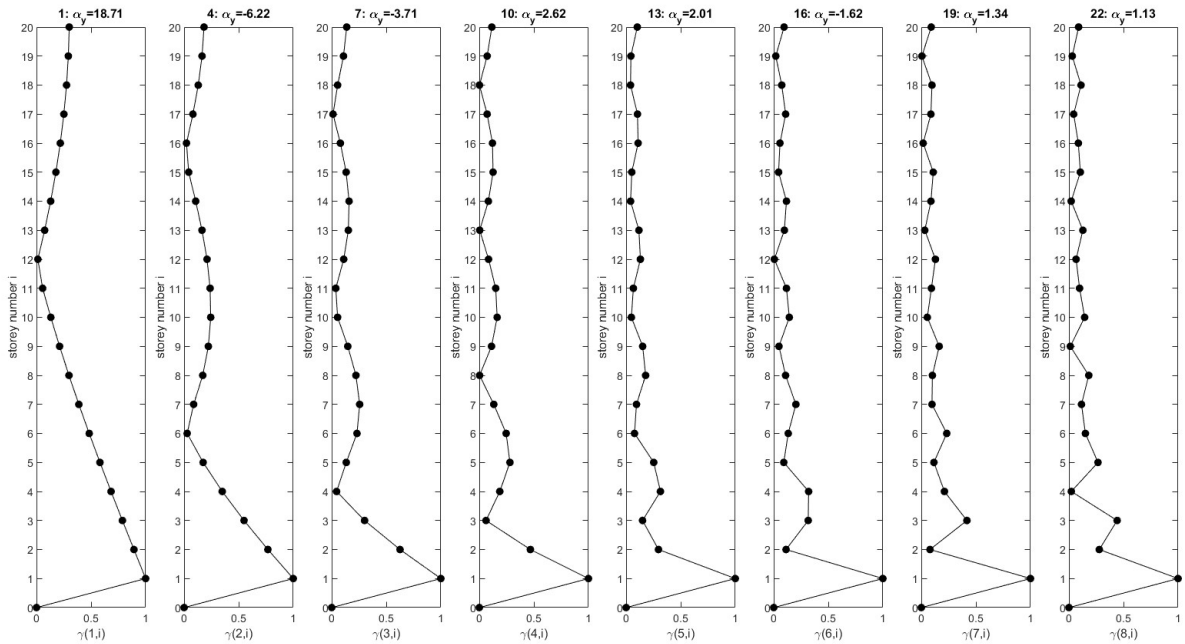

Figure B.5: Evolution of γ along Y in function of N_m modes considered with a symmetric mass distribution, 20 floors.

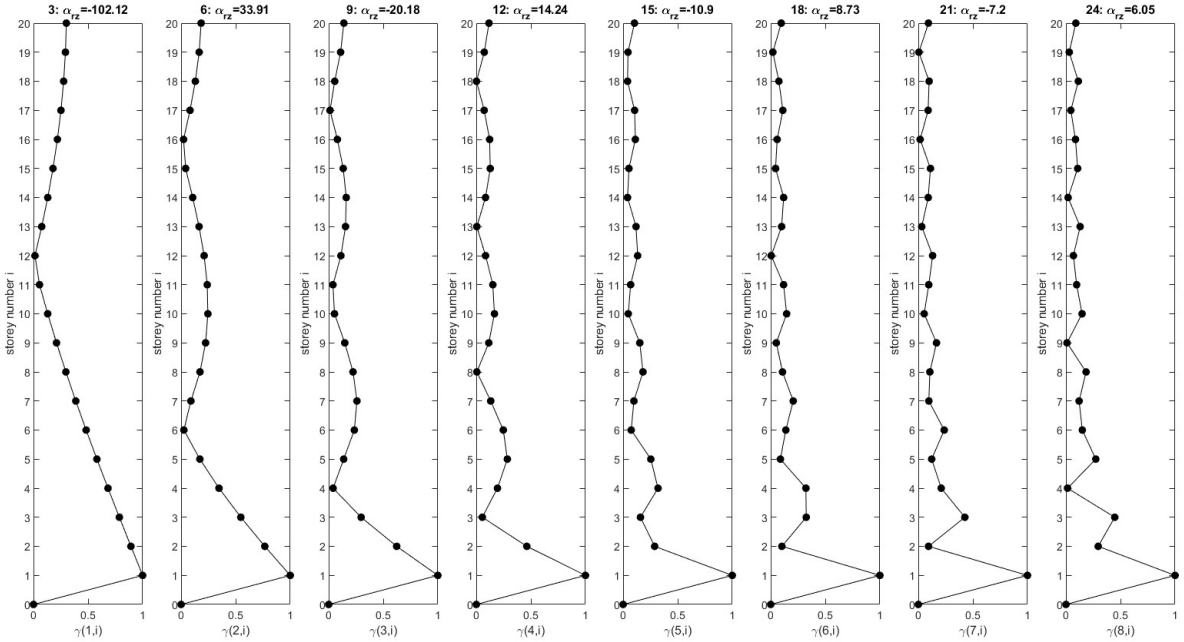

Figure B.6: Evolution of γ around Z in function of N_m modes considered with a symmetric mass distribution, 20 floors.

B.2 Non-symmetric mass distribution

B.2.1 5 floors

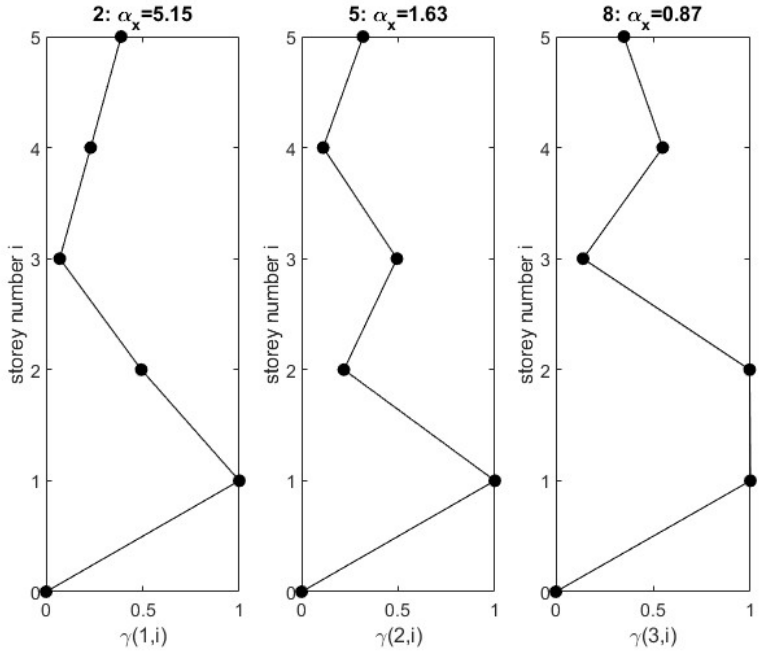

Figure B.7: Evolution of γ along X in function of N_m modes considered with a non-symmetric mass distribution, 5 floors .

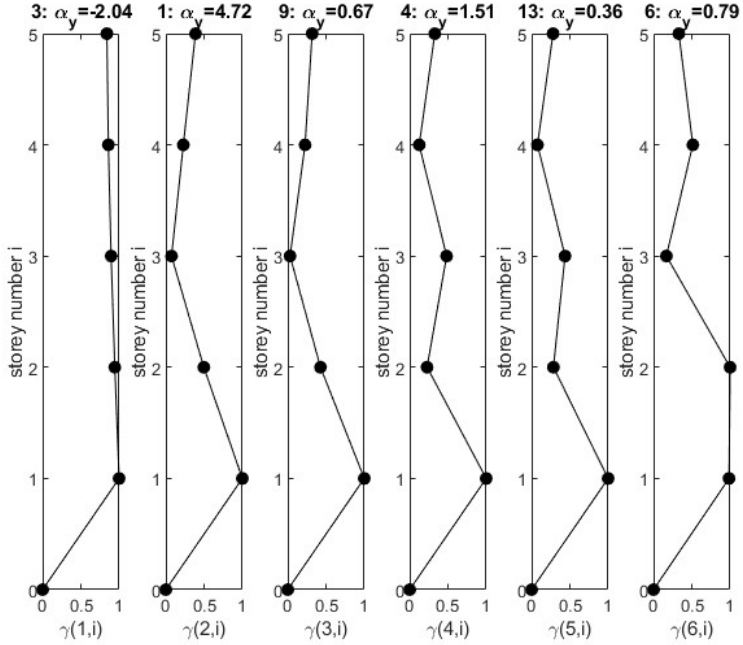

Figure B.8: Evolution of γ along Y in function of N_m modes considered with a non-symmetric mass distribution, 5 floors.

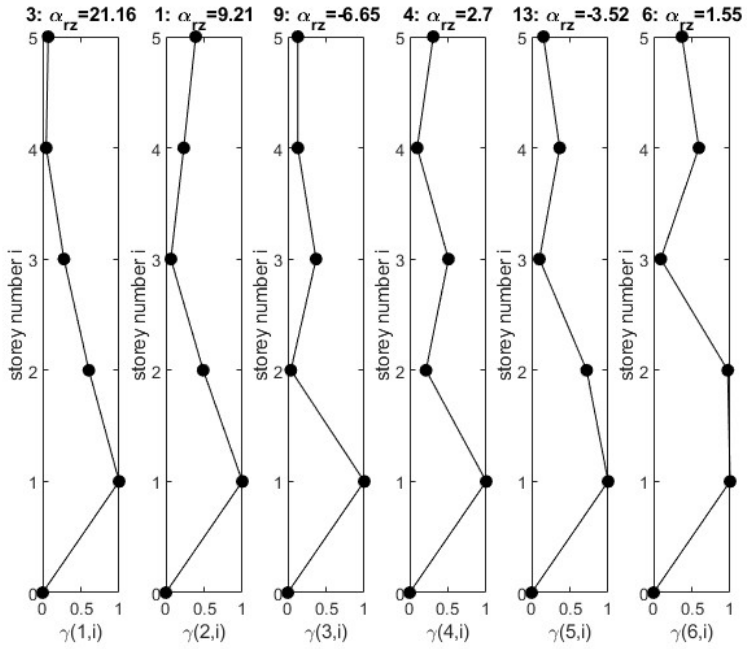

Figure B.9: Evolution of γ around Z in function of N_m modes considered with a non-symmetric mass distribution, 5 floors.

N_s	Direction		
	X	Y	RZ
1	3	3	3
2	2-4	2-4	2-4

Table B.1: Optimal placement of sensors for a 5-storey structure.

B.2.2 20 floors

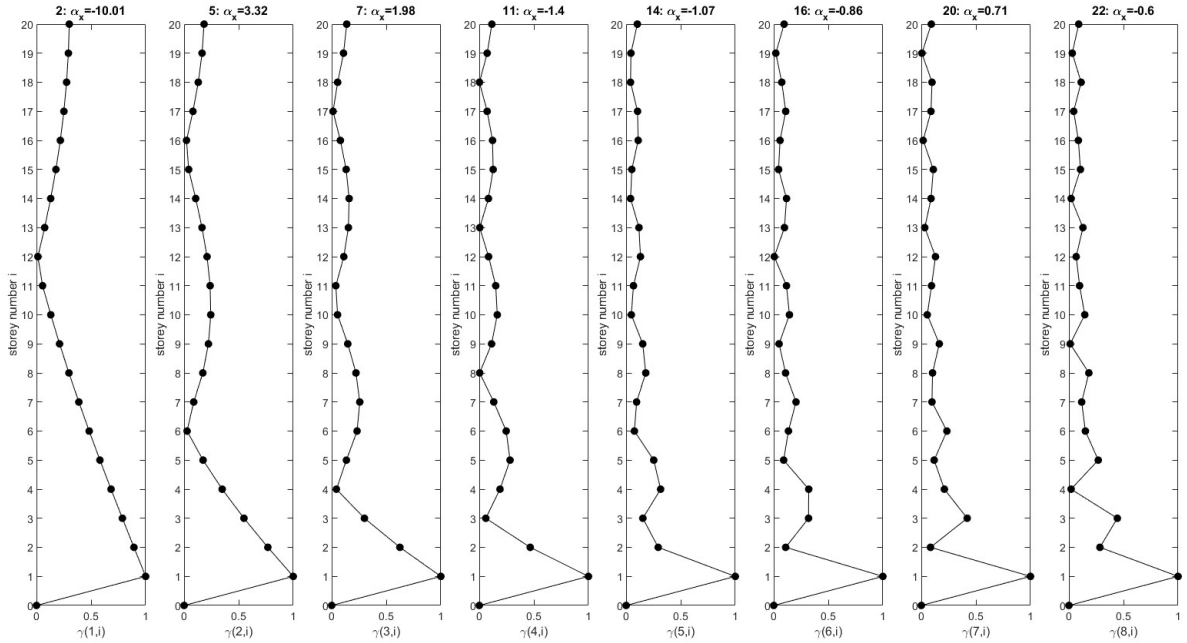

Figure B.10: Evolution of γ along X in function of N_m modes considered with a non-symmetric mass distribution, 20 floors.

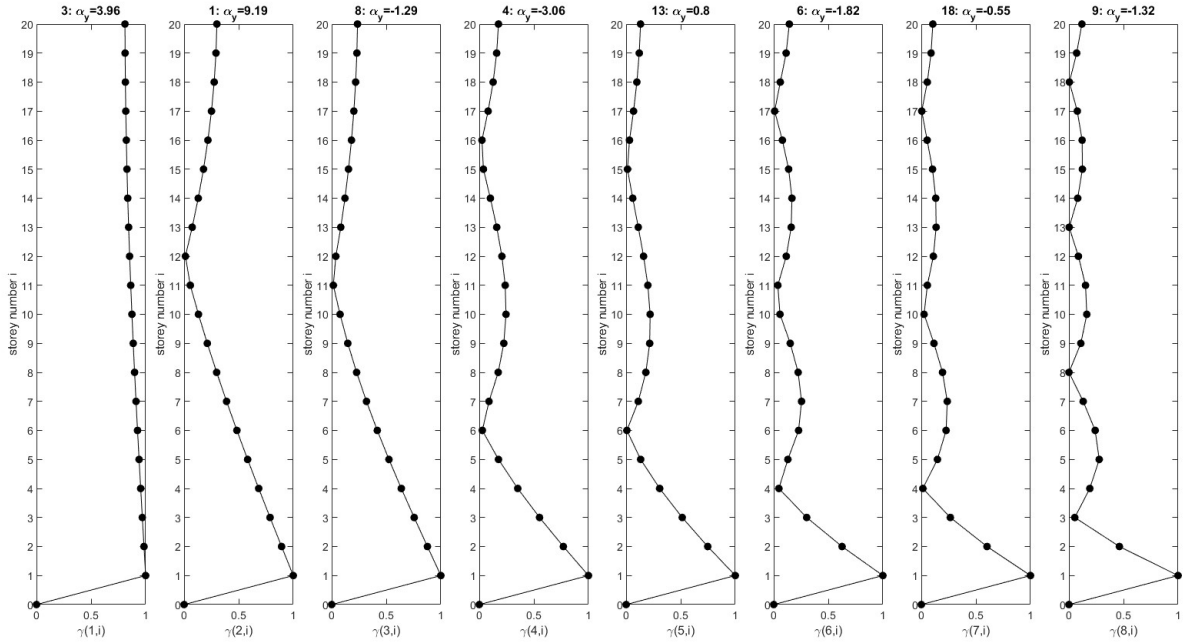

Figure B.11: Evolution of γ along Y in function of N_m modes considered with a non-symmetric mass distribution, 20 floors(γ 1-8).

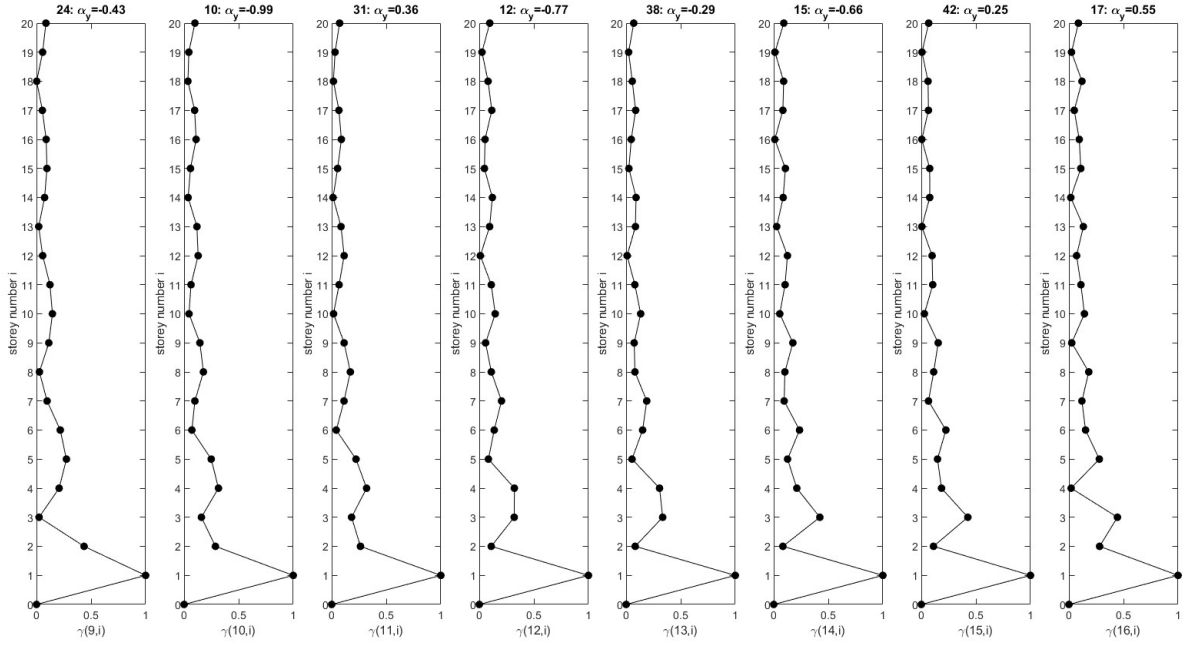

Figure B.12: Evolution of γ along Y in function of N_m modes considered with a non-symmetric mass distribution, 20 floors(γ 9-16).

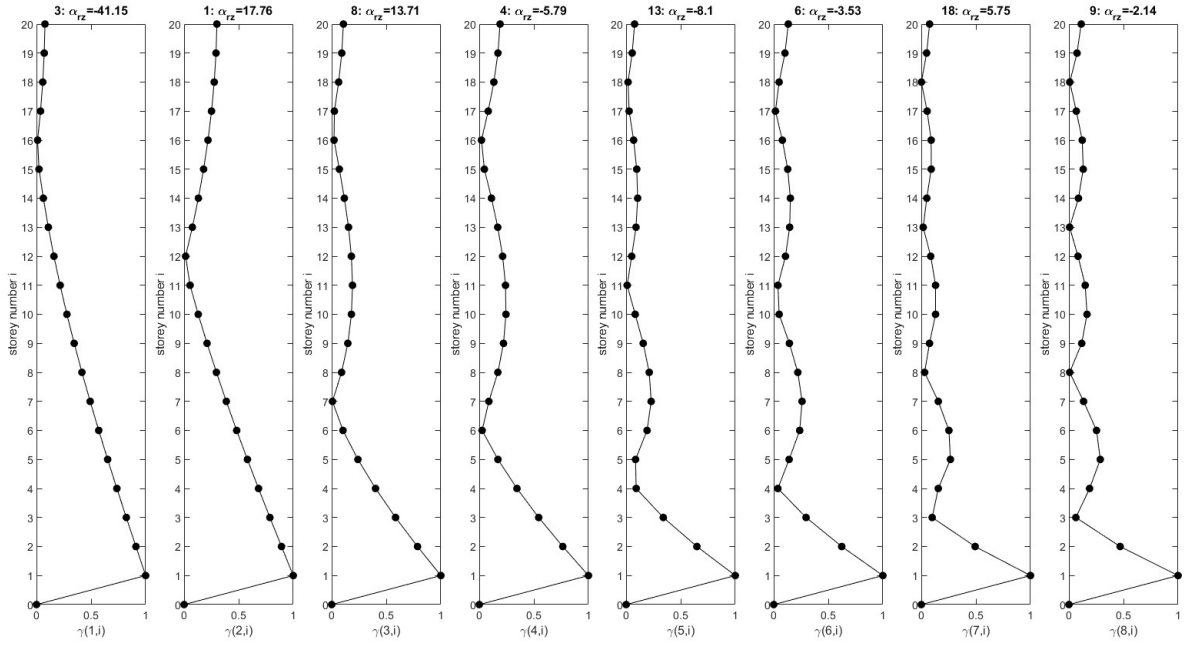

Figure B.13: Evolution of γ around Z in function of N_m modes considered with a non-symmetric mass distribution, 20 floors(γ 1-8).

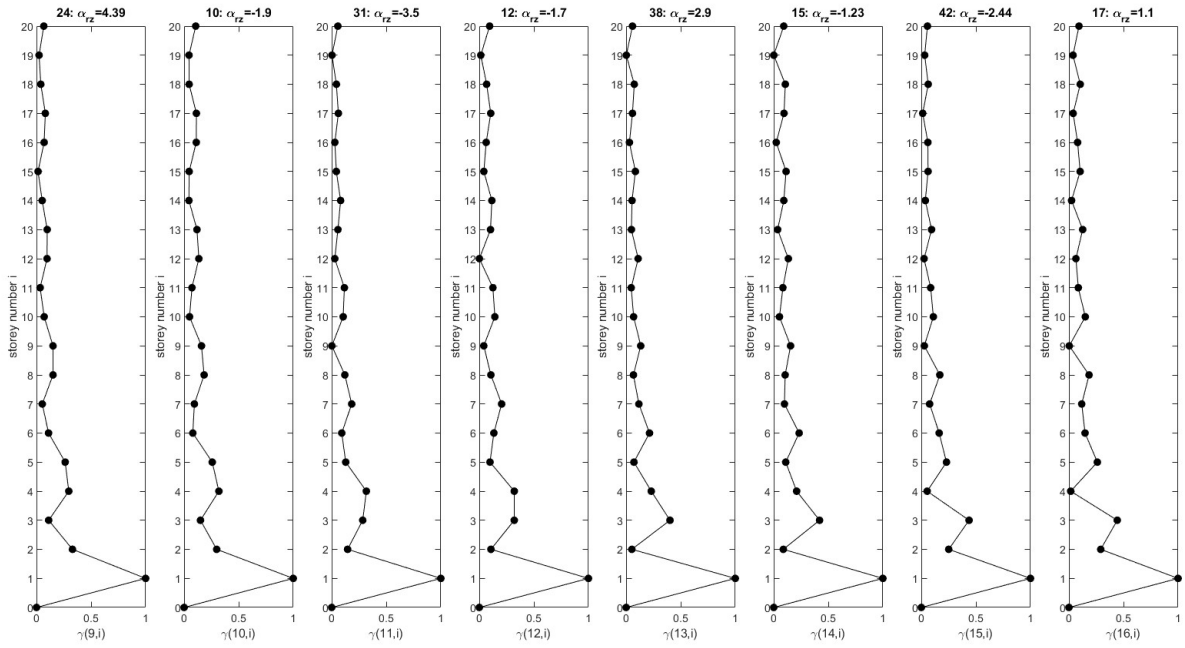

Figure B.14: Evolution of γ around Z in function of N_m modes considered with a non-symmetric mass distribution, 20 floors(γ 9-16).

N_s	Direction		
	X	Y	RZ
1	12	12	12
2	6-16	6-16	6-16
3	4-11-17	4-11-17	4-11-17
4	3-8-13-18	3-8-13-18	3-8-13-18

Table B.2: Optimal placement of sensors for a 20-storey structure.

It is observed that for the dominant modes, the first two and the first four respectively for the 5-storey and the 20-storey structure, the optimal placement of sensors coincides with the one of the paper where the 2D method was introduced [28], and thus the conclusions at the end of chapter 3 hold also for these two other structures. Nevertheless, one slight difference is remarked. In particular, for the 20-storey structure it is noticed that in the 2D frame the optimal position for one sensor was 13, while in the current case it is 12. A possible explanation for this difference is that, as stated in the report, the numerical model was simplified by assigning equal masses to each floor, including the roof. In contrast, the 2D frame had slightly lower masses at the roof nodes. This difference was not remarked in the 5-storey and 10-storey models, probably because the reduction in mass was not as influent to change the optimal positioning as it was in the 20-storey structure.

Appendix C

Other provided plans of Australian Structures

In this Appendix the three typical Australian plans that were provided by Dr. Scott Menegon are entirely presented. The first one, in Figure C.1 and C.2 was used in Chapter 4 for creating a numerical model of a typical Australian Structure to be studied. The other two plans, on the other hand, have not been used in the current thesis. They could be however useful material for further research and to have an even wider knowledge on Australian Structures behaviour. They could be modelled in a FE software as done in Chapter 4, and compared with the already modelled one.

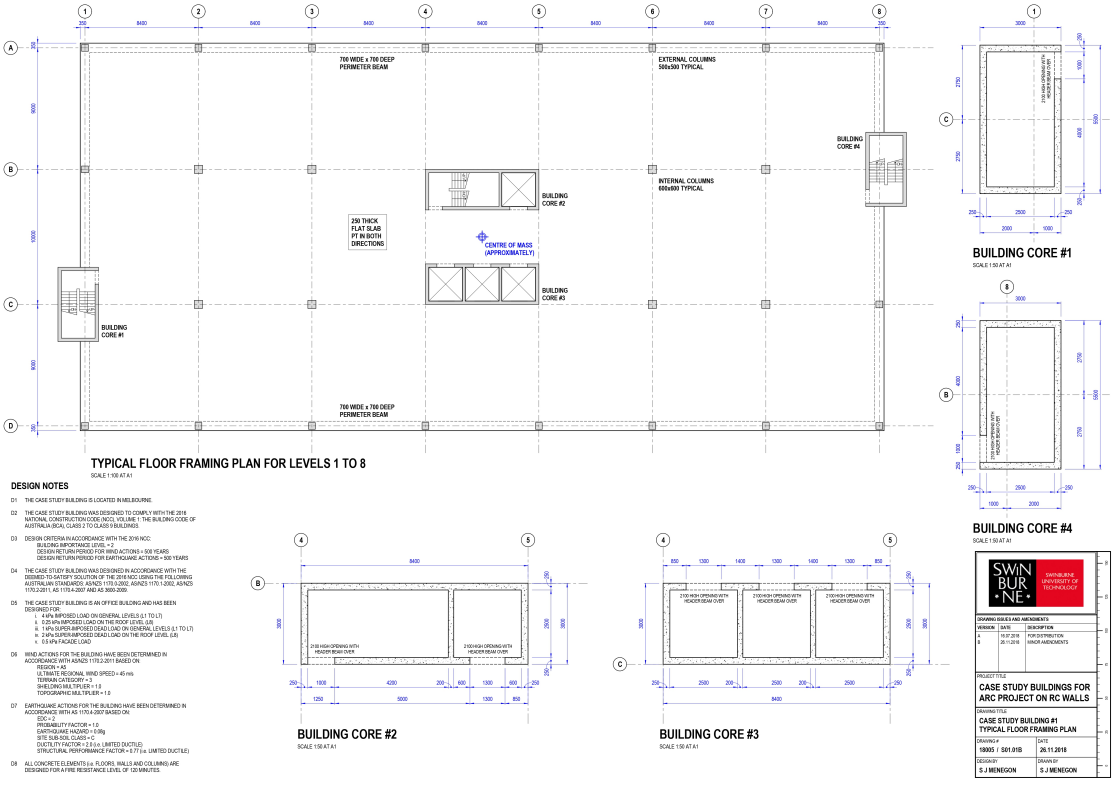

Figure C.1: Plan 1-front.

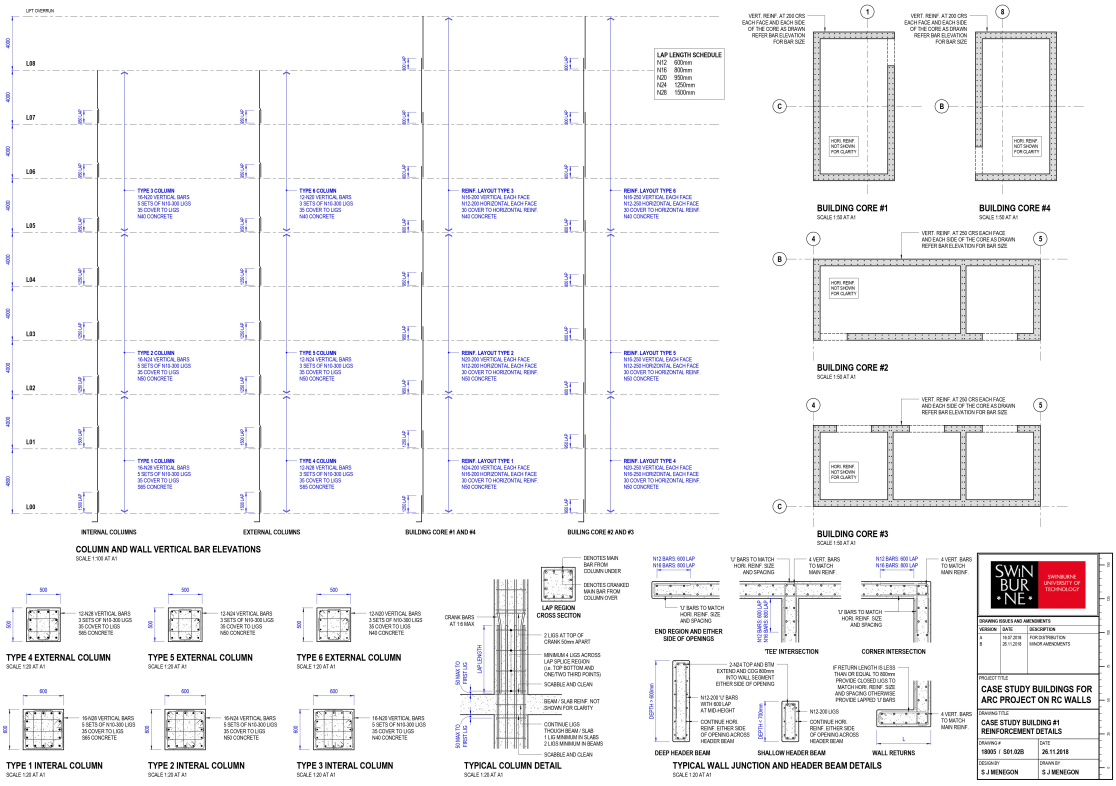

Figure C.2: Plan 1-back.

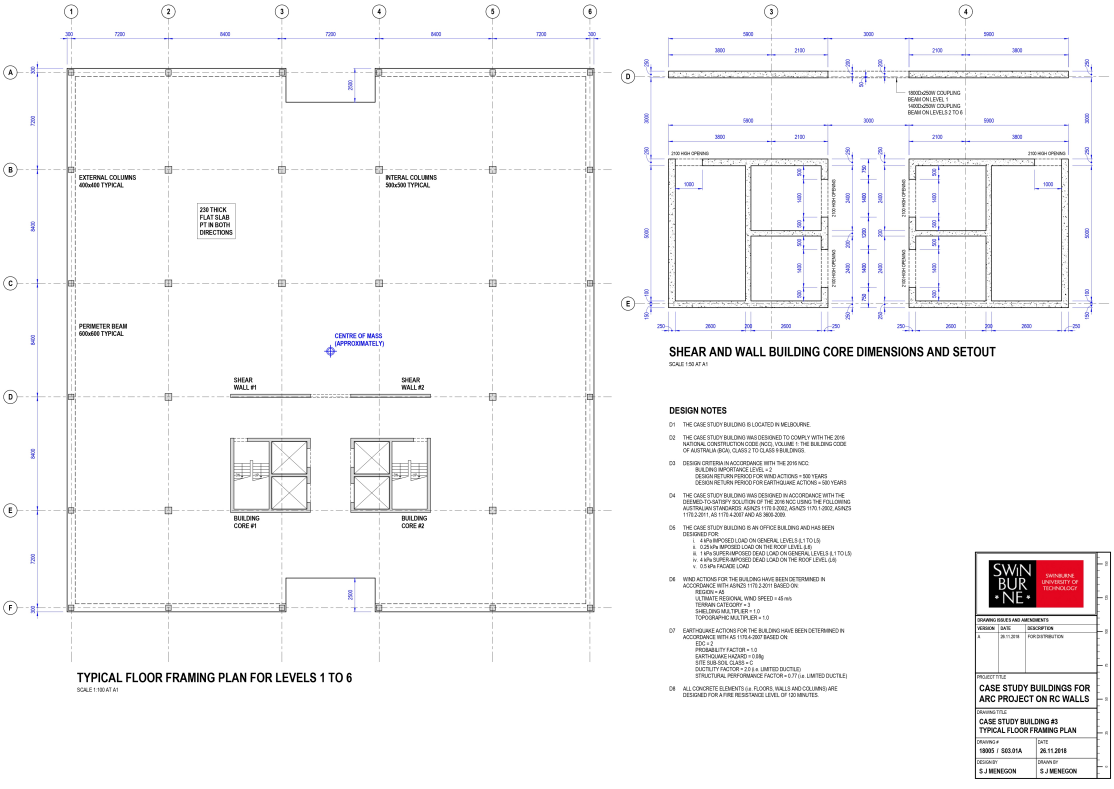

Figure C.3: Plan 2-front.

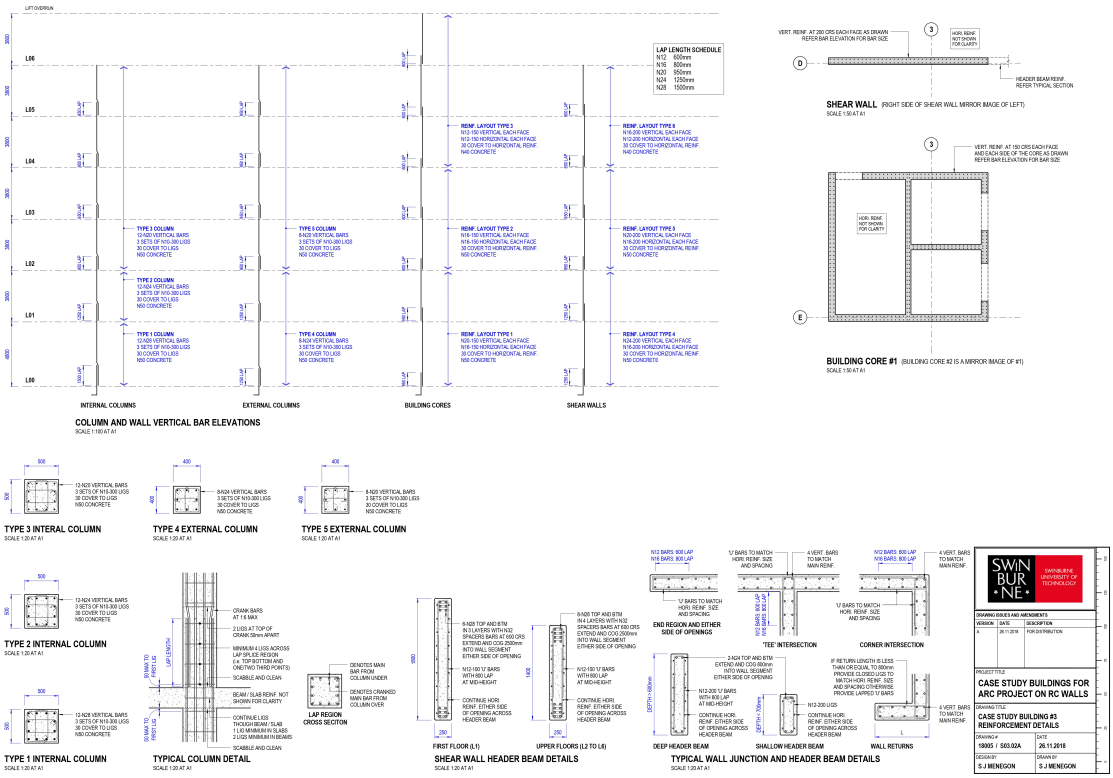

Figure C.4: Plan 2-back.

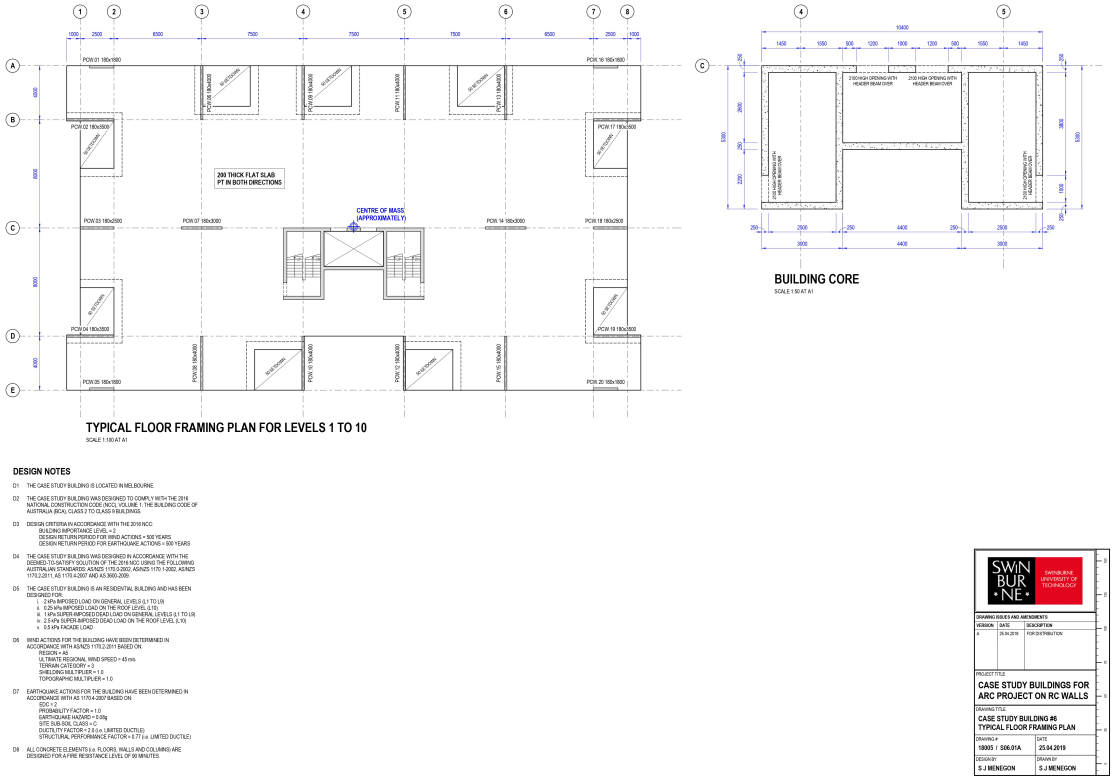

Figure C.5: Plan 3-front.

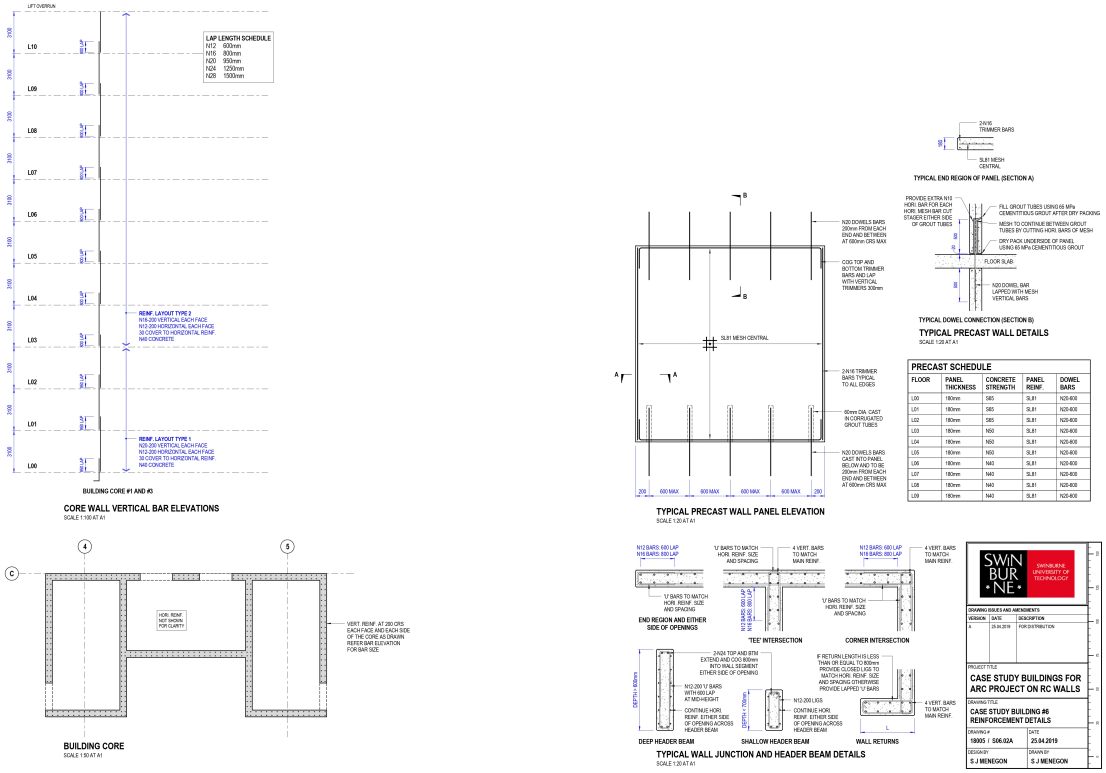

Figure C.6: Plan 3-back.

Appendix D

MATLAB Tool for implementing the Method in general building applications

As the final step in this thesis, a tool on the software MATLAB was created to make the method of optimal placement more accessible and easy to apply, without requiring users to understand all the codes used in this thesis or to be experts in MATLAB.

To achieve this, the App feature from MATLAB was utilized. This feature allows the creation of simple applications with an interface where the user inputs some parameters, and the software automatically returns the results. It was deemed to effectively meet the needs presented in this Appendix of creating an easy-to-use tool.

It is important to note that several assumptions were made during the development of this tool. The automation process necessitated some simplifications. However, a potential future direction for this thesis could involve revisiting these assumptions and expanding the tool to include scenarios where the initial assumptions may not hold.

The following sections detail the required inputs for the tool, the assumptions made during its development, and a step-by-step explanation of the process.

D.1 Inputs

In designing this simple tool, efforts were made to minimize the number of inputs required, asking the user to specify only the most critical parameters.

The required inputs, concentrated in the first tab of the tool, primarily relate to structural parameters (to define the mass matrix) and recorded accelerations (to compute the modal shapes). Specifically, the user is asked to provide:

1. Whether the goal is to find the optimal sensor placement for measuring only the flexural behavior in one direction or if the out-of-plane behavior is also of interest.

2. The mass of each floor or, if unknown, the type of frame of the structure.

3. The rotational inertia around the center of mass (this parameter is not needed if only flexural modes in one direction are considered).

4. The number of floors in the building.

5. The list of instrumented floors (with one or three sensors depending on the choice in point 1).

6. The path to the folder containing the recorded accelerations. The files in this folder should be ordered from the base upwards. If 3D behavior is to be investigated, the three acceleration files for each floor should be ordered with the two in the NS direction first and the one in the EW direction afterward.

7. The file extension of the acceleration files.

8. The time step used in the recorded accelerations.

Additionally, in the second tab of the tool, the user is asked to enter intervals where the natural frequencies should be computed for the different modes. The number of accelerometers to be placed on the structure, excluding the one at the base, should also be specified in this tab.

D.2 Hypotheses

Several key assumptions were made during the tool's development:

1. The pair of sensors on the same floor used to capture torsional motion are placed in the North-South direction.

2. If only flexural modes in one direction are of interest (2D method), the provided accelerations are assumed to be along the North-South direction.

3. The interstory height is considered uniform across all floors; thus, the building height is not directly relevant as all calculations reference the floors.

4. The mass is assumed to be homogeneously distributed along the height of the structure.

5. The tool only considers the first three modes in the three directions (NS, EW, and Torsion), as discussed in Chapter 5.

D.3 Guide to the Use

The tool is organized into three main tabs. The first tab requires all the inputs presented in Section D.1 from the user (Figure D.1, on the left); the second tab prompts the user to define intervals for detecting natural frequencies based on the plotted Fourier Transform Amplitude (Figure D.1, on the right); and the third tab visualizes the γ functions, identifies points of local minima, and proposes an optimal sensor layout based on the specified number of sensors (Figure D.2). To navigate

from the first tab to the second, and from the second to the third, the user must press the button at the bottom of the interface, which initiates a series of calculations until the next set of inputs is required. In particular, the user is asked to press "Compute the FFT" when passing from the first to the second tab and "Compute modal shapes and optimal placement" when passing from the second to the third tab.

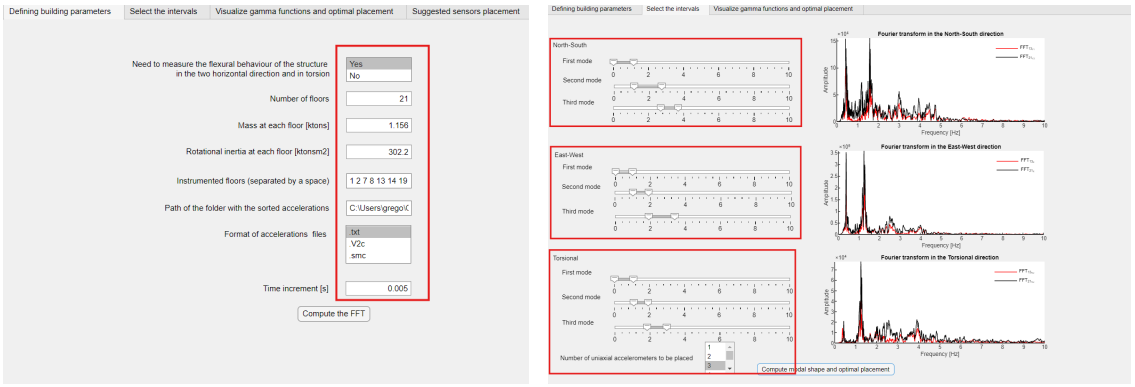

Figure D.1: First and second tabs, with inputs required from the user highlighted in red.

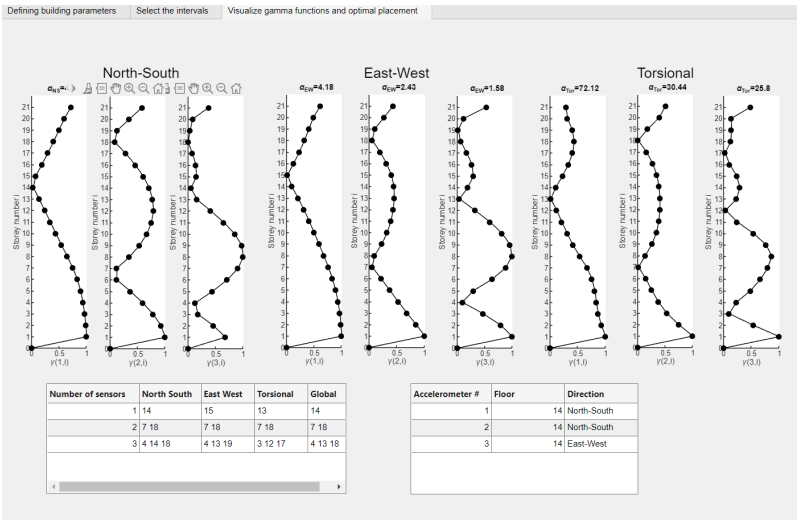

Figure D.2: Third tab, where the γ functions are visualized for the three directions and a proposed sensors' layout is provided corresponding to the previously selected number of accelerometers (in the table in the bottom right corner).

In the third tab, shown in Figure D.2, the table on the bottom left corner simply presents in a more coincise way the results from the diagrams of the γ function above. In addition, it averages the obtained values along the three directions presenting under a column, titled "Global", the result of this averaging.
The other table in the tab presents, based on the number of available sensors specified at the bottom of the second tab, a possible layout to capture the highest number of modes in one or three directions, depending if in the first tab it was selected to consider the 3D behaviour or not.

UNIVERSITÉ CATHOLIQUE DE LOUVAIN
École polytechnique de Louvain
Rue Archimède, 1 bte L6.11.01, 1348 Louvain-la-Neuve, Belgique | **www.uclouvain.be/epl**